

POLITECNICO DI TORINO

Collegio di Ingegneria

**Corso di Laurea Magistrale  
in Ingegneria Elettrica**

---

Tesi di Laurea Magistrale

**Distributed Model Predictive Control for  
Power Management in Small-scale Off-grid  
Energy Systems**



**Relatore**

prof. Gianmario Pellegrino

**Candidato**

Giuseppe Carnevale

**Correlatrice**

Anna Seppälä

---

Anno Accademico 2018/2019

*“Quant’è bella giovinezza,  
che si fugge tuttavia!  
chi vuol esser lieto, sia:  
di doman non c’è certezza.*

*[...]*

*Ciascun apra ben gli orecchi,  
di doman nessun si paschi;  
oggi siam, giovani e vecchi,  
lieti ognun, femmine e maschi;  
ogni tristo pensier caschi:  
facciam festa tuttavia.  
Chi vuol esser lieto, sia:  
di doman non c’è certezza.”*

“Trionfo di Bacco e Arianna”, Lorenzo de’ Medici.

---

# Abstract

In remote locations where there is no electricity grid the need for energy can be met by installing independently small electricity systems, called Off-grid systems. These systems utilize locally available renewable resources to provide electricity and are considered as an ecological and economical viable alternative to commonly used diesel generators. However, these small-scale renewable energy systems require a well-designed power management to ensure the power quality supply and to improve reliability while maintaining reduced costs. Power electronics technology with efficient control strategies are used to reach these targets, and nowadays new control methods to achieve better performance are receiving more attention.

The objective of the thesis is to model and simulate an off-grid PV system for power management, using an advanced control technique named Model Predictive Control (MPC), with the aim to write a stable and robust algorithm easy to implement on cheap microcontrollers. Mathematical analysis was performed to get the dynamic model of the components and control units. Performance of the simulations were evaluated in MATLAB programming interface to validate the effectiveness of the proposed model.

In the first chapter, a general introduction to the topic of the thesis is exposed, highlighting the motivation of the study, the objective and the approach used.

In the second chapter, the configuration of the off-grid PV system under study is presented. The proposed system is composed of a PV array, a non-inverting Buck-Boost DC-DC converter, a DC load connected to the DC bus, a Battery pack and a Bidirectional DC-DC converter. In this section all the components of the system are analyzed and modeled separately. Simulations results which proved the effectiveness of the models are reported and commented. For the PV array the common single diode model is proposed, and the non-linear characteristic of the model is tested for different irradiation and temperature conditions. For the non-inverting Buck-Boost converter the state-space averaging method is used to study its dynamic properties. A look to the issues regarding PV interfacing converters and the need to be implemented as current-fed converters is also presented. For the Battery a model that extract parameters directly from manufacture's datasheet was used. Finally, a detailed analysis of the Bidirectional converter model using state-space equations along with a simple analysis of the DC load are reported.

In the third chapter the design of the two proposed control units of the system are presented. The first control unit, which makes use of the maximum power point tracking (MPPT) algorithm to extract the maximum power from the PV panel, is introduced. The performance of the MPPT converter, are analyzed in terms of frequency responses. A classic control loop with a PI controller is designed, using the small-signal and the Bode plot analysis, to solve converter's stability problems. Worth to mention is that, this section also inspects the consequences on the stability by considering a current-fed convert, implemented with an additional input capacitor. The results of the voltage controlled MPPT converter are shown and discussed.

The second control unit is the MPC. The objective of the proposed method is to control the Bidirectional converter in order to balance the power between PV generation and load demand. Thus, initially the MPC principle of operation is explained and then a simple but effective control strategy is proposed. The advantage of the presented strategy is that the problem is formulated in a way that only one step prediction horizon is needed to control the converter. Therefore, the discrete model and a cost function, in terms of inductor current, are built. The MPC working principle

---

applied to the Bidirectional converter under study is illustrated and the results that validate the performance of the method are shown. Finally, a power management algorithm which coordinates the elements of the system is built, and to verify the performance, simulations for various scenarios are carried out.

In the chapter four, the direct voltage MPC strategy is presented. In this section, a different approach that considers a direct voltage control and a prediction horizon with  $N$  steps ( $N > 1$ ), is analyzed. First, a detailed explanation of the mathematical formulation of the proposed method is introduced. Then the discrete model of the Bidirectional converter which makes use of the small-signal state space equations is build, and a const function defined as a convex optimization problem is formulated. The optimal control actions that minimize the const function, obtained in MATLAB MPC Designer Toolbox environment, are reported. Lastly a sensitivity analysis to better understand the limitations of the approach together with the ultimately results are presented.

Finally, the work is summarized in the conclusions and the opportunities for a future work are considered.

---

# Acknowledgements

First of all, I would like to thank the Technical University of Munich that hosted me, and in particular Anna Seppälä that brought me step-by-step to the fulfillment of the thesis. Then I would like to thank my supervisor prof. Gianmario Pellegrino and the Politecnico di Torino that allowed me to write the thesis abroad, and I would also thank them for the constant dedication they put to satisfy the students' needs.

Finally, I would like and I am obligate to thank my big family, my girlfriend Alice and my friends that supported and motivated me throughout the difficulties encountered in the way.

Thank you! Grazie! Danke!

---

# Contents

- Abstract** ..... **i**
- Acknowledgements** ..... **iii**
- Contents** ..... **iv**
- Chapter 1. Introduction** ..... **1**
  - 1.1 Rural Areas and Off-grid Systems ..... 1
  - 1.2 Power Management and MPC Control ..... 2
  - 1.3 Thesis Objective and Approach ..... 3
- Chapter 2. Model of the Off-grid System** ..... **4**
  - 2.1 PV Model ..... 5
    - 2.1.1 Determination of Model Parameters ..... 7
    - 2.1.2 Validation of the Model ..... 8
  - 2.2 PV interfacing converters ..... 11
    - 2.2.1 Converter Topologies ..... 11
    - 2.2.2 Non-Inverting Buck-Boost Converter ..... 13
    - 2.2.3 Current Fed Converter ..... 14
    - 2.2.4 State Space Averaged Model ..... 16
    - 2.2.5 Converter Design ..... 25
    - 2.2.6 Validation of the Dynamic Model with Trapezoidal Method ..... 28
  - 2.3 Battery Energy Storage (BES) ..... 31
    - 2.3.1 Battery Model ..... 31
    - 2.3.2 Battery Model Validation ..... 33
    - 2.3.3 Battery Sizing ..... 35
  - 2.4 Bidirectional Buck-Boost Converter ..... 37
    - 2.4.1 Converter Modeling ..... 38
    - 2.4.2 Complementary Analysis ..... 41
    - 2.4.3 Converter Design ..... 42
  - 2.5 DC Load Analysis ..... 43
- Chapter 3. Control System Design** ..... **45**
  - 3.1 Maximum Power Point Tracking ..... 46
    - 3.1.1 P&O Algorithm ..... 46
  - 3.2 MPPT Converter Control ..... 48
    - 3.2.1 Open Loop Analysis ..... 49
    - 3.2.2 PI Controller Design ..... 50

---

3.2.3 Closed Loop Analysis .....	52
3.2.4. Implementation and Simulation Results .....	53
3.2.5. Improvements .....	56
3.3 Model Predictive Control .....	58
3.3.1 MPC Principle of Operation.....	58
3.3.2 Proposed Single-step Control Strategy .....	60
3.3.3 Implementation and Simulation.....	62
3.4 Power Management Strategy .....	64
<b>Chapter 4. Direct Voltage MPC.....</b>	<b>67</b>
4.1 Cost Function Formulation .....	67
4.2 Problem Statement and Small-signal Model.....	69
4.3 Implementation and Simulation Results .....	72
4.4 Sensitivity Analysis .....	75
<b>Conclusions.....</b>	<b>78</b>
<b>References .....</b>	<b>79</b>
<b>Appendix A – MATLAB Scripts of Chapter 2 .....</b>	<b>84</b>
<b>Appendix B – MATLAB Scripts of Chapter 3 .....</b>	<b>89</b>
<b>Appendix C – MATLAB Scripts of Chapter 4 .....</b>	<b>96</b>

---

# Chapter 1. Introduction

In this first chapter, a general introduction to the topic of the thesis is exposed, highlighting the motivation of the study, the objective and the approach used.

## *1.1 Rural Areas and Off-grid Systems*

In developed countries like UE, the access to electricity is widely accepted as a settled right for people. During the process of economic growth of these industrialized countries, energy and in particular electricity supply had a significant role in promoting improvements in the progress. Thus, it can be recognized that the availability of electricity has led to an enhanced well-being in these society.

However, in the world there are almost 1.2 billion of people that don't have access to electricity, and most of them live in poor isolated regions of developing countries, called rural areas. These areas are in general characterized by poor infrastructure, low services, high illiteracy, difficult access to clean water and health care, which turns in general in a low quality of life.

The activities that represent the principal source of income for the inhabitants are the pastoralism, the agriculture, fishing and sometimes also tourism. Thus, the demand for energy for rural families is mainly needed to cover basic needs as, cooking, space-heating and lighting [1].

In this contest the need for energy can be met by installing independently small electricity systems, called Off-grid systems. These systems utilize locally available renewable resources to provide electricity and are considered as an ecological and economical viable alternative to commonly used diesel generators. Off-grid systems are generally divided in two categories: mini-grids and stand-alone systems. The common feature is that, both operate independently and out of the electricity grid.

A mini-grid, also called micro-grid, is an off-grid system involving small-scale electricity generation and is generally defined as a distribution network having a power rating less than 11kW and operating out of the national utility grid [2]. Mini-grid supplies the electricity demand of small concentrated number of consumers, for domestic, business and social services. In general, mini-grids use renewable energies like wind, solar, hydro and biomass to generate the electricity, but they can also include back-up power supplies from diesel generators or battery packs.

Stand-alone systems present similar characteristics of mini-grids, but they are generally used to provide electricity to individual appliances such as house or small-businesses appliances. They use local renewable sources in combination with batteries to supply the customers' needs that in general are represented by DC devices.

Thanks to the drop in the installation price for both, mini-grid and stand-alone, off-grid systems are becoming more and more popular in the contest of energy security supply.

So far, much effort has been put in issues regarding energy security and energy resources, with the final target to assure universal access to energy, especially for remote locations. Small-scale off-grid generation systems represent an appropriate option to face energy needs and serve as a first step in the electrification process of a future electricity grid.

Since the 1980s, many programs have been promoting a grid development in rural areas. Generally, they were international aid projects or government projects mostly focused in initiative to improve health centers and social services [3]. Today, thanks to the drop-in prices, especially for photovoltaic systems, new funded programs have taken place in developing countries, and this has allowed rural families to afford the installation of small-scale off-grid systems.

---

Thus, the accessibility to electrical energy for dwellers of rural areas has become more common, and this has led to a better standard of living for inhabitant of these emarginated remote locations.

## *1.2 Power Management and MPC Control*

Off-grid systems have a great potential to bring energy where there is no electricity grid. However, these small-scale renewable energy systems require a well-designed power management to ensure the power quality supply and to improve reliability while maintaining reduced costs.

The renewable energy sources, that generally represents the main sources of the off-grid system are considered reliable, environmentally friendly and cost-effective. However, as known, they have an intermittent nature characteristic and so the major drawback of these sources is the uncertainty in the output power. Supplying energy to the customers with a high-power quality, avoiding voltage and power fluctuations to the load, is a great challenge that needs to be addressed [4].

Hence power management has become a critical aspect of enabling off-grid operation. When considering energy management different approaches can be taken into account, but the main objectives that a common power management system must consider are, to balance the different sources, to optimize energy utilization, to ensure power supply also during critical loads, to minimize operation costs and to consider environmental effects [5].

Generally, in off-grid systems storage units are implemented as a back-up energy source, to balance the power between generation and demand, moreover these devices improve efficiency and increase reliability of the system. The common storage units for small-scale off-grid system are batteries, and they represent the main vulnerable elements both in terms of costs and control. Thus, if efficiently controlled, energy storages can provide uninterrupted power to the load, so improving the whole system operation.

To overcome stability problems, and to further bring benefits to the system, other devises are integrated in the off-grid system. Power converters devices are used to interfaces power sources to the load and are essential elements to efficiently control the system. In off-grid systems they are mainly used to extract the maximum power for the variable sources, to manage the energy storage and in general to improve stability

Therefore, a power management strategy and a control unit that coordinates the elements of the system must be designed to make the power flow more efficient and reliable. In this thesis a new control method to achieve better performance is considered, named Model Predictive Control (MPC).

MPC is an advanced control technique that recently has become very popular in the field of power electronics. Although this strategy has been in use in process industry since the '80s, this powerful method was not possible to be applied for high switching frequencies devices because of the large calculation time needed for the control algorithm. In recent years, with the development of powerful microcontrollers, this issue is no more a problem and thus interest in the MPC has increased greatly [6]. The main idea of the MPC, is that a model of the system is used to predict the future behavior of the controlled variables, so that the optimal control action can be determined by minimizing a predefined cost function.

The operation principle and the implementation of the proposed MPC into the off-grid PV system, is presented in chapter 2.

---

### *1.3 Thesis Objective and Approach*

The objective of the thesis is to model and simulate an off-grid PV system for power management, using an advanced control technique named Model Predictive Control (MPC), to optimize the use of renewable sources and with the aim to write a stable and robust algorithm easy to implement on cheap microcontrollers.

Mathematical analysis is performed to get the dynamic model of the components and control units. Performance of the simulations are evaluated in MATLAB programming interface to validate the effectiveness of the proposed model.

In the second chapter, detailed modeling for each individual components of the off-grid PV system are presented. The validation of the implemented mathematical model for the PV panel and for the Battery is performed by comparing the simulation results with the manufacture's curves.

In the third chapter, the proposed control strategies are presented. The first approach to the MPC, considering a single step in the prediction horizon for current control, is explained. Simulation results, together with the power management algorithms are reported.

In the chapter four, a different approach for the MPC is proposed. The method considers a direct voltage control with a receding horizon. A detailed explanation of the mathematical formulation of the propose method, together with simulation results and a sensitivity analysis is reported in this chapter.

Finally, in the last chapter, the conclusions are summarized and commented, and an insight into a possible future work is also reported.

## Chapter 2. Model of the Off-grid System

In this chapter, the design of an off-grid PV system in terms of modeling the elements of the plant is discussed. The system under study is a common standalone PV system, where the load is supplied by the PV panel and a storage unit, usually a battery bank, is served as a backup source. All the components of the off-grid PV system have been modeled and simulated on MATLAB programming interface, and the simulation results validate the analyzed mathematical models. The configuration of the off-grid PV system analyzed is represented in Fig. 2.

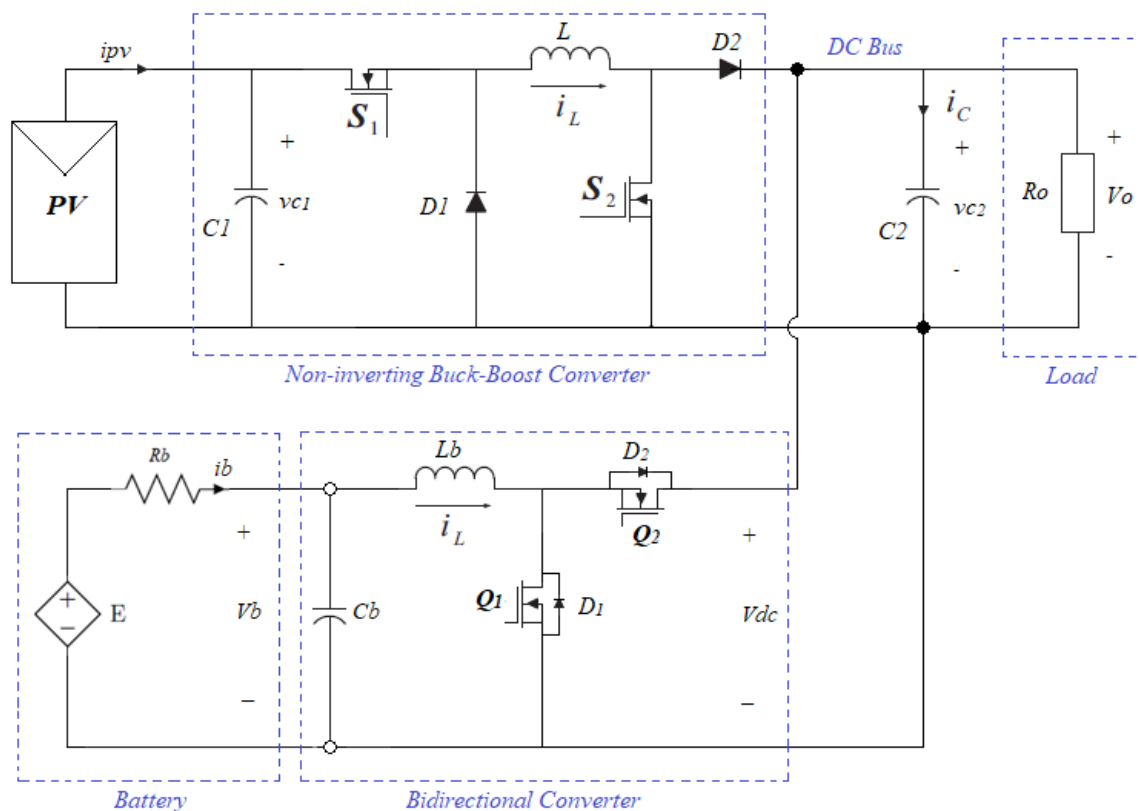


Fig. 2. Electrical scheme of the off-grid PV system.

The proposed system is composed of: a PV array, which represent the main power source; a non-inverting Buck-Boost DC-DC converter which interfaces the PV module with the DC bus connected to the load and is used to extract the maximum available power from the PV array, increasing or reducing the output voltage of the panel according to environmental conditions; a Battery Pack mainly used as a backup power source; and a Bidirectional DC-DC converter that connects the battery to the common DC bus, and is used to charge and discharge the battery to balance the power between PV generation and load demand, and moreover to maintain the DC bus voltage constant. If the generation exceeds the demand, the PV panel will charge the battery to store the extra power, otherwise, when the generation is less than the demand, the battery will discharge the stored power to supply the load [7]. Thus, the reliability of the whole generation system is improved.

## 2.1 PV Model

Solar energy is one of the most popular renewable energy sources. Photovoltaics is a branch of solar energy technology in which the light is converted directly into electricity [8].

Photovoltaic (PV) systems are made of PV cells which are basically two layers of semiconductor material with opposite charges. When sunlight enters the cell, its energy generates charge carriers, that originate an electric current, whom flows through the cell to produce power [9].

Various models of a PV cell have been proposed in the relevant literature. The most commonly used is the single diode model as it offers a good compromise between complexity and accuracy [10]. Its equivalent circuit is shown in Fig. 2.1.

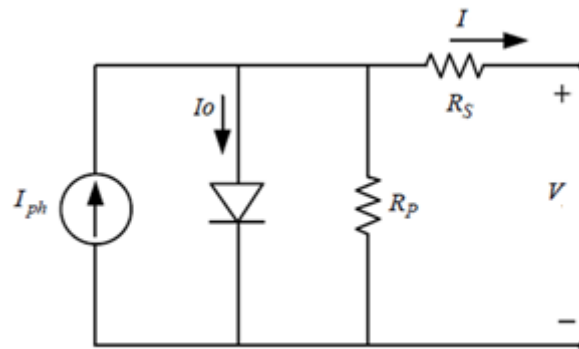


Fig. 2.1. Circuit diagram of the single diode PV model.

This PV cell model is a non-linear model and can be represented as a current source in parallel with diode as shown in the circuit, including the connection of series and parallel internal resistance, namely  $R_s$  and  $R_p$  respectively [11].

The  $I$ - $V$  characteristic of a PV cell is similar to diode characteristic, as illustrated in Fig. 2.2 [12].

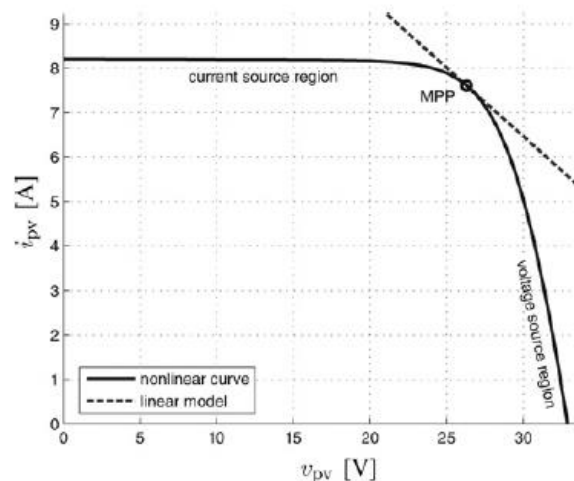


Fig. 2.2. Non-linear  $I$ - $V$  characteristic of a solar array and equivalent linear model at the MPP.

We can notice that the  $I$ - $V$  characteristic present a current source region and a voltage source region depending on the operating point. In addition, the figure shows that the PV array has a maximum power point (MPP). Ideally the array should operate at this point in order to deliver the maximum available instantaneous power.

In this thesis the PV array has been considered as a constant current source (CC), because the operation in the CC region of the  $I$ - $V$  curve presents the wider and most critical dynamic behavior, therefore modeling the solar cell in the current source region is more realistic and it will automatically fit for the operation in the voltage source region [13].

The PV characteristic depends on the solar irradiance and the temperature of the PV module. The effects of solar irradiance and temperature on the  $I$ - $V$  and  $P$ - $V$  characteristics of PV panel are illustrated in Fig. 2.3 [14].

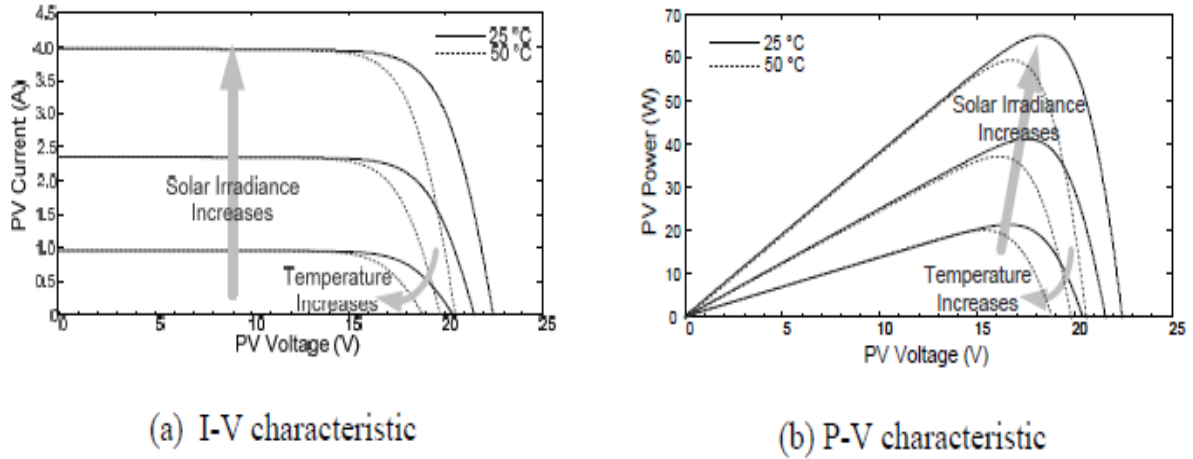


Fig. 2.3. The effect of solar irradiance and temperature on  $I$ - $V$  and  $P$ - $V$  characteristics.

It can be observed that as the solar irradiance increases, the photocurrent increases while the open circuit voltages are almost the same, hence, the power produced by the PV module increases. The open circuit voltage of the PV module decreases with a rise of the PV module temperature while the short circuit currents are almost the same.

It can also be seen that each curve has a unique MPP. The aim is to operate the PV system always at this maximum point to extract maximum power from the module.

The output current of the equivalent circuit,  $I$ , can be expressed as a function of the cell voltage,  $V$  [15]:

$$I = I_{ph} - I_o \left[ \exp \left( \frac{V + R_s I}{V_t a} \right) - 1 \right] - \frac{V + R_s I}{R_p} \quad (2.1)$$

where  $I_{ph}$  is the photocurrent,  $I_o$  is the diode saturation current,  $V_t = N_s \cdot k \cdot T / q$  is the thermal voltage of the array with  $N_s$  cells connected in series. Cells connected in parallel increase the current and cells connected in series provide greater output voltages. If the array is composed of  $N_p$  parallel connections of cells the photocurrent and saturation current may be expressed as  $I_{ph} = I_{ph} \cdot N_p$ ,  $I_o = I_o \cdot N_p$ . Moreover,  $q$  is the electron charge ( $1.60217646 \cdot 10^{-19}$  C),  $k$  is the Boltzmann constant ( $1.3806503 \cdot 10^{-23}$  J/K),  $T$  (in Kelvin) is the cell temperature and  $a$  is the ideality factor of the diode.

The parameters of the model are obtained from manufacturer's datasheets, which generally provide the open circuit voltage of the array ( $V_{oc,n}$ ), the short-circuit current ( $I_{sc,n}$ ), the maximum power voltage ( $V_{mp}$ ), the maximum power current ( $I_{mp}$ ), temperature coefficient of the open-circuit voltage ( $K_v$ ), temperature coefficient of the short-circuit current ( $K_i$ ), and the maximum experimental peak output power ( $P_{mp,e}$ ). This information is always provided with reference to the nominal condition or standard test conditions (STC) of temperature and solar irradiation ( $T_n = 25^\circ$  and  $G_n = 1000 \text{ Wb/m}^2$ ) [16].

Photocurrent  $I_{ph}$  mainly depends on the solar irradiation ( $G$ ) and on the temperature of the panel ( $T$ ) [17],

$$I_{ph} = \frac{G}{G_n} [I_{ph,n} + K_i (T - T_n)] \quad (2.2)$$

where,  $I_{ph,n}$  is the photocurrent at nominal condition, calculated based on (2.3)

$$I_{ph,n} = \frac{R_s + R_p}{R_p} I_{sc,n} \quad (2.3)$$

The diode saturation current,  $I_o$  varies with the cell temperature and can be expressed by [16]

$$I_o = I_{o,n} \cdot \left(\frac{T}{T_n}\right)^3 \cdot \exp\left[\frac{q E_g}{a k} \left(\frac{1}{T_n} - \frac{1}{T}\right)\right] \quad (2.4)$$

where  $E_g$  (eV) is the band-gap energy of the cell material ( $E_g = 1.12$  eV for polycrystalline Si at 25 °C [18]). The diode saturation current at the STC is related to the photocurrent at STC,

$$I_{o,n} = \frac{I_{sc,n}}{\left[\exp\left(\frac{V_{oc,n}}{V_t a}\right) - 1\right]} \quad (2.5)$$

Those equations mainly represent the single diode PV model.

### 2.1.1 Determination of Model Parameters

Manufacturers of PV arrays provide only a few experimental data about electrical and thermal characteristics. Therefore, some of the parameters required for adjusting PV array models cannot be found in the datasheets and they need to be determined, such as the diode ideality factor, the series and shunt resistances and the diode saturation current [16].

The ideality factor  $a$  is a constant which depends on PV cell technology and can be chosen according to Table 1 [19].

**Table 1.** Ideality factor  $a$ .

Technology	Ideality factor $a$
Si-mono	1.2
Si-poly	1.3
a-Si-H	1.8
a-Si-H tandem	3.3
a-Si-H triple	5
CTs	1.5
AsGa	1.3

The series resistance of the panel corresponds to the internal losses due to current flow and has a large impact on the slope of the  $I$ - $V$  curve at  $V = V_{oc}$ , while the shunt resistance accounts for the losses due to the leakage currents across the cell and impacts the slope of the  $I$ - $V$  curve at  $I = I_{sc}$  [20].

The relation between those unknown parameters,  $R_s$  and  $R_p$ , may be found by making the maximum power calculated by the  $I$ - $V$  model ( $P_{mp,m}$ ) equal to the maximum experimental power from the datasheet ( $P_{mp,e}$ ) at the MPP ( $P_{mp,m} = P_{mp,e}$ ) and solving the resulting equation for  $R_s$ , as shown in [16].

$$P_{mp,m} = V_{mp}I_{mp} = V_{mp} \left\{ I_{ph} - I_o \left[ \exp \left( \frac{V_{mp} + R_s I_{mp}}{V_t a} \right) - 1 \right] - \frac{V_{mp} + R_s I_{mp}}{R_p} \right\} \quad (2.6)$$

$$= P_{mp,e}$$

$$R_p = V_{mp}(V_{mp} + R_s I_{mp}) / \left\{ V_{mp} I_{ph} - V_{mp} I_o \exp \left( \frac{V_{mp} + R_s I_{mp}}{V_t a} \right) + V_{mp} I_o - P_{mp,e} \right\} \quad (2.7)$$

The method proposed is based on the fact that for any value of  $R_s$  there will be a value of  $R_p$  that makes the mathematical  $I$ - $V$  curve cross the experimental ( $V_{mp}$ ,  $I_{mp}$ ) point. The goal is to find the value of  $R_s$  (and hence,  $R_p$ ) that makes the peak of the mathematical  $P$ - $V$  model ( $P_{mp,m}$ ) coincide with the experimental peak power, from the datasheet ( $P_{max,e}$ ), at the MPP ( $V_{mp}$ ,  $I_{mp}$ ). This requires several iterations until  $P_{max,m} = P_{max,e}$ . Each iteration updates  $R_s$  and  $R_p$  toward the best model solution. The iteration starts at  $R_s = 0$ , which must increase in order to move the modeled MPP until it matches with the experimental MPP. The corresponding initial value of  $R_p$  may be given by:

$$R_{p,min} = \frac{V_{mp}}{I_{sc,n} - I_{mp}} - \frac{V_{oc,n} - V_{mp}}{I_{mp}} \quad (2.8)$$

Equation 2.8 determines the minimum value of  $R_p$ , which is the slope of the line segment between the short circuit and the maximum power. Although  $R_p$  is still unknown, it surely is greater than  $R_{p,min}$  and this is a good initial guess [21].

The implementation presented is used to simulate the proposed model (Solarex SX80 [22]) by incrementing  $R_s$  until matching  $P_{mp,m}$  with  $P_{mp,e}$ . The iterative method gave  $R_s = 0.1930 \Omega$  and  $R_p = 201.2957 \Omega$ .

The MATLAB script file that shows the iterative method is reported in **Appendix A.1**.

Considering that the saturation current  $I_o$  is strongly dependent on the temperature, a further improvement in the model can be done by including in the equation (2.4) the current and voltage coefficients  $K_i$  and  $K_v$  [16].

$$I_o = \frac{I_{sc,n} + K_i (T - T_n)}{\exp \left( \frac{V_{oc,n} + K_v (T - T_n)}{V_t a} \right) - 1} \quad (2.9)$$

This equation simplifies the model and aims to match the open circuit voltage of the model with the experimental data for a very large range of temperatures. Another interesting fact is that introducing the coefficient  $K_v$  from the manufacturer's datasheet brings important information necessary to achieve the best possible  $I$ - $V$  curve.

### 2.1.2 Validation of the Model

For the simulation the Solarex SX80 array was chosen to illustrate and verify the model. The electrical parameters given by datasheet and those determined from the model are listed in Table 2.

**Table 2.** Parameters of Solarex SX80 array at STC.

Parameters	Values
$I_{mp}$	4.75 A
$V_{mp}$	16.8 V
$P_{mp,e}$	79.8 W
$I_{sc}$	5.17 A
$V_{oc}$	21 V
$N_s$	36
$a$	1.3
$R_s$	0.1930
$R_p$	201.2957

To see if the chosen model, characterized by previous equations, follows properly the real values of the PV array and to graphically compare the mismatch between the measured curves from the datasheet and the results of the considered model, the model of the PV array was implemented and simulated in MATLAB.

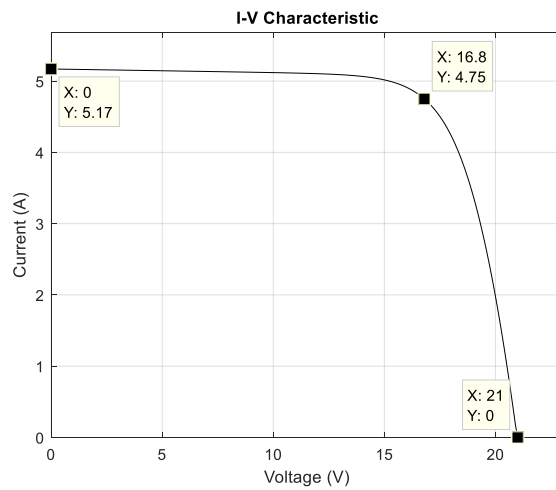


**Fig. 2.4.** I-V curve at remarkable points.

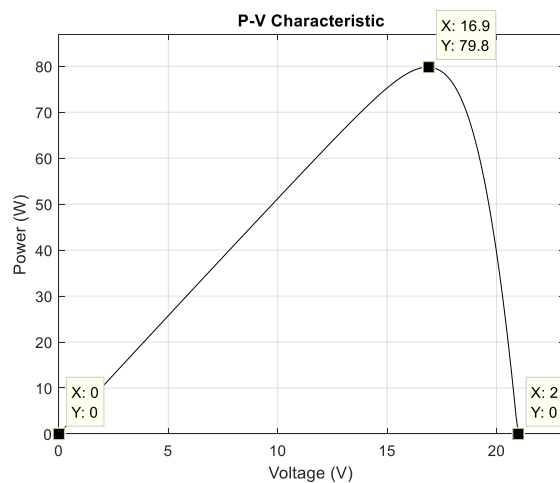


**Fig. 2.5.** P-V curve at remarkable points.

The I-V curve of a solar cell has three important points called remarkable points: short circuit ( $0, I_{sc}$ ), open circuit ( $V_{oc}, 0$ ) and MPP ( $V_{mp}, I_{mp}$ ).

According to Tables 2 and Figs. 2.5-2.6, the developed model and the experimental data are exactly matched at the nominal (STC) remarkable points of the  $I$ - $V$  and  $P$ - $I$  curves.

In general, practical operating conditions are mostly different from the desired standard conditions. Therefore, in order to test the validity of the model, a comparison with other experimental data is performed. The Simulation was carried out for different level of irradiances and for different temperature levels. The  $I$ - $V$  and  $P$ - $V$  curves plotted at different conditions are shown in Fig. 2.6 and Fig. 2.7, respectively.

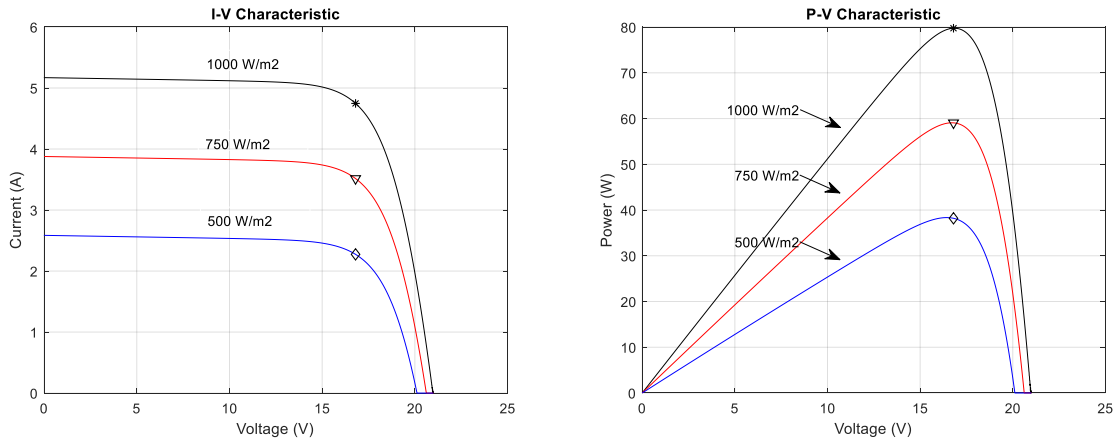


Fig. 2.6.  $I$ - $V$  and  $P$ - $V$  curves for different irradiances, 25 °C.

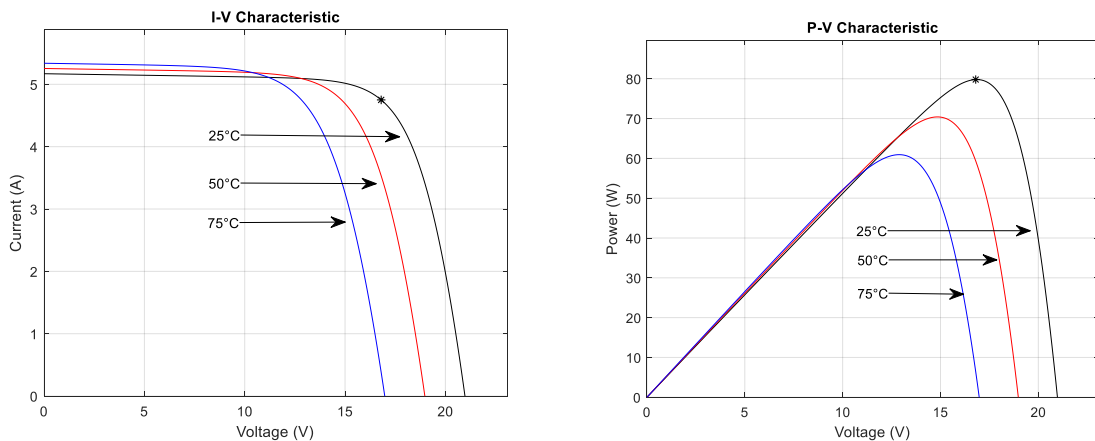


Fig. 2.7.  $I$ - $V$  and  $P$ - $V$  curves at different temperatures, 1000 W/m<sup>2</sup>.

The similarities of the  $I$ - $V$  curves for different conditions with the corresponding curves taken from the Solarex SX 80 panel datasheet, prove the validity of the developed solar panel model. Fig. 2.8 validate that the model accurately matches with the experimental data.

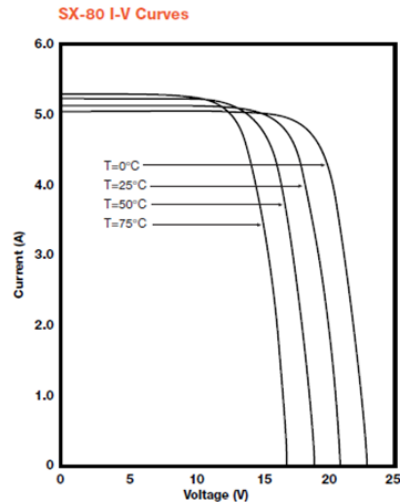


Fig. 2.8. Solarex SX 80 I-V curves at different temperatures,  $1000 \text{ W/m}^2$ .

The PV array model was implemented in MATLAB. The parameters required for simulation and the implementation of the equations are initialized by the script-code file attached in **Appendix A.2**.

The simplicity of the single diode model with the parameter improvements proposed, make this model perfect for power electronics designers who need an easy and effective model for the simulation of PV arrays with power converters [16].

## 2.2 PV interfacing converters

The solar generator output is seldom suited for directly feed small loads such as lighting systems and DC motors, because of its highly dependence on the environmental conditions, such as ambient temperature, solar irradiation, cloud passing, etc. This low conversion rate of PVs prohibits the system to operate with maximum efficiency, hence energy is wasted [23]. Therefore, to increase the conversion efficiency of a PV power system, a DC-DC converter with the maximum power point tracking (MPPT) is required, to ensure that the maximum available solar energy could be harvested from the solar panel.

Converters with the MPPT feature use an algorithm to continuously detect the maximum instantaneous power of the PV array. Many MPPT methods have been proposed in the literature. However, the achievement of MPPT strongly depends on the performance of the converter and its ability to regulate the operating point of the PV array [12].

### 2.2.1 Converter Topologies

There are three main DC-DC converter topologies used to achieve the MPP operation, the Buck converter, the Boost converter and Buck-Boost converter. A Buck converter is a step-down voltage converter since its output voltage is lower than its input voltage. For the Buck-type converter the input current is discontinuous and the output current flowing through the inductance is continuous [24]. A Boost converter is similar to the Buck converter except it functions as a step-up converter. Its output voltage is higher than the input voltage. For the Boost-type converter, the input current flowing into the inductance is continuous and the output current is discontinuous.

Non isolated Buck and Boost DC-DC converters are widely used in stand-alone photovoltaic power systems because of their simplicity and efficiency. For comparison [25], the Boost topology has some

---

advantages over the Buck for this application. To achieve the same ripple of inductor current, the Boost topology needs more inductance than the Buck converter. However, the rms current through the inductor is much lower than that of the Buck converter. If considering the input capacitors, the Buck topology requires a large capacitor to smooth the discontinuous input current from the PV module. On the other hand, the PV current in the Boost converter is as smooth as its inductor current, without any input capacitor.

The capacity of solar generation systems depends heavily on the presence of light. At night, a current could flow back into PV cells from the bus; however, reverse current must be avoided because it causes leakage loss or extensive damage [18]. Blocking diodes are effective to prevent reverse current flows. In the Boost topology, the freewheel diode can serve as the blocking diode to avoid this current. However, a Buck converter requires an additional diode to block reverse current flow. This results in an increase in cost and additional power loss due to the forward voltage drop.

Lastly, regarding the MPPT, the Boost converter is shown to have a slight advantage over the Buck, particularly at low light levels, since it can always track the MPP. The input voltage of a Buck converter is always greater than or equal to its output voltage. Hence, a Buck converter can operate at the MPP under most, but not all, conditions. Instead, the input voltage of a Boost converter must lie between zero and the output voltage, for complete control of the power flow. Thus, a Boost converter is always able to operate at the panel's MPP.

In the last topology, the output voltage of the Buck-Boost converter can be either higher or lower than the input voltage. Several commonly used Buck-Boost power converters have been proposed in the literature as PV interfacing converter [17]. Among the others: conventional Buck-Boost, Cuk and SEPIC, are the most known.

Cuk converter has the advantage that the input and output inductors create a smooth current at both sides of the converter while the conventional Buck-Boost has at least one side with pulsed current. However, both, Cuk and conventional Buck-Boost, are inverting type power converters (output voltage polarity is reversed). SEPIC converter has the advantage to have zero-ripple output current and non-reversed polarity, however it has less reliability and needs more components.

These problems are solved by using a non-inverting Buck-Boost converter which can work over a wide range of input voltage to generate both higher and lower voltages while supplying high current. Although two switches are required versus only one in the inverting or Cuk converters, only one capacitor and inductor are necessary, versus two for each in the Cuk converter [26].

The converter is constructed with two independently controllable switches such that it can be operated as a Buck or as a Boost converter in different portions of the input voltage. Such a topology could offer high efficiency, low stress on switches, low volume, and positive polarity of output voltage [27]. The equivalent circuit for the different topologies considered is shown in Fig. 2.9.

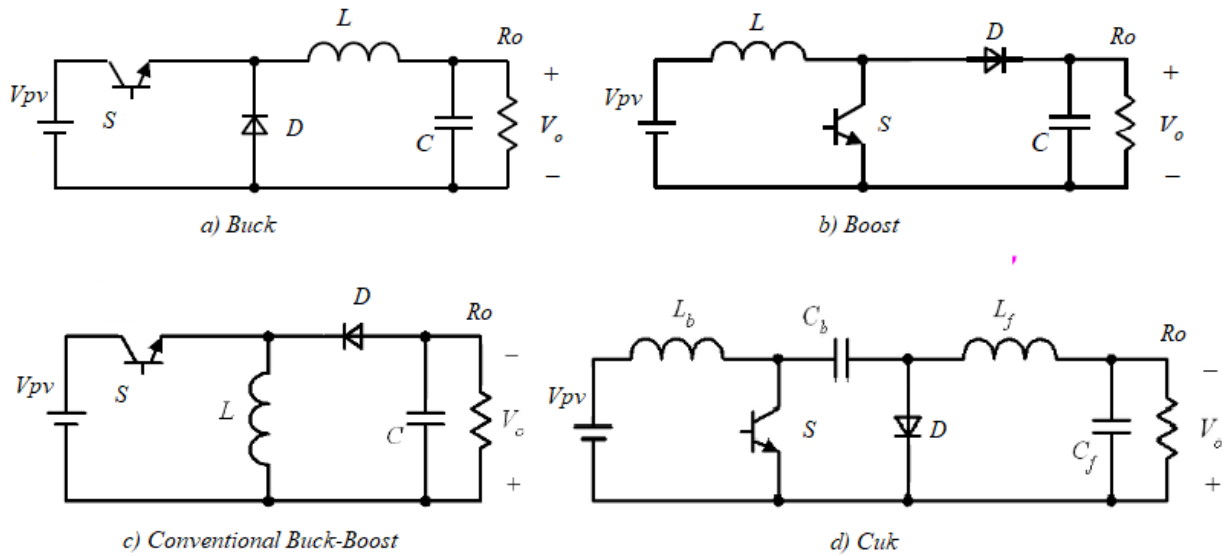


Fig. 2.9. Converter topologies: a) Buck; b) Boost; c) conventional Buck-Boost; d) Cuk.

### 2.2.2 Non-Inverting Buck-Boost Converter

A non-inverting Buck-Boost converter, as shown in Fig. 2.10, is basically a combination of a Buck converter and a Boost converter with two switches ( $S_1$  and  $S_2$ ), an inductor and a capacitor. The extra switch and a diode solve former converters problems. As the name implies, this converter does not invert the polarity of the output voltage in relation to the polarity of the input. In addition, the non-inverting Buck-Boost converter is capable of being used in three separate operating modes which are Buck mode, Boost mode and Buck-Boost mode [28].

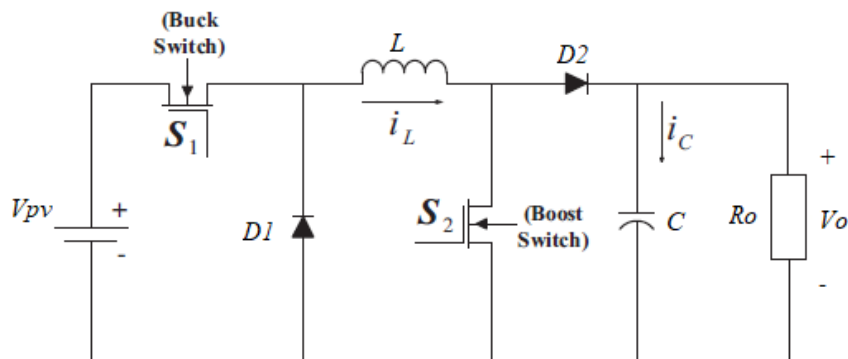


Fig. 2.10. Non-inverting Buck-Boost converter.

Depending upon the load condition the converter operates in one of these modes. In Buck-only mode,  $S_1$  is used as a switch, with the diode  $D_1$ .  $S_2$  is turned OFF and diode  $D_2$  is always ON. In the continuous conduction mode (CCM) condition, the voltage conversion ratio is  $V_o = D \cdot V_{pv}$ , where  $D$  is the duty cycle of  $S_1$ . Fig. 2.11 shows the converter operating in Buck mode [29].

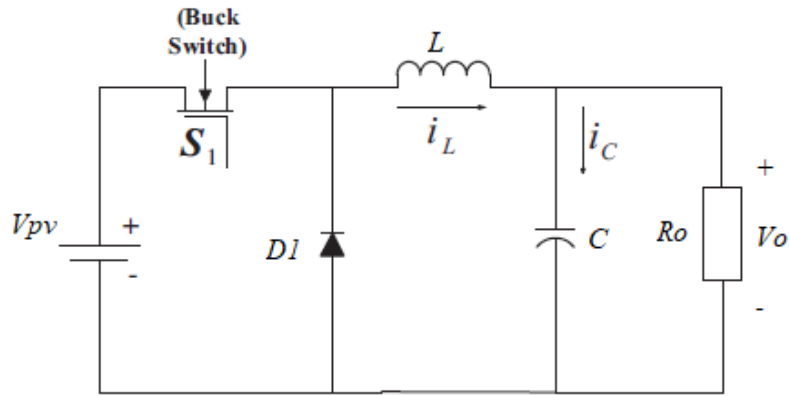


Fig. 2.11. Non-inverting Buck-Boost converter in Buck mode.

In Boost-only mode then, the switch  $S_1$  remains close.  $S_2$  is used as a switch and  $D_2$  acts as the diode in the Boost regulator.  $S_1$  is always ON and  $D_1$  is always OFF. In the CCM condition, the voltage conversion ratio is  $V_o = V_{pv}/(1-D)$ , whith  $D$  duty cycle of  $S_2$ . The circuit diagram of the converter operating in Boost mode in shown in Fig. 2.12.

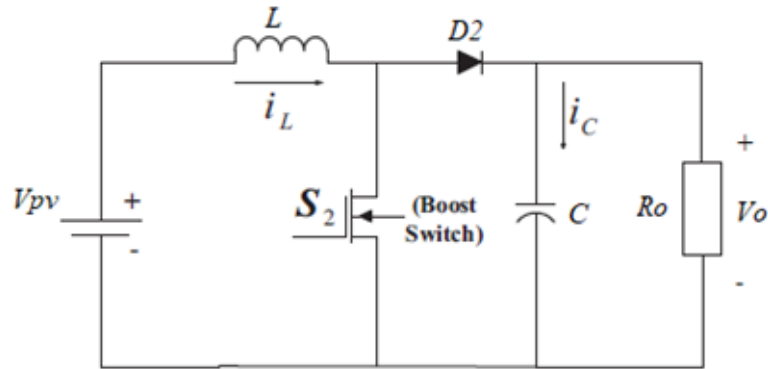


Fig. 2.12. Non-inverting Buck-Boost converter in Boost mode.

In Buck-Boost mode the  $S_1$  and  $S_2$  are simultaneously ON during the switching cycle or ON time, while  $D_1$  and  $D_2$  are simultaneously ON during the opposite switching cycle or OFF time. This means that when  $S_1$  and  $S_2$  are turned ON, the inductor is getting charged, so  $D_1$  and  $D_2$  are turned OFF. Vice versa when  $D_1$ ,  $D_2$  are ON, the inductor is charging the load capacitor, so  $S_1$  and  $S_2$  are turned OFF [29].

### 2.2.3 Current Fed Converter

As seen, an efficient PV power generation requires that a certain MPP of the PV generator is located. This is usually performed by an interfacing DC-DC power converter employing some MPP-tracking techniques and algorithms. Therefore, it is extremely important to have consistent information's regarding the nature of the energy source and interfacing devices as well as the load connected to the system.

The interfacing of a solar generator is rather complicated due to the terminal characteristics of the solar cell. Basically, the solar cell can be considered as a highly non-linear and non-ideal current source having both constant current (CC) and constant voltage (CV) like properties depending on the operating point. The CC and CV regions of the solar cell imply that the interfacing converter can be based either by using voltage-fed (VF) or current-fed (CF) converters [30]. Naming of the classes is

based on the type of the input energy source; the VF converter is fed by a voltage source and the CF converter by a current source. In general VF converters dominate in power supply applications, because most of the energy sources are voltage sources by nature. The static and dynamic properties of the VF converters are well known, however frequently they are applied without considering the real nature of the application environment and the theoretical basis of the controller.

Due to the current-source nature of the solar cell, proper CF interfacing cannot be done by conventional VF converters, because it neglects the current-source nature of a PV array and may give inconsistent information on the behavior of the converter in real application.

The CF converters in PV interfacing are already widely utilized and recognized, but usually they are implemented implicitly by modifying the conventional VF converter, therefore the dynamic properties of such converters are not fully understood and nor treated accordingly. The CF properties of the conventional VF converters can be created by applying the duality transformation which suggests that any electrical circuit can be transformed to its dual circuit. There are three different ways to derive CF converters [8].

Firstly, the converters can be implemented based on *intuition*. This method is analogous to the design of conventional VF converters, but it is performed under CF domain. Basically, the practical power stage is constructed based on the circuit theory to satisfy with a current type source.

Secondly, the CF converters can be implemented by an *explicit duality transformation* method from the corresponding VF converter, e.g. the VF Buck transforms into its dual CF Buck.

The third method is the *implicit* implementation. The CF properties of the conventional VF converters are obtained by adding a capacitor at the input of an existing VF power stage and modifying the feedback control scheme (the polarity of the feedback and reference signal must be changed for proper operation). Adding a capacitor, to enhance the constant-voltage properties of the source, is understandable because it is common to consider voltage source in series with inductor as a current source and the same idea can be applied to the parallel connection of current source and capacitor, yielding at voltage source as shown in Fig. 2.13 [8].

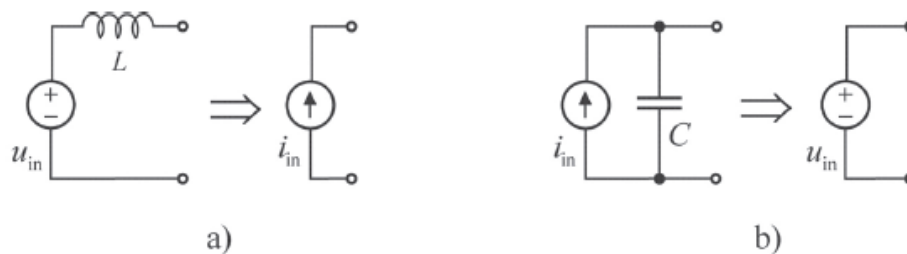


Fig. 2.13. a) a voltage source in series with an inductor becomes a current source and b) a current source in parallel with a capacitor becomes a voltage source.

The above method, however, may lead to misinterpretations in the analysis of the PV power system if the domain change from VF to CF is not recognized, because the adding of the capacitor does not practically remove the effects of the current source or the PV module and the controlling schemes of the converters are not always presented unambiguously (positive vs. negative feedback). The capacitor can be added to ease the PV interfacing, but it also changes the dynamic properties of the converter. Therefore, a proper dynamic model of a switched-mode converter must be developed.

## 2.2.4 State Space Averaged Model

It was shown that the input source has a significant effect on converter dynamics. Fig. 2.14 shows the non-inverting Buck-Boost converter with an additional input capacitor. The modification changes the VF converter into a CF converter with corresponding steady-state and dynamic properties.

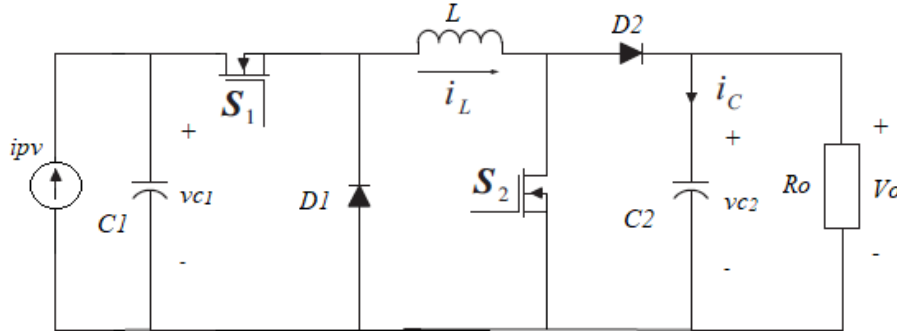


Fig. 2.14. Non-inverting Buck-Boost converter with additional input capacitor.

The dynamic of a switched-mode converter can be obtained analytically by applying the well-known state-space averaging method, performed by averaging its operation over one switching period and linearizing the averaged model at certain operation point [8]. Using the state-space averaging method the small-signal averaged equations, and therefore the transfer functions necessary for the control analysis, can be obtained.

The mathematical model is based on the state-space representation method [31].

$$\begin{cases} \dot{\mathbf{x}} = \mathbf{A}\mathbf{x} + \mathbf{B}\mathbf{u} \\ \mathbf{y} = \mathbf{C}\mathbf{x} + \mathbf{D}\mathbf{u} \end{cases} \quad (2.10)$$

Where  $\mathbf{x}$  is the state vector containing all the state variables,  $\dot{\mathbf{x}} = d\mathbf{x}/dt$ ,  $\mathbf{u}$  is the input or control vector,  $\mathbf{y}$  is the output variable vector and  $\mathbf{A}$ ,  $\mathbf{B}$ ,  $\mathbf{C}$ ,  $\mathbf{D}$  are coefficient matrices consisting of constant elements such as resistances, inductances and capacitances.

The physical state variables of a system are usually associated with the storage of energy, as the inductor currents and capacitor voltages. The state variables of the non-inverting Buck-Boost converter, shown in Fig. 2.14, are the inductor current  $i_L$ , the output voltage  $vc_2$  and the input voltage  $vc_1$ . The introduction of a new system variable, the input voltage capacitance, increases the dynamic modes of the system compared to the VF without the input capacitor, resulting in different steady state waveforms and more complex describing equations [32]. The output variable of the converter can be either the current or the voltage. The input voltage  $vc_1$  has been chosen as the controlled variable, in order to regulate the operating point of the array. It is observed [8], that in the MPP-tracking process of the PV generator the current control is prone to saturation. Therefore, the input voltage is recommended to be controlled in order to avoid saturation. Moreover, the voltage control is preferred because the voltage at the MPP is approximately constant [12]. The PV current, on the other hand, changes greatly when the solar irradiation varies.

A non-inverting Buck-Boost converter is a combination of Buck and Boost converters with different modes of operation [33]. In order to obtain the state-space model of the converter, each operating mode needs to be considered. Table 3 shows the different operational modes and the corresponding switching states [28]. In Buck operation, switch  $S_2$  is always off during the switching interval, while  $S_1$  is switched on and off. In Boost mode,  $S_1$  remains constantly on during the switching interval and  $S_2$  is switched. In addition, if both  $S_1$  and  $S_2$  are switched simultaneously with the same duty cycles, the

non-inverting Buck-Boost converter is similar to the conventional Buck-Boost converter in terms of performance. Since in this mode both switches are continuously turned on and off, the switching losses are higher than the other modes. Therefore, this operation mode is avoided. Avoiding from using this mode does not put any limitation on the converter functionality. In summary, the converter can only be utilized in either Buck or Boost modes [33].

**Table 3.** Switching modes of non-inverting Buck-Boost converter.

Mode	S1	S2
Buck	Switching	Off
Boost	On	Switching
Buck-Boost	Switching	Switching

For each operation mode two subintervals could be considered, which correspond to the two different possible switching states, defined as the switch-on state and switch-off state. Assuming that all the converter's components are ideal, and that the converter operates in a continuous conduction mode (CCM) [34].

In **Buck** mode, its equivalent circuit for each switching state is represented in Fig. 2.15.

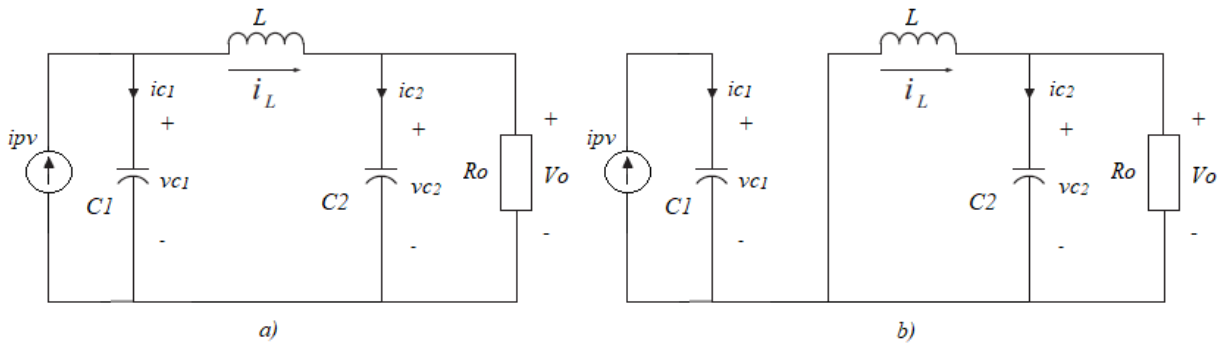


*Fig. 2.15. Non-inverting Buck-Boost converter in Buck mode: a) switch S1 is on; b) switch S1 is off.*

Based on the electrical circuit depicted in Fig. 2.15, differential equations of the state variables and output variable can be derived. During the switch-on interval, equations are:

$$L \frac{di_L}{dt} = vc_1 - vc_2 \quad (2.11)$$

$$C_1 \frac{dvc_1}{dt} = ipv - i_L \quad (2.12)$$

$$C_2 \frac{dvc_2}{dt} = i_L - \frac{vc_2}{R} \quad (2.13)$$

$$vpv = vc_1 \quad (2.14)$$

equations (2.11) – (2.14) can be expressed in state-space form, as:

$$\begin{cases} \dot{\mathbf{x}} = \mathbf{A}_{on}\mathbf{x} + \mathbf{B}_{on}\mathbf{u} \\ \mathbf{y} = \mathbf{C}_{on}\mathbf{x} + \mathbf{D}_{on}\mathbf{u} \end{cases}, \quad \mathbf{x} = \begin{bmatrix} i_L \\ vc_1 \\ vc_2 \end{bmatrix}, \quad \mathbf{u} = [ipv], \quad \mathbf{y} = [vpv] \quad (2.15)$$

$$\begin{bmatrix} \dot{i}_L \\ \dot{v}c_1 \\ \dot{v}c_2 \end{bmatrix} = \begin{bmatrix} 0 & \frac{1}{L} & -\frac{1}{L} \\ -\frac{1}{C_1} & 0 & 0 \\ \frac{1}{C_2} & 0 & -\frac{1}{RC_2} \end{bmatrix} \begin{bmatrix} i_L \\ v c_1 \\ v c_2 \end{bmatrix} + \begin{bmatrix} 0 \\ 1 \\ 0 \end{bmatrix} ipv \quad (2.16)$$

$$[vpv] = [0 \quad 1 \quad 0] \begin{bmatrix} i_L \\ v c_1 \\ v c_2 \end{bmatrix} \quad (2.17)$$

where  $\mathbf{D}_{on} = [0]$ .

During the second subinterval, when the switch is off, differential equations are:

$$L \frac{di_L}{dt} = -vc_2 \quad (2.18)$$

$$C_1 \frac{dvc_1}{dt} = ipv \quad (2.19)$$

$$C_2 \frac{dvc_2}{dt} = i_L - \frac{vc_2}{R} \quad (2.20)$$

$$vpv = vc_1 \quad (2.21)$$

that in state-space form become:

$$\begin{cases} \dot{\mathbf{x}} = \mathbf{A}_{off}\mathbf{x} + \mathbf{B}_{off}\mathbf{u} \\ \mathbf{y} = \mathbf{C}_{off}\mathbf{x} + \mathbf{D}_{off}\mathbf{u} \end{cases} \quad (2.22)$$

$$\begin{bmatrix} \dot{i}_L \\ \dot{v}c_1 \\ \dot{v}c_2 \end{bmatrix} = \begin{bmatrix} 0 & 0 & -\frac{1}{L} \\ 0 & 0 & 0 \\ \frac{1}{C_2} & 0 & -\frac{1}{RC_2} \end{bmatrix} \begin{bmatrix} i_L \\ v c_1 \\ v c_2 \end{bmatrix} + \begin{bmatrix} 0 \\ 1 \\ 0 \end{bmatrix} ipv \quad (2.23)$$

$$[vpv] = [0 \quad 1 \quad 0] \begin{bmatrix} i_L \\ v c_1 \\ v c_2 \end{bmatrix} \quad (2.24)$$

where  $\mathbf{D}_{off} = [0]$ .

Buck mode converter in state-space is described by equations (2.15) and (2.22), that correspond to the two possible switching states [35]. According to the state-space averaging method [36], by applying the weighted sum of the two mentioned equations the averaged state equation can be written.

$$\begin{cases} \dot{\bar{\mathbf{x}}} = \mathbf{A}\bar{\mathbf{x}} + \mathbf{B}\bar{\mathbf{u}} \\ \bar{\mathbf{y}} = \mathbf{C}\bar{\mathbf{x}} + \mathbf{D}\bar{\mathbf{u}} \end{cases} \quad (2.25)$$

Where now  $\bar{x}$ ,  $\bar{u}$  and  $\bar{y}$  are the averaged vectors containing all the averaged variables, and  $A$ ,  $B$ ,  $C$ ,  $D$  are the averaged matrices, calculated as:

$$\begin{aligned} A &= dA_{on} + (1-d)A_{off} \\ B &= dB_{on} + (1-d)B_{off} \\ C &= dC_{on} + (1-d)C_{off} \\ D &= dD_{on} + (1-d)D_{off} \end{aligned} \quad (2.26)$$

where  $d = ton/T$ , ( $T$ , switching interval) is the converter duty cycle representing the switching-on interval and  $(1-d) = toff/T$  is the complement of duty cycle representing the switching-off interval. Therefore, by combining the continuous equations corresponding to the two subintervals, the averaged matrices and the corresponding average state-space model of the converter in Buck mode is obtained.

$$A = \begin{bmatrix} 0 & \frac{d}{L} & -\frac{1}{L} \\ -\frac{d}{C_1} & 0 & 0 \\ \frac{1}{C_2} & 0 & -\frac{1}{RC_2} \end{bmatrix}, B = \begin{bmatrix} 0 \\ 1 \\ C_1 \\ 0 \end{bmatrix}, C = [0 \quad 1 \quad 0], D = [0] \quad (2.27)$$

$$\begin{bmatrix} \dot{i}_L \\ \dot{v}_{c1} \\ \dot{v}_{c2} \end{bmatrix} = \begin{bmatrix} 0 & \frac{d}{L} & -\frac{1}{L} \\ -\frac{d}{C_1} & 0 & 0 \\ \frac{1}{C_2} & 0 & -\frac{1}{RC_2} \end{bmatrix} \begin{bmatrix} \bar{i}_L \\ \bar{v}_{c1} \\ \bar{v}_{c2} \end{bmatrix} + \begin{bmatrix} 0 \\ 1 \\ C_1 \\ 0 \end{bmatrix} \bar{v} \quad (2.28)$$

$$[\bar{v}pv] = [0 \quad 1 \quad 0] \begin{bmatrix} \bar{i}_L \\ \bar{v}_{c1} \\ \bar{v}_{c2} \end{bmatrix} \quad (2.29)$$

The steady-state operation point can be obtained from (2.25) by setting  $\dot{x} = 0$  [37], yielding:

$$\begin{cases} \mathbf{0} = \mathbf{A}\mathbf{X} + \mathbf{B}\mathbf{U} \\ \mathbf{Y} = \mathbf{C}\mathbf{X} \end{cases} \rightarrow \begin{cases} \mathbf{X} = -\mathbf{A}^{-1}\mathbf{B}\mathbf{U} \\ \mathbf{Y} = -\mathbf{C}\mathbf{A}^{-1}\mathbf{B}\mathbf{U} \end{cases} \quad (2.30)$$

$$\begin{bmatrix} 0 \\ 0 \\ 0 \end{bmatrix} = \begin{bmatrix} 0 & \frac{D}{L} & -\frac{1}{L} \\ -\frac{D}{C_1} & 0 & 0 \\ \frac{1}{C_2} & 0 & -\frac{1}{RC_2} \end{bmatrix} \begin{bmatrix} I_L \\ V_{c1} \\ V_{c2} \end{bmatrix} + \begin{bmatrix} 0 \\ 1 \\ C_1 \\ 0 \end{bmatrix} Ipv \quad (2.31)$$

$$[Vpv] = [0 \quad 1 \quad 0] \begin{bmatrix} I_L \\ V_{c1} \\ V_{c2} \end{bmatrix} \quad (2.32)$$

From (2.31) and (2.32) the steady state values or DC values of the averaged vectors  $\mathbf{x}$  and  $\mathbf{y}$  can be obtained:

$$\begin{cases} I_L = \frac{I_{pv}}{D} \\ V_{c_1} = \frac{R I_{pv}}{D^2} \\ V_{c_2} = \frac{R I_{pv}}{D} \end{cases} \quad (2.33)$$

$$V_{pv} = \frac{R I_{pv}}{D^2} \quad (2.34)$$

From (2.33) the well-known static output-to-input ratio of the Buck converter is found:

$$V_{pv} = V_{c_1} = \frac{V_{c_2}}{D} \quad (2.35)$$

However, the state variables of equation (2.25) are the mean values of the converter instantaneous variables over one switching period, and therefore, do not represent their ripple components [31]. To investigate the performance of the convert a small-signal model can be obtained. Small-signal analysis is the study of deviations from an operating point for a system subjected to small disturbances. The assumption made by this method is that the disturbances are so small that the deviation of the system can be described linearly [38].

State variables, from equation (2.25) are decomposed in DC steady-state quantities (uppercase letters) and small ac perturbations ("^") around operating point, as shown in (2.36).

$$\begin{cases} \bar{\mathbf{x}} = \mathbf{X} + \hat{\mathbf{x}} \\ \bar{\mathbf{u}} = \mathbf{U} + \hat{\mathbf{u}} \\ \bar{\mathbf{y}} = \mathbf{Y} + \hat{\mathbf{y}} \\ \bar{d} = D + \hat{d} \end{cases} \quad (2.36)$$

by substituting (2.26) and (2.36) in equation (2.25), we obtain:

$$\begin{aligned} (\dot{\mathbf{X}} + \dot{\hat{\mathbf{x}}}) = & [(D + \hat{d})\mathbf{A}_{on} + (1 - D - \hat{d})\mathbf{A}_{off}] (\mathbf{X} + \hat{\mathbf{x}}) + [(D + \hat{d})\mathbf{B}_{on} \\ & + (1 - D - \hat{d})\mathbf{B}_{off}] (\mathbf{U} + \hat{\mathbf{u}}) \end{aligned} \quad (2.37)$$

$$(\dot{\mathbf{Y}} + \dot{\hat{\mathbf{y}}}) = [(D + \hat{d})\mathbf{C}_{on} + (1 - D - \hat{d})\mathbf{C}_{off}] (\mathbf{X} + \hat{\mathbf{x}})$$

the derivative of  $\dot{\mathbf{X}}$  in steady state is zero. By rearranging terms:

$$\begin{aligned} \hat{\mathbf{x}} = & (\mathbf{A}\mathbf{X} + \mathbf{B}\mathbf{U}) + (\mathbf{A}\hat{\mathbf{x}} + \mathbf{B}\hat{\mathbf{u}}) + [(\mathbf{A}_{on} - \mathbf{A}_{off})\mathbf{X} + (\mathbf{B}_{on} - \mathbf{B}_{off})\mathbf{U}]\hat{d} \\ & + [(\mathbf{A}_{on} - \mathbf{A}_{off})\hat{\mathbf{x}} + (\mathbf{B}_{on} - \mathbf{B}_{off})\hat{\mathbf{u}}]\hat{d} \end{aligned} \quad (2.38)$$

$$(\mathbf{Y} + \hat{\mathbf{y}}) = \mathbf{C}\mathbf{X} + \mathbf{C}\hat{\mathbf{x}} + (\mathbf{C}_{on} - \mathbf{C}_{off})\mathbf{X}\hat{d} + (\mathbf{C}_{on} - \mathbf{C}_{off})\hat{\mathbf{x}}\hat{d}$$

Since DC terms  $(\mathbf{A}\mathbf{X} + \mathbf{B}\mathbf{U})$  and  $\mathbf{C}\mathbf{X}$  satisfy (2.30), they are neglected. Also, if the ac variations are much smaller than the quiescent values, then the second-order nonlinear terms of equation (2.38) can be neglected [36]. Therefore, the linearized ac model is obtained:

$$\begin{cases} \dot{\hat{x}} = A\hat{x} + B\hat{u} + [(A_{on} - A_{off})X + (B_{on} - B_{off})U]\hat{d} \\ \hat{y} = C\hat{x} + (C_{on} - C_{off})X\hat{d} \end{cases} \quad (2.39)$$

Since  $B_{on} = B_{off}$ , and  $C_{on} = C_{off}$ , they withdraw from Eq. (2.39). Furthermore, the small perturbations of the input variable  $\hat{u} = [i\hat{p}\hat{v}]$ , around the operating point can be neglected, as the input can be considered constant. Therefore, the linearized small-signal state-space averaged model is simplified to:

$$\begin{cases} \dot{\hat{x}} = A\hat{x} + M\hat{d} \\ \hat{y} = C\hat{x} \end{cases} \quad (2.40)$$

where  $M = (A_{on} - A_{off})X$ , and the small duty cycle  $\hat{d}$  is the control variable. By replacing all the vectors in (2.40) the ac model of the Buck mode converter is obtained:

$$\begin{bmatrix} \dot{\hat{i}}_L \\ \dot{\hat{v}}_{C_1} \\ \dot{\hat{v}}_{C_2} \end{bmatrix} = \begin{bmatrix} 0 & \frac{D}{L} & -\frac{1}{L} \\ -\frac{D}{C_1} & 0 & 0 \\ \frac{1}{C_2} & 0 & -\frac{1}{RC_2} \end{bmatrix} \begin{bmatrix} \hat{i}_L \\ \hat{v}_{C_1} \\ \hat{v}_{C_2} \end{bmatrix} + \begin{bmatrix} \frac{V_{C_1}}{L} \\ \frac{I_L}{C_1} \\ 0 \end{bmatrix} \hat{d} \quad (2.41)$$

$$[i\hat{p}\hat{v}] = [0 \quad 1 \quad 0] \begin{bmatrix} \hat{i}_L \\ \hat{v}_{C_1} \\ \hat{v}_{C_2} \end{bmatrix} \quad (2.42)$$

From steady state equations (2.33) – (2.34), it is observed that a decrease in the duty ratio would increase the input voltage and output current. Therefore, the application of a conventional negative feedback control does not work desirably but resembles positive feedback [8]. The application of positive feedback control equals dynamically to the inversion of the switch control signal [30].

Generally, control variable  $\hat{d}$  is used in voltage-mode DC-DC converters. However, it is more convenient to obtain an equation model whose control variable is  $\hat{d}' = -\hat{d}$  the ac variations of the complement of the duty cycle ( $d' = 1 - d = D' - \hat{d} = D' + \hat{d}'$ ), since positive variations of  $d$  produce negative variations of input voltage [14]. Therefore, the small-signal state-space model of the converter for small decrements of the control variable  $\hat{d}'$  becomes [39]:

$$\begin{bmatrix} \dot{\hat{i}}_L \\ \dot{\hat{v}}_{C_1} \\ \dot{\hat{v}}_{C_2} \end{bmatrix} = \begin{bmatrix} 0 & \frac{D}{L} & -\frac{1}{L} \\ -\frac{D}{C_1} & 0 & 0 \\ \frac{1}{C_2} & 0 & -\frac{1}{RC_2} \end{bmatrix} \begin{bmatrix} \hat{i}_L \\ \hat{v}_{C_1} \\ \hat{v}_{C_2} \end{bmatrix} + \begin{bmatrix} -\frac{V_{C_1}}{L} \\ \frac{I_L}{C_1} \\ 0 \end{bmatrix} \hat{d}' \quad (2.43)$$

$$[i\hat{p}\hat{v}] = [0 \quad 1 \quad 0] \begin{bmatrix} \hat{i}_L \\ \hat{v}_{C_1} \\ \hat{v}_{C_2} \end{bmatrix} \quad (2.44)$$

Finally, the small-signal transfer function that describes the dynamic behavior of the converter input voltage near the operating point can be obtained. Applying the Laplace transformation to the small-signal state-space in (2.40) and manipulating the equation, yields:

$$\begin{cases} \dot{\hat{x}} = (sI - A)^{-1}M\hat{d}' \\ \hat{y} = C\hat{x} \end{cases} \rightarrow \frac{\hat{y}}{\hat{d}'} = C(sI - A)^{-1}M \quad (2.45)$$

therefore, by substituting the variables, the control to input voltage transfer function is:

$$\frac{\widehat{v}_{pv}}{\hat{d}'} = \frac{\frac{Vc_2}{RC_1} \left[ s^2 + \left( \frac{R}{L} + \frac{1}{RC_2} \right) s + \frac{2}{LC_2} \right]}{s^3 + \frac{1}{RC_2} s^2 + \left( \frac{1}{LC_2} + \frac{D^2}{LC_1} \right) s + \frac{D^2}{RLC_1C_2}} \quad (2.46)$$

In **Boost** mode, when S1 is always on and S2 switches on and off, its equivalent circuit for each switching state is represented by Fig. 2.16.

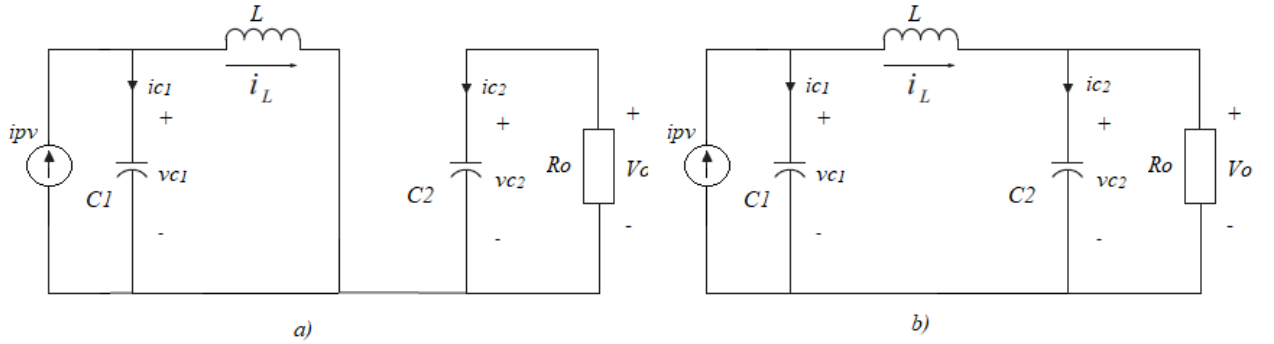


Fig. 2.16. Non-inverting Buck-Boost converter in Boost mode: a) switch S2 is on; b) switch S2 is off.

During the time interval  $dT$  when the switch is on, equations directly given in state-space form are:

$$\begin{cases} \dot{x} = A_{on}x + B_{on}u \\ y = C_{on}x + D_{on}u \end{cases}, \quad x = \begin{bmatrix} i_L \\ v_{c1} \\ v_{c2} \end{bmatrix}, \quad u = [ipv], \quad y = [vpv] \quad (2.47)$$

$$\begin{bmatrix} \dot{i}_L \\ \dot{v}_{c1} \\ \dot{v}_{c2} \end{bmatrix} = \begin{bmatrix} 0 & \frac{1}{L} & 0 \\ -\frac{1}{C_1} & 0 & 0 \\ 0 & 0 & -\frac{1}{RC_2} \end{bmatrix} \begin{bmatrix} i_L \\ v_{c1} \\ v_{c2} \end{bmatrix} + \begin{bmatrix} 0 \\ 1 \\ 0 \end{bmatrix} ipv \quad (2.48)$$

$$[vpv] = [0 \quad 1 \quad 0] \begin{bmatrix} i_L \\ v_{c1} \\ v_{c2} \end{bmatrix} \quad (2.49)$$

During the second subinterval  $(1 - d)T$ , when the switch is off, state-space equations are:

$$\begin{cases} \dot{x} = A_{off}x + B_{off}u \\ y = C_{off}x + D_{off}u \end{cases} \quad (2.50)$$

$$\begin{bmatrix} \dot{i}_L \\ \dot{v}_{c_1} \\ \dot{v}_{c_2} \end{bmatrix} = \begin{bmatrix} 0 & \frac{1}{L} & -\frac{1}{L} \\ -\frac{1}{C_1} & 0 & 0 \\ \frac{1}{C_2} & 0 & -\frac{1}{RC_2} \end{bmatrix} \begin{bmatrix} i_L \\ v_{c_1} \\ v_{c_2} \end{bmatrix} + \begin{bmatrix} 0 \\ \frac{1}{C_1} \\ 0 \end{bmatrix} ipv \quad (2.51)$$

$$[vpv] = [0 \quad 1 \quad 0] \begin{bmatrix} i_L \\ v_{c_1} \\ v_{c_2} \end{bmatrix} \quad (2.52)$$

As for the Buck mode converter, applying the averaging technic the state-space averaged equations can be derived:

$$\begin{cases} \dot{\bar{x}} = \mathbf{A}\bar{x} + \mathbf{B}\bar{u} \\ \bar{y} = \mathbf{C}\bar{x} + \mathbf{D}\bar{u} \end{cases} \quad (2.53)$$

$$\begin{bmatrix} \dot{\bar{i}}_L \\ \dot{\bar{v}}_{c_1} \\ \dot{\bar{v}}_{c_2} \end{bmatrix} = \begin{bmatrix} 0 & \frac{1}{L} & -\frac{(1-d)}{L} \\ -\frac{1}{C_1} & 0 & 0 \\ \frac{(1-d)}{C_2} & 0 & -\frac{1}{RC_2} \end{bmatrix} \begin{bmatrix} \bar{i}_L \\ \bar{v}_{c_1} \\ \bar{v}_{c_2} \end{bmatrix} + \begin{bmatrix} 0 \\ \frac{1}{C_1} \\ 0 \end{bmatrix} \bar{ipv} \quad (2.54)$$

$$[\bar{vpv}] = [0 \quad 1 \quad 0] \begin{bmatrix} \bar{i}_L \\ \bar{v}_{c_1} \\ \bar{v}_{c_2} \end{bmatrix} \quad (2.55)$$

Where  $\bar{x}$ ,  $\bar{u}$  and  $\bar{y}$  are the averaged vectors over a switching period, and  $\mathbf{A}$ ,  $\mathbf{B}$ ,  $\mathbf{C}$ ,  $\mathbf{D}$  are the averaged matrices, calculated as in (2.26).

By considering zero perturbation, the steady-state operation of the converter is obtained:

$$\begin{cases} \mathbf{0} = \mathbf{A}\mathbf{X} + \mathbf{B}\mathbf{U} \\ \mathbf{Y} = \mathbf{C}\mathbf{X} \end{cases} \rightarrow \begin{cases} \mathbf{X} = -\mathbf{A}^{-1}\mathbf{B}\mathbf{U} \\ \mathbf{Y} = -\mathbf{C}\mathbf{A}^{-1}\mathbf{B}\mathbf{U} \end{cases} \quad (2.56)$$

$$\begin{bmatrix} 0 \\ 0 \\ 0 \end{bmatrix} = \begin{bmatrix} 0 & \frac{1}{L} & -\frac{(1-D)}{L} \\ -\frac{1}{C_1} & 0 & 0 \\ \frac{(1-D)}{C_2} & 0 & -\frac{1}{RC_2} \end{bmatrix} \begin{bmatrix} I_L \\ V_{c_1} \\ V_{c_2} \end{bmatrix} + \begin{bmatrix} 0 \\ \frac{1}{C_1} \\ 0 \end{bmatrix} IpV \quad (2.57)$$

$$[VpV] = [0 \quad 1 \quad 0] \begin{bmatrix} I_L \\ V_{c_1} \\ V_{c_2} \end{bmatrix} \quad (2.58)$$

At the equilibrium, the state variables become the averaged values  $V_{c_1}$ ,  $V_{c_2}$  and  $I_L$ :

$$\begin{cases} I_L = Ipv \\ V_{c_1} = (1 - D)^2 RIpv \\ V_{c_2} = (1 - D)RIpv \end{cases} \quad (2.59)$$

$$Vpv = (1 - D)^2 RIpv \quad (2.60)$$

From (2.59) the well-known static input-to-output ratio of the Boost converter is found:

$$V_{c_2} = \frac{V_{c_1}}{(1 - D)} = \frac{Vpv}{(1 - D)} \quad (2.61)$$

As in (2.41) the linearized small-signal state-space model is obtained:

$$\begin{cases} \dot{\hat{x}} = A\hat{x} + B\hat{u} + [(A_{on} - A_{off})X + (B_{on} - B_{off})U]\hat{d} \\ \hat{y} = C\hat{x} + (C_{on} - C_{off})X\hat{d} \end{cases} \quad (2.62)$$

where “^” variables indicate ac perturbations and uppercase variables are the DC quantities. As for the Buck converter  $B_{on} = B_{off}$ ,  $C_{on} = C_{off}$  and neglecting the ac variations of the input variable  $\hat{u} = [i\hat{p}v]$ , the ac state-space model is simplified to:

$$\begin{cases} \dot{\hat{x}} = A\hat{x} + (A_{on} - A_{off})X\hat{d} \\ \hat{y} = C\hat{x} \end{cases} \quad (2.63)$$

$$\begin{bmatrix} \dot{\hat{i}}_L \\ \dot{\hat{v}}_{c_1} \\ \dot{\hat{v}}_{c_2} \end{bmatrix} = \begin{bmatrix} 0 & \frac{1}{L} & -\frac{(1-D)}{L} \\ -\frac{1}{C_1} & 0 & 0 \\ \frac{(1-D)}{C_2} & 0 & -\frac{1}{RC_2} \end{bmatrix} \begin{bmatrix} \hat{i}_L \\ \hat{v}_{c_1} \\ \hat{v}_{c_2} \end{bmatrix} + \begin{bmatrix} \frac{V_{c_2}}{L} \\ 0 \\ -\frac{I_L}{C_2} \end{bmatrix} \hat{d} \quad (2.64)$$

$$[i\hat{p}v] = [0 \quad 1 \quad 0] \begin{bmatrix} \hat{i}_L \\ \hat{v}_{c_1} \\ \hat{v}_{c_2} \end{bmatrix} \quad (2.65)$$

From equation (2.59) it can be seen that the output current  $I_o = (1 - D)Ipv$  and the output voltage  $V_{c_2}$ , are inversely proportional to the duty ratio. Therefore, the small-signal state-space model can be written with the control variable  $\hat{d}' = -\hat{d}$ , because negative variations of duty cycle cause positive increments in the input voltage [12].

$$\begin{bmatrix} \dot{\hat{i}}_L \\ \dot{\hat{v}}_{c_1} \\ \dot{\hat{v}}_{c_2} \end{bmatrix} = \begin{bmatrix} 0 & \frac{1}{L} & -\frac{(1-D)}{L} \\ -\frac{1}{C_1} & 0 & 0 \\ \frac{(1-D)}{C_2} & 0 & -\frac{1}{RC_2} \end{bmatrix} \begin{bmatrix} \hat{i}_L \\ \hat{v}_{c_1} \\ \hat{v}_{c_2} \end{bmatrix} + \begin{bmatrix} -\frac{V_{c_2}}{L} \\ 0 \\ \frac{I_L}{C_2} \end{bmatrix} \hat{d}' \quad (2.66)$$

$$[\widehat{v}_{pv}] = [0 \quad 1 \quad 0] \begin{bmatrix} \widehat{i}_L \\ \widehat{v}_{C_1} \\ \widehat{v}_{C_2} \end{bmatrix} \quad (2.67)$$

Applying the Laplace transformation and manipulating the equations, the small-signal control to input voltage transfer function is obtained:

$$\frac{\widehat{v}_{pv}}{\widehat{d}'} = \frac{\frac{V_{C_2}}{LC_1} \left( s + \frac{2}{RC_2} \right)}{s^3 + \frac{1}{RC_2} s^2 + \left( \frac{1-D}{LC_2} + \frac{1}{LC_1} \right) s + \frac{1}{RLC_1C_2}} \quad (2.68)$$

### 2.2.5 Converter Design

The results of the dynamic analysis of the small-signal model indicate that the converter is highly dependent on the operating region of the PV system and on the duty ratio command. To maximize the efficiency of the non-inverting Buck-Boost converter, the system is designed such that the converter is operated in CCM [17]. The design of the non-inverting Buck-Boost converter is same as the Buck design and Boost design, since these are the two modes of operation of the converter. The electrical specifications and parameters shown in Table 4 are used to design the components of the proposed converter [40].

**Table 4.** Converter specifications.

Deign parameters	Target values
Input voltage, $V_{in}$	2 – 21 V
Output voltage, $V_o$	12 V
Output power, $P_o$	8 – 80 W
Switching frequency, $f_s$	20 kHz
Output voltage ripple, $\Delta v_o$	120 mV (1% of $V_o$ )

When the non-inverting Buck-Boost converter operates under Buck mode, the variation range of duty cycle, according to (2.35), is:

$$D_{max} = \frac{V_o}{V_{in_{min}}} = \frac{12}{12} = 1 \quad (2.69)$$

$$D_{min} = \frac{V_o}{V_{in_{max}}} = \frac{12}{21} = 0.5714 \quad (2.70)$$

Duty cycles are important because at these values the converter is operating at the extremes of its operating range. As a design guideline, the output filter inductance should be designed to ensure the inductance current ripple  $\Delta i_L$ , be 20% of  $I_{o_{max}}$ , which means that the converter operates in critical current mode (CRM) at 10% of  $I_{o_{max}}$ , as clarified in Fig. 2.17.

$$\Delta i_L = 0.2 \cdot I_{o_{max}} = 2 \cdot I_{o_{CRM}} \quad (2.71)$$

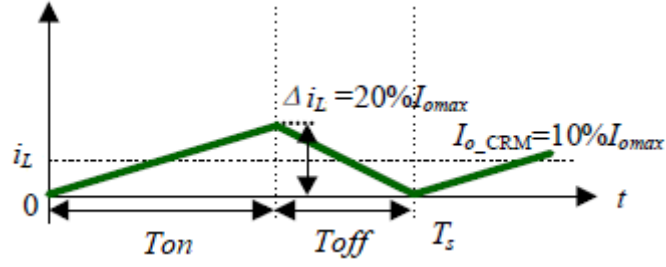


Fig. 2.17. Inductance current waveform under critical current mode (CRM).

Therefore, the Buck converter operates in CCM for  $L > L_{min}$ , where:

$$L_{min} = \frac{(1 - D_{min})V_o}{\Delta i_L f_s} = \frac{(1 - D_{min})V_o}{2I_{o_{min}} f_s} = \frac{(1 - D_{min})V_o^2}{2P_{o_{min}} f_s} \quad (2.72)$$

substituting the parameters, the minimum inductance in Buck mode is calculated as:

$$L_{min_{Buck}} = \frac{(1 - D_{min})V_o^2}{2P_{o_{min}} f_s} = \frac{(1 - 0.5714) * 12^2}{2 * 8 * 20 * 10^3} = 0.1928mH \quad (2.73)$$

In the same way, when the converter operates under Boost mode, the variation range of the duty cycle, according to (2.61), is:

$$D_{max} = \frac{V_o - V_{in_{min}}}{V_o} = \frac{12 - 2}{12} = 0.8333 \quad (2.74)$$

$$D_{min} = \frac{V_o - V_{in_{max}}}{V_o} = \frac{12 - 12}{21} = 0 \quad (2.75)$$

The Boost inductance is designed to ensure the converter operates in CCM, therefore:

$$L_{min} = \frac{D(1 - D)^2 V_o}{2I_{o_{min}} f_s} = \frac{D(1 - D)^2 V_o^2}{2P_{o_{min}} f_s} \quad (2.76)$$

The duty cycle in which the  $L_{min}$  of (2.76) possesses the maximum value must be determined. From Fig. 2.18, where equation (2.76) function of  $D$  is plotted, it can be seen that the function achieves the maximum value solution for  $D = 1/3$  [40].

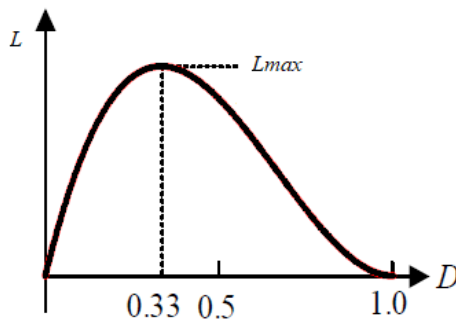


Fig. 2.18. Diagram of  $L_{min}$  function of duty cycle  $D$ .

Subsequently, the minimum inductance under Boost mode can be calculated as:

$$L_{min_{Boost}} = \frac{D(1-D)^2 V_o^2}{2P_{o_{min}} f_s} = \frac{\frac{1}{3} \left(1 - \frac{1}{3}\right)^2 * 12^2}{2 * 8 * 20 * 10^3} = 0.0667mH \quad (2.77)$$

There is only one inductor in the non-inverting Buck-Boost converter, therefore a value that satisfies both Buck and Boost mode conditions must be selected. To assure a continuous current of the inductor in either modes, the larger one of (2.73) and (2.77) is chosen [27]. In practice, for safety reason, the chosen one is multiplied by 1.25. This process ensures that the inductor current can be operated under CCM. Thus, for CCM the minimum inductance required became:

$$L_{min} = 1.25 \cdot L_{min_{Buck}} = 1.25 \cdot 0.1928mH = 0.241mH \quad (2.78)$$

For the capacitor selection, a solution that satisfies both Buck and Boost mode must be chosen [41]. For Buck mode, the minimum output capacitor value for a desired output voltage ripple, is calculated:

$$C_{min_{Buck}} = \frac{(1 - D_{min})V_o}{8f_s^2 L_{min} \Delta V_o} = \frac{(1 - 0.5714)}{8 * 20^2 * 10^6 * 0.241 * 10^{-3} * 0.01} = 55.58\mu F \quad (2.79)$$

For Boost mode, according to the specification requirements of output voltage ripple, the size of the output capacitor value can be determined as [19]:

$$C_{min_{Boost}} = \frac{D I_{o_{min}}}{f_s \Delta V_o} = \frac{D P_{o_{min}}}{f_s \Delta V_o V_o} = \frac{0.333 * 8}{20 * 10^3 * 0.120 * 12} = 92.6\mu F \quad (2.80)$$

The larger minimum required capacitance is selected and multiplied by 1.25 for safety reasons:

$$C_{min} = 1.25 \cdot C_{min_{Boost}} = 1.25 \cdot 92.6\mu F \approx 116\mu F \quad (2.81)$$

The above design was conducted for the worst-case condition of the Buck mode and the Boost mode, according to Power Electronics. Since the converter is forced to work under MPPT, a proper components design should consider the maximum operating point. The electrical specifications and parameters of the converter at the MPP operation are shown in Table 5.

**Table 5.** MPPT specifications.

Deign parameters	Target values
Input voltage, $V_{mpp}$	16.8 V
Output voltage, $V_o$	12 V
Output power, $P_{mpp}$	79.8 W
Switching frequency, $f_s$	20 kHz
Output voltage ripple, $\Delta v_o$	120 mV (1% of $V_o$ )

At the MPP the converter works in Buck mode, therefore the duty cycle is calculated as:

$$D = \frac{V_o}{V_{mpp}} = \frac{12}{16.8} = 0.7143 \quad (2.82)$$

The required inductance is calculated as:

$$L_{mpp} = \frac{(1-D)V_o^2}{2P_{mpp} f_s} = \frac{(1-0.7143) * 12^2}{2 * 79.8 * 20 * 10^3} = 0.013mH \quad (2.83)$$

The output capacitor value, that results in the desired voltage ripple is given by:

$$C_{mpp} = \frac{(1-D)V_o}{8f_s^2 L_{min} \Delta V_o} = \frac{(1-0.7143)}{8 * 20^2 * 10^6 * 0.013 * 10^{-3} * 0.01} \approx 687\mu H \quad (2.84)$$

About the input capacitor, it was chosen as equal as the output capacitor. The minimum value of the input capacitor is necessary to stabilize the input voltage due to the peak current requirement of a switching power supply. The value can be increased if the input voltage is noisy [41].

For the simulation slightly higher values of  $L$  and  $C$  were chosen.  $L = 0.33mH$  and  $C = 700\mu F$ .

## 2.2.6 Validation of the Dynamic Model with Trapezoidal Method

Time domain simulation of switching converters is an essential stage during the design, implementation and development of a DC-DC converter [42]. Generally, numerical integration methods are used to find numerical approximations to the solutions of ordinary differential equations (ODEs). Different numerical methods can be used to perform time domain simulation of the converters. The simplest numerical method is the *forward Euler*, where a general first order differential equation can be approximated as a forward finite difference [43]:

$$f(x, t) = \frac{dx}{dt} \approx \frac{x(t + \Delta t) - x(t)}{\Delta t} \quad (2.85)$$

which rearranged becomes:

$$x(t + \Delta t) = x(t) + \Delta t f(x, t) \quad (2.86)$$

The forward Euler is an explicit method, meaning that the new value  $x(t + \Delta t)$  is defined in terms of things that are already known, like  $x(t)$ . However, if instead of (2.85), the approximation explained below is used:

$$f(x, t) = \frac{dx}{dt} \approx \frac{x(t) - x(t - \Delta t)}{\Delta t} \quad (2.87)$$

the *backward Euler* method is obtained [43], that is:

$$x(t + \Delta t) = x(t) + \Delta t f(x + \Delta x, t + \Delta t) \quad (2.88)$$

The backward Euler method is an implicit method, meaning that an equation must be solved to find  $x(t + \Delta t)$ . Another widely used method is the *trapezoid rule*, which, as the name says, approximates the integration using a trapezoid. The trapezoidal rule is given by the formula [44]:

$$x(t + \Delta t) = x(t) + \frac{\Delta t}{2} (f(x, t) + f(x + \Delta x, t + \Delta t)) \quad (2.89)$$

Trapezoidal rule is superior to both Euler rules. Its most salient properties are numerical stability and accuracy [45]. The Euler methods might not always estimate the state values accurately [42], therefore, the trapezoid rule which increases the estimation accuracy should be used. It correctly predicts the system behavior and position of poles of discrete system at lower frequencies, that may have a significant effect on compensator design for DC-DC converter [46].

Other well-known but more complicated numerical methods, such as Runge-Kutta, higher order Adams-Moulton, etc., can also be used for real-time simulation. All those methods can be implemented using any computer language programs or mathematical tools.

The non-inverting Buck-Boost converter was modeled using state-space equations. For the solution of state-equations, trapezoidal integration is performed to obtain a discrete-time model from a continuous-time one [47]. In each of the switching mode (on/off), the converter can be represented in state-space form by:

$$\dot{\mathbf{x}}(t) = \mathbf{A}\mathbf{x}(t) + \mathbf{B}\mathbf{u}(t) \quad (2.90)$$

Using the trapezoidal rule of integration, (2.90) is transformed to a set of difference equations [48]:

$$\begin{aligned} \mathbf{x}(t) = \mathbf{x}(t - \Delta t) + \frac{\Delta t}{2} [\mathbf{A}(t - \Delta t)\mathbf{x}(t - \Delta t) + \mathbf{A}(t)\mathbf{x}(t)] \\ + \frac{\Delta t}{2} [\mathbf{B}(t - \Delta t)\mathbf{u}(t - \Delta t) + \mathbf{B}(t)\mathbf{u}(t)] \end{aligned} \quad (2.91)$$

where  $\Delta t$ , is the step length. The above equation can be rearranged as:

$$\begin{aligned} \mathbf{x}(t) = \left( \mathbf{I} - \frac{\Delta t}{2} \mathbf{A}(t) \right)^{-1} \left\{ \left( \mathbf{I} + \frac{\Delta t}{2} \mathbf{A}(t - \Delta t) \right) \mathbf{x}(t - \Delta t) \right. \\ \left. + \frac{\Delta t}{2} [\mathbf{B}(t - \Delta t)\mathbf{u}(t - \Delta t) + \mathbf{B}(t)\mathbf{u}(t)] \right\} \end{aligned} \quad (2.92)$$

where  $\mathbf{I}$ , is the identity matrix.

In power electronics,  $\mathbf{A}$  and  $\mathbf{B}$  change when circuit state changes. Therefore, for any circuit state over an interval during which the state is not changing, those matrices are independent of time.

$$\mathbf{x}(t) = \left( \mathbf{I} - \frac{\Delta t}{2} \mathbf{A} \right)^{-1} \left( \mathbf{I} + \frac{\Delta t}{2} \mathbf{A} \right) \mathbf{x}(t - \Delta t) + \left( \mathbf{I} - \frac{\Delta t}{2} \mathbf{A} \right)^{-1} \frac{\Delta t}{2} \mathbf{B} [\mathbf{u}(t - \Delta t) + \mathbf{u}(t)] \quad (2.93)$$

Thus, the desired approximate solution of (2.90) can be written as:

$$\mathbf{x}(t) = \mathbf{M}\mathbf{x}(t - \Delta t) + \mathbf{N}[\mathbf{u}(t - \Delta t) + \mathbf{u}(t)] \quad (2.94)$$

where  $\mathbf{M} = \left(\mathbf{I} - \frac{\Delta t}{2}\mathbf{A}\right)^{-1} \left(\mathbf{I} + \frac{\Delta t}{2}\mathbf{A}\right)$  and  $\mathbf{N} = \left(\mathbf{I} - \frac{\Delta t}{2}\mathbf{A}\right)^{-1} \frac{\Delta t}{2}\mathbf{B}$ , are real matrices to be calculated only once for any circuit state as  $\Delta t$  is constant. Since the subinterval in which the Buck converter is in on-state (S1 on) is equal to the subinterval in which the Boost is in off-state (S2 off), only three state are needed to simulate the response of the system.

The numerical method presented is used to simulate the non-inverting Buck-Boost converter on MATLAB (file script in **Appendix A.3**) and the results are shown in Figs. 2.19 and 2.20.

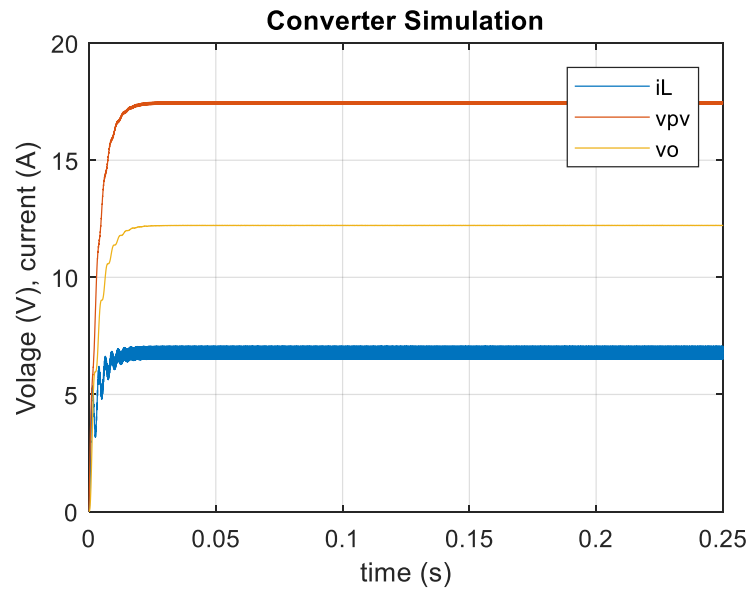


Fig. 2.19. Real-time simulation of non-inverting Buck-Boost converter operating in Buck mode when  $D = 0.7$ .

Fig. 2.19 shows the output voltage  $v_o$ , the input voltage  $v_{pv}$ , and the inductance current  $i_L$ , responses of the converter working in Buck mode, simulated for constant input current and  $D = 0.7$ .

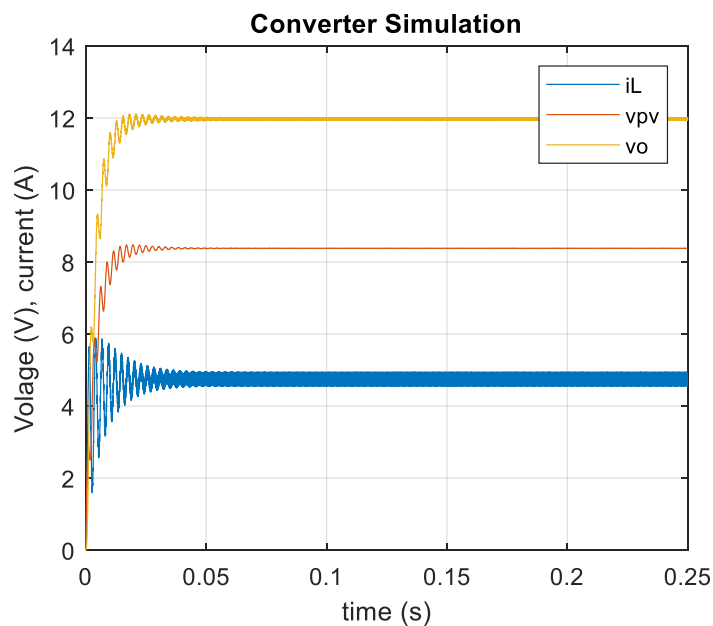


Fig. 2.20. Real-time simulation of non-inverting Buck-Boost converter operating in Boost mode when  $D = 0.3$ .

Fig. 2.20 shows the time-domain simulation of the converter working in Boost mode when  $D = 0.3$  and with  $R = 3.6\Omega$  (resistive load). The top waveform is the output voltage  $v_o$ , and the bottom waveforms are input voltage  $v_{pv}$ , and inductance current  $i_L$ , respectively. The simulations are carried out with a time step of  $50\mu s$  [49].

The results show that the proposed trapezoidal method can successfully model a switching converter in time domain. The resulting model can be implemented and executed together with a controller to perform a complete closed-loop time domain simulation [42].

## 2.3 Battery Energy Storage (BES)

PV generation is developing increasingly fast as a renewable energy source, because of the cost-effective and the environmentally friendly characteristics [7]. However, the output delivered by the arrays depends greatly on weather conditions, making PV generation an intermittent and uncertain source of power [50]. Supplying the customers with a quality power is a challenging issue in a stand-alone PV system [4]. Thus, the battery energy storage is a necessary element to help improving the stability and the reliability of the system, since the battery can store the excess energy and provide it at times of deficiency, ensuring the energy balance of the PV system [51].

To investigate battery performance, effective battery models are critically needed [52].

### 2.3.1 Battery Model

There are basically three types of battery models: experimental, electrochemical and electric circuit-based [53]. The first two, experimental and electrochemical, are very accurate models primarily utilized when designing the battery packaging [54]. However, those models are not well suited to represent cell dynamics since simulation can be quite time consuming [53]. Circuit-based battery models are electrical equivalent models using a combination of voltage source, resistors and capacitors to model battery performance [52]. Those models are simple and can represent steady-state and dynamic battery behavior [55], therefore are the most suitable for dynamic simulation [7].

The simplest electric model consists of an ideal voltage source  $V_o$ , in series with an internal resistance  $R_b$ , as shown in Fig. 2.21 [56].

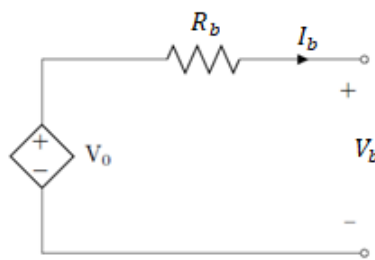


Fig. 2.21. Circuit diagram of a simple linear battery model.

This model, however, does not consider the state of charge (SOC) of the battery which is assumed to have unlimited energy. Therefore, is not suitable if the available voltage at different charge levels is of interest [56]. Other equivalent models are based on an open-circuit voltage in series with resistance and parallel RC circuits. Although these models are more accurate than the simple linear battery model, the identification of all the parameters is much more complicated [53].

It is necessary to identify a model that estimates the SOC accurately as it is important for the purposes of converter control [51]. Accurate modelling of a battery is a very complex task that requires

knowledge of the electrochemical processes. For simulation purposes, a model that accounts for the varying voltage that is available based on the SOC is sufficient [56].

An easy-to-use battery model applied for dynamic simulation software is presented in [53]. This model considers the SOC as the only state variable, however the model is only valid in steady state (constant current) [57]. As shown in Fig. 2.22, the model is composed of a controlled voltage source in series with a constant resistance. This model assumes the same characteristics for the charge and the discharge cycles.

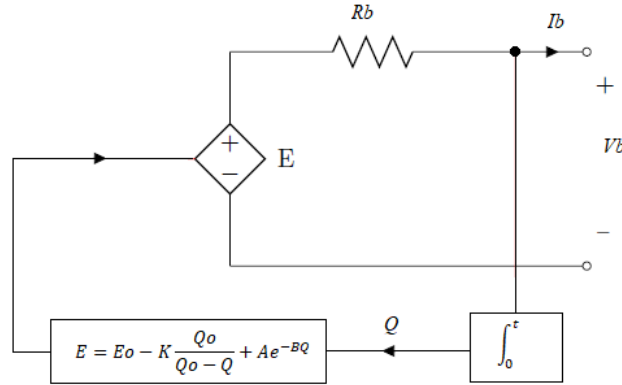


Fig. 2.22. Circuit diagram of battery model with controlled voltage source.

The controlled voltage source dependent on the actual SOC of the battery is calculated with the equation:

$$E = E_o - K \frac{Q_o}{Q_o - Q} + Ae^{-BQ} \quad (2.95)$$

where,  $E$  is the no-load voltage (V),  $E_o$  is the battery constant voltage (V),  $K$  is the polarization voltage (V),  $Q_o$  is the nominal battery capacity (Ah),  $A$  is the exponential zone amplitude (V),  $B$  is the exponential zone time constant inverse (Ah)<sup>-1</sup> and  $Q$  is the actual battery charge (Ah), calculated integrating the battery current  $I_b$  (A) and adding the initial charge  $Q_{in}$  (Ah), as:

$$Q = Q_{in} + \int_0^t -I_b dt \quad (2.96)$$

The minus in the integral in (2.96) means that the current is assumed to be positive when the battery is discharged, resulting in a reducing total charge of the battery, and assumed to be negative when the battery is charged resulting in an increasing of the total charge [56].

Finally, the battery voltage of the model is calculated as:

$$V_b = E - R_b I_b \quad (2.97)$$

The presented model is based on several approximations and assumptions [53]:

- the internal resistance  $R_b$ , is assumed to be constant during both charging and discharging, and independent on current amplitude;
- charge characteristic is assumed to be the same as the discharge characteristic;
- the battery capacity is assumed constant (independent of the current amplitude);
- temperature effect is not included;

- self-discharge is not considered.

The power of this model is that all the parameters needed can easily be extracted from the manufacturer's discharge curve. A typical discharge characteristic is shown in Fig. 2.23.

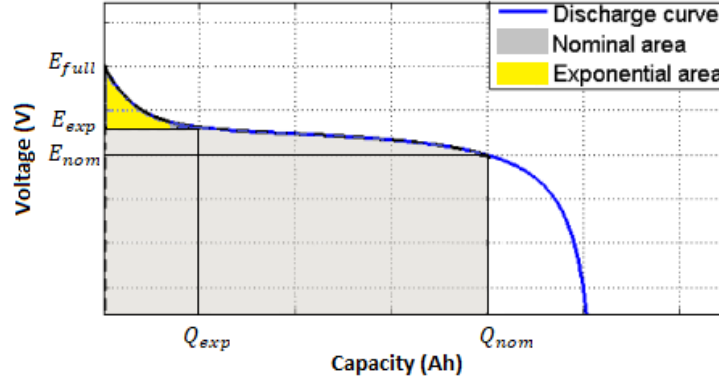


Fig. 2.23. Typical battery discharge curve.

Only three points on the discharge curve, shown in Fig. 2.23, are required to obtain the parameters: the point of fully charged voltage  $(0, E_{full})$ , the end of exponential zone  $(Q_{exp}, E_{exp})$  and the end of nominal zone  $(Q_{nom}, E_{nom})$ . Therefore, the following battery parameters can be calculated based on these three points:

$$A = E_{full} - E_{exp} \quad (2.98)$$

$$B = \frac{3}{Q_{exp}} \quad (2.99)$$

$$K = \frac{[E_{full} - E_{nom} + A(e^{-BQ_{exp}} - 1)] (Q_0 - Q_{nom})}{Q_{nom}} \quad (2.100)$$

$$E_0 = E_{full} + K + R_b I_b - A \quad (2.101)$$

The internal resistance  $R_b$ , is usually provided by manufacturer's datasheet.

Obviously, with this approach the parameters are approximated but still it is a very useful method for modelling the battery, with a level of accuracy that is sufficient for the purpose of this thesis.

### 2.3.2 Battery Model Validation

This approach, that use only SOC as a state variable is very general, so it can be applied to many types of battery, as explained in [53]. The model parameters extracted from manufacture's datasheet of a Panasonic HHR650D3 NiMH battery cell, are shown in table 6.

**Table 6.** Panasonic HHR650D3 Nickel-Metal-Hybrid parameters.

Parameters	Values
Nominal voltage	1.2 V
Nominal capacity	6.5 Ah
$R_b$	0.0046 $\Omega$

$E_{full}$	1.4 V
$E_{exp}$	1.25 V
$E_{nom}$	1.2 V
$Q_{exp}$	1.3 Ah
$Q_{nom}$	5.2 Ah
$K$	0.0125 V
$A$	0.15 V
$B$	2.3077 Ah <sup>-1</sup>

The parameters presented in table 6 are extracted from manufacturer's discharge curve at 1.3A. To validate whether the obtained values accurately represent the real behavior of the battery, the model with all the equations of the previous section and the parameters of table 6 are integrated and simulated in MATLAB (file script in **Appendix A.4**). The simulated charging and discharging cell voltage curve function of the SOC is visualized in Fig. 2.24. The curve is obtained for a constant battery current  $I_b$ , of 1.3A.

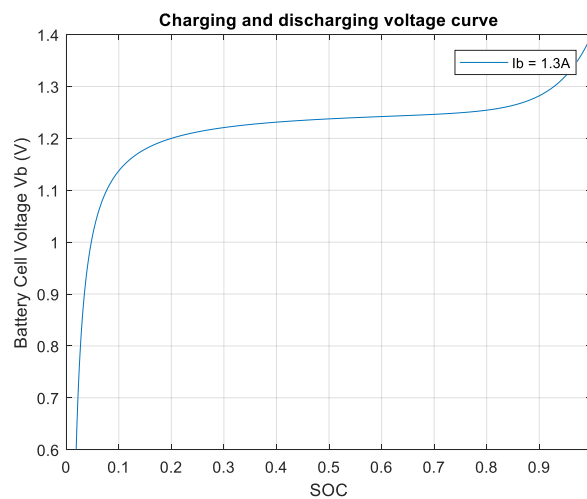


Fig. 2.24. Charging and discharging voltage curve function of SOC.

To validate the battery model, the discharge voltage curve function of time is plotted and compared with the discharge characteristic taken from the datasheet, as shown in Fig. 2.25.

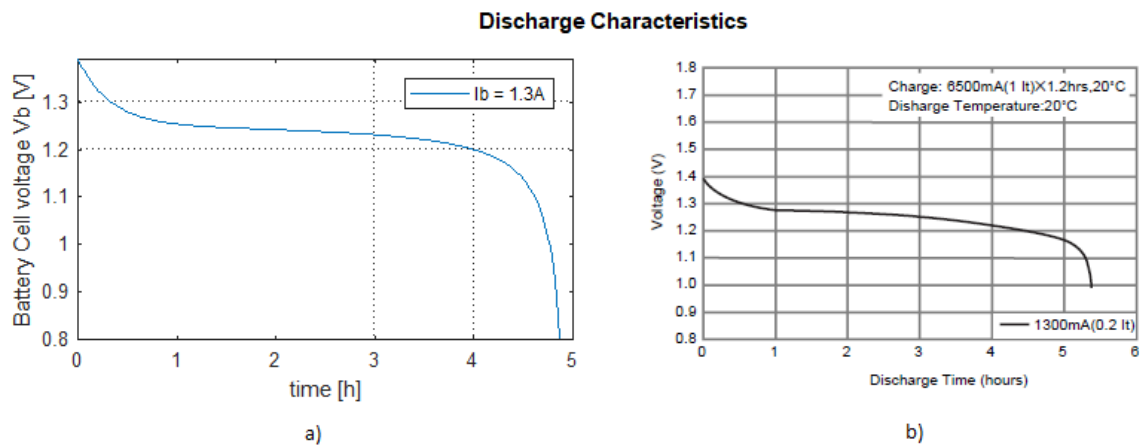


Fig. 2.25. Discharge characteristics curves of the battery at 1.3A discharge current: a) simulation model; b) manufacturer's datasheet.

Moreover, the simulated curves and the manufacturing curves for different discharge currents are plotted and compared in Fig. 2.26.

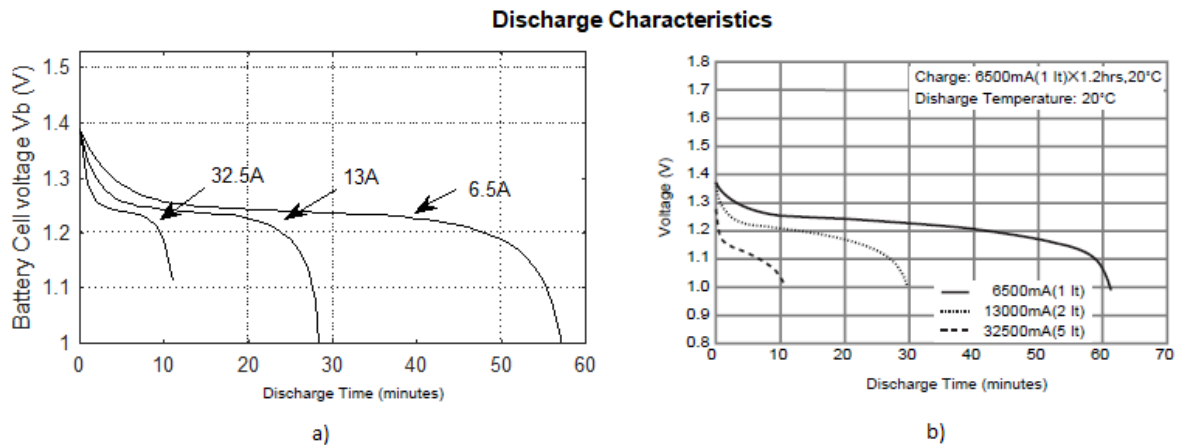


Fig. 2.26. Discharge characteristics of the battery at different discharge currents: a) simulation model; b) manufacturer's datasheet.

Even though the results of the simulated model show a slightly different shapes compared to the datasheet curves, from Figs. 2.25 and 2.26, it can be seen that the proposed model can properly represent the real behavior of the battery cell considered.

### 2.3.3 Battery Sizing

The approach described can be used to extract parameters for other batteries types.

Of the wide variety of battery chemistries available, the major types of rechargeable batteries used or being considered for solar system applications are Lead-acid, Nickel-metal-hydride (NiMH) and Lithium-ion (Li-ion) [58]. Each technology has its own merits and drawbacks. The choice of a battery technology comes out from a compromise of needed characteristics such as: size, cycle life, maintenance, reliability, efficiency, overcharge tolerance, operating temperature range and cost [59].

Lead acid batteries are the most widely used rechargeable battery systems today due to their low cost, high availability and durability, while still providing reasonable performance and life characteristics [51]. This oldest and mature technology has been used for many power system applications. The main advantages of lead acid batteries are the relatively low cost, easy availability of raw materials, easy of manufacture, safety and reliability. However, low specific energy, poor temperature performance and short cycle life are the main drawbacks that obstacle their use.

Lead acid batteries can be divided into two distinct categories: flooded and valve regulated (VRLA) or sealed (SLA) batteries. In flooded batteries water is consumed through the battery life and the batteries can emit gases [60]. This necessitates the periodic maintenance (water addition to the battery), upright orientation to prevent electrolyte leakage and ventilated environment [61].

Since the main problems of conventional flooded batteries involve the liquid electrolyte, the design of the lead acid battery has been improved by the development of the maintenance-free lead acid battery that could operate in any position [62]. Two main types of sealed batteries emerged: Gel type and Absorbed Glass Mat (AGM) type. These batteries have immobilized form of electrolyte thus they have no need for water additions and successfully overcame many objections of flooded batteries, like problems of corrosion and electrolyte leakage. Therefore, sealed lead acid batteries are suitable for PV applications because of the less maintenance requirement, smaller sizes and low cost. Gel type lead

acid batteries with deep discharge cycle are the most used for standalone applications where maintenance free operation is required [60].

In some cases, Nickel-Cadmium or Nickel-metal-hydride (NiMH) batteries can be a good alternative to lead acid batteries [63]. Despite their higher cost they have longer deep cycle life, high temperature tolerance and larger energy density compared to lead acid batteries [52].

Among the batteries mentioned, Li-ion battery is the most promising technology because of its desirable features such as high specific power, high specific energy and long cycle life [58]. Li-ion batteries are very low-weight, thus make them suitable for many portable applications. However, the production costs are high, and overcharging can easily damage the battery [56].

Mainly for cost reasons, a Lead acid gel battery was chosen for the simulation of the system. In particular, Panasonic LC-R067R2P [64] 6V 7.2Ah battery type, with parameters of table 7, was considered.

**Table 7.** Panasonic LC-R067R2P Lead-Acid parameters.

Parameters	Values
Nominal voltage	6 V
Nominal capacity	7.2 Ah
$R_b$	0.02 $\Omega$
$E_{full}$	6.5 V
$E_{exp}$	6.1 V
$E_{nom}$	6 V
$Q_{exp}$	0.012 Ah
$Q_{nom}$	1.44 Ah

The simulated discharge voltage curves function of time are plotted and compared with the discharge characteristics taken from the datasheet, as shown in Fig. 2.27.

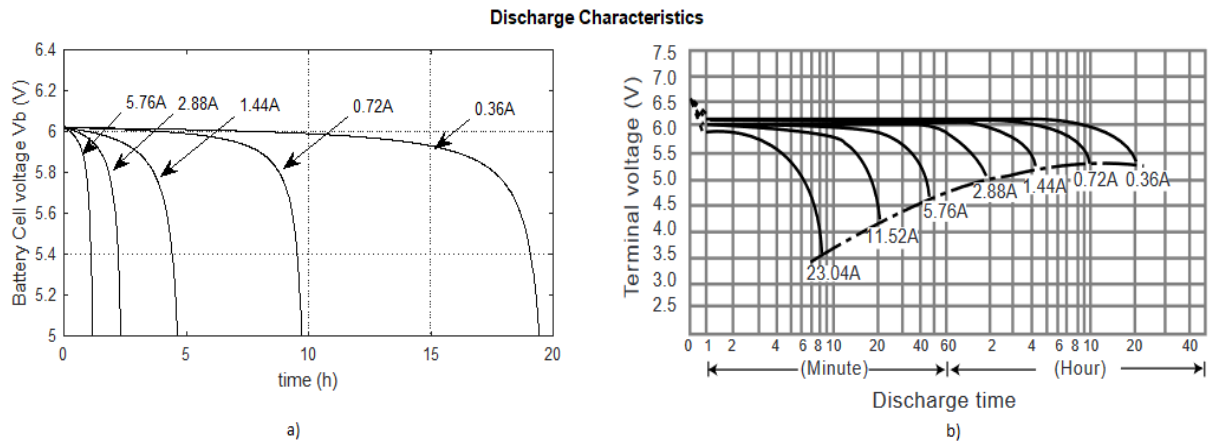


**Fig. 2.27.** Discharge characteristics of the battery at different discharge currents: a) simulation model; b) manufacturer's datasheet.

Chose the battery cell, the next step is to size the battery pack necessary to meet the requests of the PV system. To get the desired configuration, multiple cells are connected in series to increment the voltage and in parallel to increase the current. The battery pack capacity was determined considering design parameters of table 8.

**Table 8.** Battery pack design parameters.

Parameters	Values
Wh per day	168 Wh/d
Days of autonomy	1 d
Depth of discharge (DoD)	40%
Cell voltage	6 V
Cell capacity	7.2 Ah

The depth of discharge (DoD) is the dominant variable affecting the cycle life of the battery. Generally, to increase the lifetime (number of cycles), batteries are limited to 40-50% of DoD. This implies an oversizing of the design. Therefore, the battery pack capacity is calculated as [4],

$$\text{Battery pack capacity} = \frac{168 \frac{\text{Wh}}{\text{d}} * 1 \text{ d}}{6 \text{ V} * 0.4} \approx 70 \text{ Ah}$$

Hence, the number of batteries required to be connected in series and parallel are respectively,  $N_s = 1$  and  $N_p = 10$ .

To simulate the model of the battery pack, the parameters of the equivalent circuit model for a single battery cell need to be scaled. The open-circuit voltage needs to be multiplied by the number of series cells  $N_s$ . The battery current needs to be multiplied by the number of parallel branches  $N_p$ , and the resistance needs to be scaled by a factor of  $\frac{N_s}{N_p}$  [54].

The resulting voltage characteristic, of the modelled battery pack, function of the SOC is shown in Fig. 2.28. MATLAB code used for the simulation of the battery pack model is presented in **Appendix A.5**.

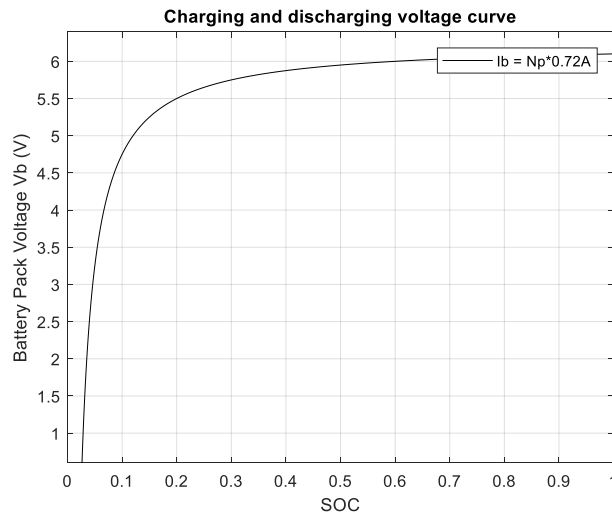


Fig. 2.28. Voltage curve of the simulated battery pack function of SOC.

## 2.4 Bidirectional Buck-Boost Converter

The battery energy storage (BES) is connected to the common DC bus through a bidirectional DC-DC converter [4]. This interfacing converter is an important part of power storage system, since he can charge and discharge the battery to balance the power between PV generation and load demand [7].

The bidirectional DC-DC converter can operate either as a Buck or as Boost converter. It works as a Buck converter for charging the battery, and it operates as a Boost for discharging the battery power to the load [9]. Using a bidirectional converter, the battery voltage can be chosen lower compared to reference DC-link voltage (12V), thus less batteries are needed to be connected in series [4].

Many bidirectional DC-DC converter topologies can be used. Basically, they are divided into two types, non-isolated and isolated converters. The non-isolated converters are much more attractive, because of the efficiency, size, weight and cost characteristics.

Among them, one of the widely used type is the Half-Bridge (HB) converter [65]. The HB bidirectional DC-DC converter is a combination of Buck and Boost converters where diodes have been replaced by controllable IGBT or MOSFET switches [66]. This converter is more attractive because of its reduced number of components, lower current stress and improved efficiency compared to other types such as SEPIC and Cuk converters [67]. Fig. 2.29 shows the Half-Bridge bidirectional DC-DC converter topology.

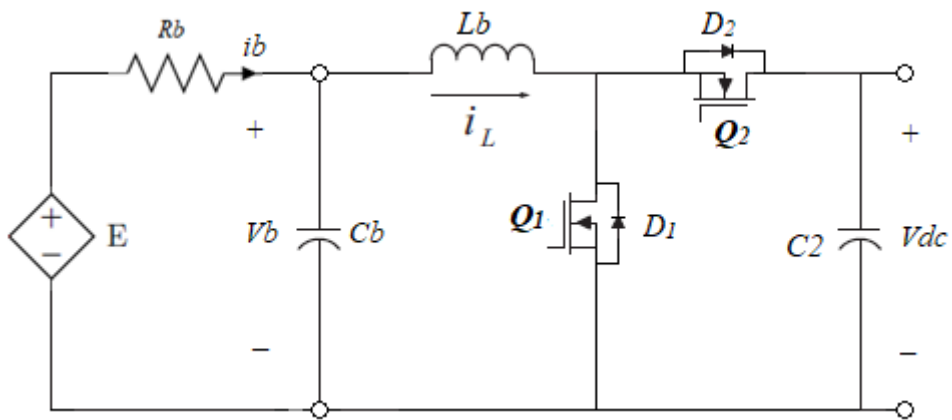


Fig. 2.29. Half-Bridge bidirectional DC-DC converter.

As can be seen from the proposed model, the battery pack is placed on the low voltage (LV) side  $V_b$ , while the high voltage (HV) side is connected to the DC bus  $V_{dc}$ . The inductor  $L_b$ , is on the LV side, decreasing the current ripple which is advantageous for charging and discharging the battery [68]. The two capacitors,  $C_b$  and  $C_2$ , are used to filter the ripple currents on both discharging and charging operations [65]. The switches  $Q_1$  and  $Q_2$  are controlled to permit the inductor current to flow on both directions and thus allowing the charging and discharging process.

#### 2.4.1 Converter Modeling

The bidirectional DC-DC converter is a combination of Buck and Boost converters. When  $Q_1$  is switched and  $Q_2$  is off, it works as Boost converter discharging the battery. Otherwise when  $Q_1$  is off and  $Q_2$  is modulated, it works as a Buck converter charging the battery. It should be noted that the two modes have opposite inductor current directions. Assuming that all the circuit elements are ideal, that the converter is designed to operate in CCM and defining a positive current during discharge mode, the state-space equations of the converter can be derived [69].

In **Boost** mode, the equivalent circuit for each switching state is represented in Fig. 2.30.

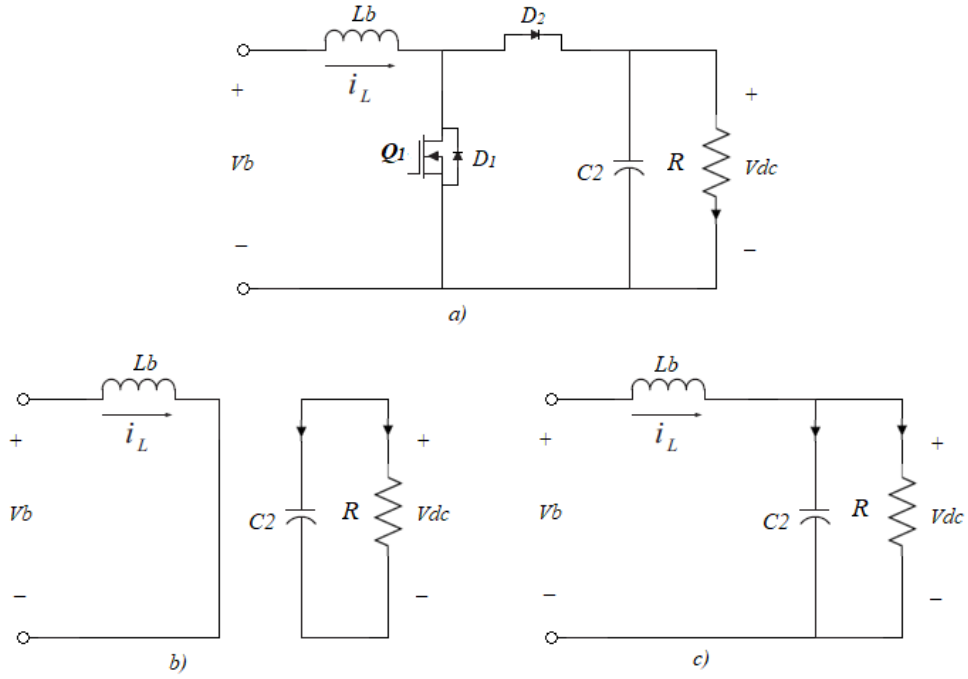


Fig. 2.30. a) Bidirectional Buck-Boost converter in Boost mode; b) switch Q1 is on; c) switch Q1 is off.

When switch Q1 is on, the differential equations of the state variables  $i_L$  and  $v_{dc}$ , are derived [70]:

$$L_b \frac{di_L}{dt} = v_b \quad (2.102)$$

$$C_2 \frac{dv_{dc}}{dt} = -\frac{v_{dc}}{R} \quad (2.103)$$

that expressed in state-space form:

$$\dot{\mathbf{x}} = \mathbf{A}_{on}\mathbf{x} + \mathbf{B}_{on}\mathbf{u}, \quad \mathbf{x} = \begin{bmatrix} i_L \\ v_{dc} \end{bmatrix}, \mathbf{u} = [v_b] \quad (2.104)$$

$$\begin{bmatrix} \dot{i}_L \\ \dot{v}_{dc} \end{bmatrix} = \begin{bmatrix} 0 & 0 \\ 0 & -\frac{1}{RC_2} \end{bmatrix} \begin{bmatrix} i_L \\ v_{dc} \end{bmatrix} + \begin{bmatrix} \frac{1}{L_b} \\ 0 \end{bmatrix} v_b \quad (2.105)$$

During the second interval, when the switch Q1 is off and diode D2 is activated, differential equations are:

$$L_b \frac{di_L}{dt} = v_b - v_{dc} \quad (2.106)$$

$$C_2 \frac{dv_{dc}}{dt} = i_L - \frac{v_{dc}}{R} \quad (2.107)$$

in state-space form become:

$$\dot{\mathbf{x}} = \mathbf{A}_{off}\mathbf{x} + \mathbf{B}_{off}\mathbf{u}, \quad \mathbf{x} = \begin{bmatrix} i_L \\ v_{dc} \end{bmatrix}, \mathbf{u} = [v_b] \quad (2.108)$$

$$\begin{bmatrix} \dot{i}_L \\ \dot{v}_{dc} \end{bmatrix} = \begin{bmatrix} 0 & -\frac{1}{L_b} \\ \frac{1}{C_b} & -\frac{1}{RC_b} \end{bmatrix} \begin{bmatrix} i_L \\ v_{dc} \end{bmatrix} + \begin{bmatrix} \frac{1}{L_b} \\ 0 \end{bmatrix} v_b \quad (2.109)$$

In **Buck** mode, when Q1 is off and Q2 switches on and off, the equivalent circuit for each switching state is represented in Fig. 2.31.

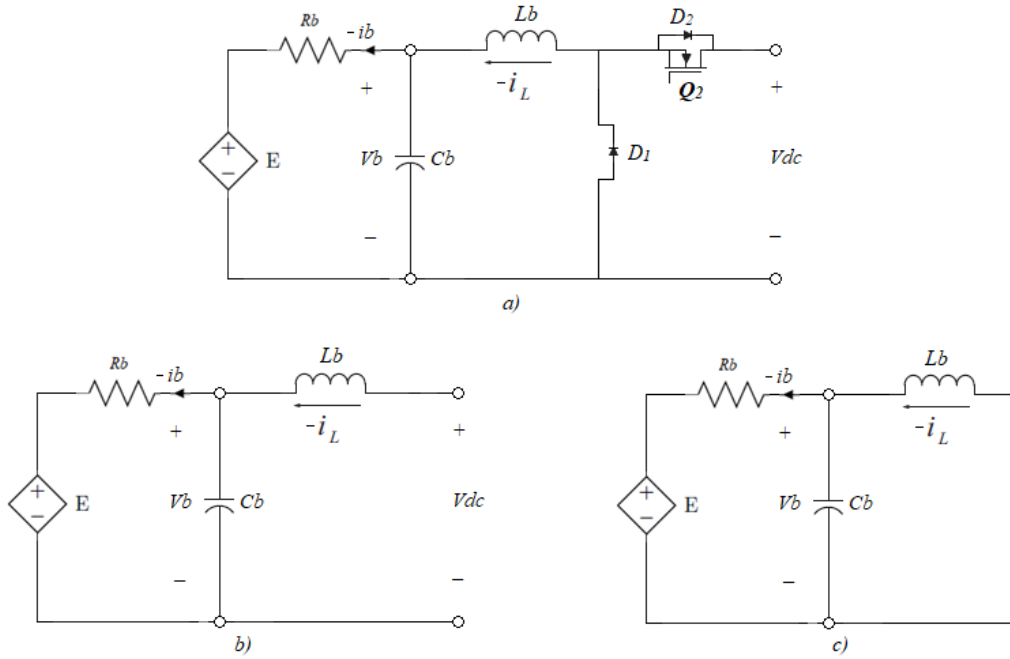


Fig. 2.31. a) Bidirectional Buck-Boost converter in Buck mode; b) switch Q2 is on; c) switch Q2 is off.

When switch Q2 is on, the differential equations of the state variables  $i_L$  and  $v_b$ , are:

$$L_b \frac{di_L}{dt} = v_b - v_{dc} \quad (2.110)$$

$$C_b \frac{dv_b}{dt} = -i_L - \frac{v_b - E}{R_b} \quad (2.111)$$

that given in state-space form are:

$$\dot{\mathbf{x}} = \mathbf{A}_{on}\mathbf{x} + \mathbf{B}_{on}\mathbf{u}, \quad \mathbf{x} = \begin{bmatrix} i_L \\ v_b \end{bmatrix}, \mathbf{u} = \begin{bmatrix} v_{dc} \\ E \end{bmatrix} \quad (2.112)$$

$$\begin{bmatrix} \dot{i}_L \\ \dot{v}_b \end{bmatrix} = \begin{bmatrix} 0 & \frac{1}{L_b} \\ -\frac{1}{C_b} & -\frac{1}{R_b C_b} \end{bmatrix} \begin{bmatrix} i_L \\ v_b \end{bmatrix} + \begin{bmatrix} -\frac{1}{L_b} & 0 \\ 0 & \frac{1}{R_b C_b} \end{bmatrix} \begin{bmatrix} v_{dc} \\ E \end{bmatrix} \quad (2.113)$$

During the second interval, when the switch Q2 is off and diode D1 becomes forward biased (on), differential equations are:

$$L_b \frac{di_L}{dt} = vb \quad (2.114)$$

$$C_b \frac{dvb}{dt} = -i_L - \frac{vb - E}{R_b} \quad (2.115)$$

Written in state-space form become:

$$\dot{\mathbf{x}} = \mathbf{A}_{off}\mathbf{x} + \mathbf{B}_{off}\mathbf{u}, \quad \mathbf{x} = \begin{bmatrix} i_L \\ vb \end{bmatrix}, \mathbf{u} = \begin{bmatrix} v_{dc} \\ E \end{bmatrix} \quad (2.116)$$

$$\begin{bmatrix} \dot{i}_L \\ \dot{vb} \end{bmatrix} = \begin{bmatrix} 0 & \frac{1}{L_b} \\ -\frac{1}{C_b} & -\frac{1}{R_b C_b} \end{bmatrix} \begin{bmatrix} i_L \\ vb \end{bmatrix} + \begin{bmatrix} 0 & 0 \\ 0 & \frac{1}{R_b C_b} \end{bmatrix} \begin{bmatrix} v_{dc} \\ E \end{bmatrix} \quad (2.117)$$

#### 2.4.2 Complementary Analysis

From the above analysis, it can be noticed that irrespective of the mode of operations, Buck or Boost, the switches Q1 and Q2 are complementary to each other. Therefore, combining the two mode of operations, and defining  $i_L$  in Boost mode as a positive current, a common model can be developed with only two states [71]. The two subintervals are denoted as: discharging mode (Q1 on and Q2 off) and charging mode (Q1 off, Q2 on), and are shown in Fig. 2.32 [72].

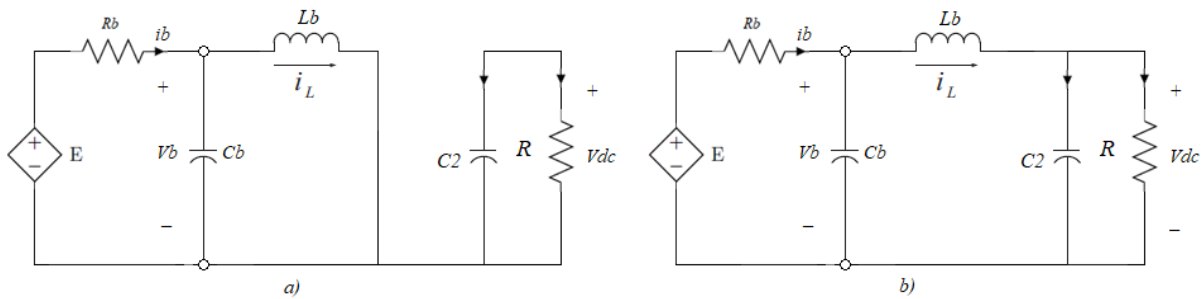


Fig. 2.32. Bidirectional converter common model with two subintervals: a) Discharging mode (Q1 on, Q2 off); b) Charging mode (Q1 off, Q2 on).

During the discharging mode, when the switch Q1 is on and Q2 off, the differential equations of the state variables  $i_L$ ,  $vb$  and  $v_{dc}$ , are derived as follow:

$$L_b \frac{di_L}{dt} = vb \quad (2.118)$$

$$C_b \frac{dvb}{dt} = -i_L - \frac{vb - E}{R_b} \quad (2.119)$$

$$C_2 \frac{dv_{dc}}{dt} = -\frac{v_{dc}}{R} \quad (2.120)$$

In the second subinterval (charging mode), when Q2 is on while Q1 is off, the state equations are:

$$L_b \frac{di_L}{dt} = vb - v_{dc} \quad (2.121)$$

$$C_b \frac{dvb}{dt} = -i_L - \frac{vb - E}{R_b} \quad (2.122)$$

$$C_2 \frac{dv_{dc}}{dt} = i_L - \frac{v_{dc}}{R} \quad (2.123)$$

Finally, the converter dynamic behavior can be described considering the states of the switches. The continuous-time model of the converter, which assembles charging and discharging modes, can be derived [73]:

$$\frac{di_L}{dt} = \frac{vb}{L_b} - (1-s) \frac{v_{dc}}{L_b} \quad (2.124)$$

$$\frac{dvb}{dt} = -\frac{i_L}{C_b} - \frac{vb - E}{R_b C_b} \quad (2.125)$$

$$\frac{dv_{dc}}{dt} = (1-s) \frac{i_L}{C_2} - \frac{v_{dc}}{RC_2} \quad (2.126)$$

where  $s$  represents the state of the switches

$$s = \begin{cases} 1 & \text{Q1 on, Q2 off} \\ 0 & \text{Q1 off, Q2 on} \end{cases} \quad (2.127)$$

and written in state-space form become:

$$\begin{bmatrix} \dot{i}_L \\ \dot{vb} \\ \dot{v}_{dc} \end{bmatrix} = \begin{bmatrix} 0 & \frac{1}{L_b} & -\frac{(1-s)}{L_b} \\ -\frac{1}{C_b} & -\frac{1}{R_b C_b} & 0 \\ \frac{(1-s)}{C_2} & 0 & -\frac{1}{RC_2} \end{bmatrix} \begin{bmatrix} i_L \\ vb \\ v_{dc} \end{bmatrix} + \begin{bmatrix} 0 \\ \frac{1}{R_b C_b} \\ 0 \end{bmatrix} E \quad (2.128)$$

### 2.4.3 Converter Design

As for the non-inverting Buck-Boost converter, the system is designed such that the converter is operated in CCM. The design of the converter is same as the Buck design and Boost design, since these are the two modes of operation of the converter. Bidirectional specification and design parameters are shown in Table 9.

**Table 9.** Bidirectional specification and design parameters.

Deign parameters	Target values
Battey voltage, $V_{in}$	6 V

DC bus voltage, $V_{dc}$	12 V
Output power, $P_o$	8 – 80 W
Switching frequency, $f_s$	20 kHz
Bus voltage ripple, $\Delta V_{dc}$	120 mV (1% of $V_{dc}$ )
Battery voltage ripple, $\Delta V_b/V_b$	1%

The inductance value to ensure the converter operates in CCM, for both Buck and Boost modes, is calculated as follow [40]:

$$L_{min_b} = \frac{D(1-D)^2 V_{dc}^2}{2P_{o_{min}} f_s} = \frac{\frac{1}{3} \left(1 - \frac{1}{3}\right)^2 12^2}{2 * 8 * 20 * 10^3} = 0.07mH * 1.25 = 0.9mH \quad (2.129)$$

Where  $D$  is substituted with  $1/3$ , that corresponds to the maximum value solution of Eq. (2.129), as already observed in section 2.2.5. Furthermore, to ensure that the converter maintains operations under CCM, the inductance was multiplied by 1.25.

Considering the voltage ripple required by the converter, the capacitors were selected. The bus capacitor was designed as:

$$C_{dc} = \frac{DP_{o_{min}}}{f_s \Delta V_{dc} V_{dc}} = \frac{0.5 * 8}{20 * 10^3 * 0.120 * 12} = 139\mu F * 1.25 \approx 175\mu F \quad (2.130)$$

The size of the battery capacitor value can be determined as:

$$C_b = \frac{(1-D)}{8f_s^2 L_{min} \left(\frac{\Delta V_b}{V_b}\right)} = \frac{(1-0.5)}{8 * 20^2 * 10^6 * 0.9 * 10^{-3} * 0.01} \approx 20\mu F \quad (2.131)$$

For the simulation slightly higher values of inductance and capacitances were chosen.  $L_b = 0.6mH$   
 $C_{dc} = 800\mu F$  and  $C_b = 700\mu F$ .

## 2.5 DC Load Analysis

The PV stand-alone system and all the components considered in the previous sections, were designed considering a DC load. The DC load can be modelled as resistance  $R_{load}$ , which is determined by the power and voltage at the DC bus. The electrical appliances considered, and the evaluating energy demand of the off-grid solar system are shown in table 10.

**Table 10.** Load profile of the appliances.

Appliance	Quantity	Nominal Power (W)	Hours per day	Wh/d
Light LED	2	10	6	120
Universal battery charger	1	8	6	48
Total Wh per day				168

The daily load profile was determined by calculating the energy demand (Wh/day) for all estimated load types [74]. The energy consumption of the load is fundamental to design the rated power of the PV array.

---

In PV system design process, the location of the system should be considered to determine the availability of solar radiation [75]. As an example, its assumed that the system is in a rural area of the central India. The solar irradiances and the peak sun hours in this area, for typical winter and summer weeks of the year, can be easily found in insolation maps on the internet. As a common practice the design is carried out based on the worst month. The worst-case scenario of an area located in the central India is in the summer month of July, and a value of 3.5h was considered as the peak sun hours. Considering an overall system efficiency of about 75%, because of the different system inefficiencies like soiling, voltage drop, degrading of the PV module, battery losses, converter losses, etc., the PV system capacity results in:

$$PV \text{ capacity } (W) = \frac{\text{Daily energy use } \left(\frac{Wh}{d}\right)}{\text{peak sun hours } (h) * \text{efficiency}} = \frac{168 \frac{Wh}{d}}{3.5h * 0.75} \approx 65W$$

This outcome assumes optimal azimuth, tilt angle and no shading. The calculated value represents the minimum power array needed. Usually, PV system are oversized to avoid power interruptions, and a compromise must be done between oversizing the system to guarantee more power and reducing costs [75]. Therefore, an **80W** SolareX panel, as in section 2.1, was selected to represent the solar system.

## Chapter 3. Control System Design

In this chapter the control design of the system under study is discussed. All the block components of the off-grid system and the two main control units are represented in Fig. 3.

In the first control unit the maximum power point tracking (MPPT) technique is used to extract the maximum power from the PV array, and a Proportional-integral (PI) controller is required in order to solve converter's stability problems. In practice, the MPPT algorithm provides the reference voltage  $V_{ref}$ , and then the inner control loop makes the interfacing voltage to track its reference value.

The other control unit, that is the core of the thesis is the model predictive control (MPC). The objective of the proposed strategy is to control the Bidirectional converter in order to balance the power between PV generation and load demand, and moreover, to regulate the DC bus voltage and to improve battery life implementing constrains on the SOC of the battery to avoid overcharge and over discharge.

An accurate analysis with the corresponding simulation results is presented in this chapter.

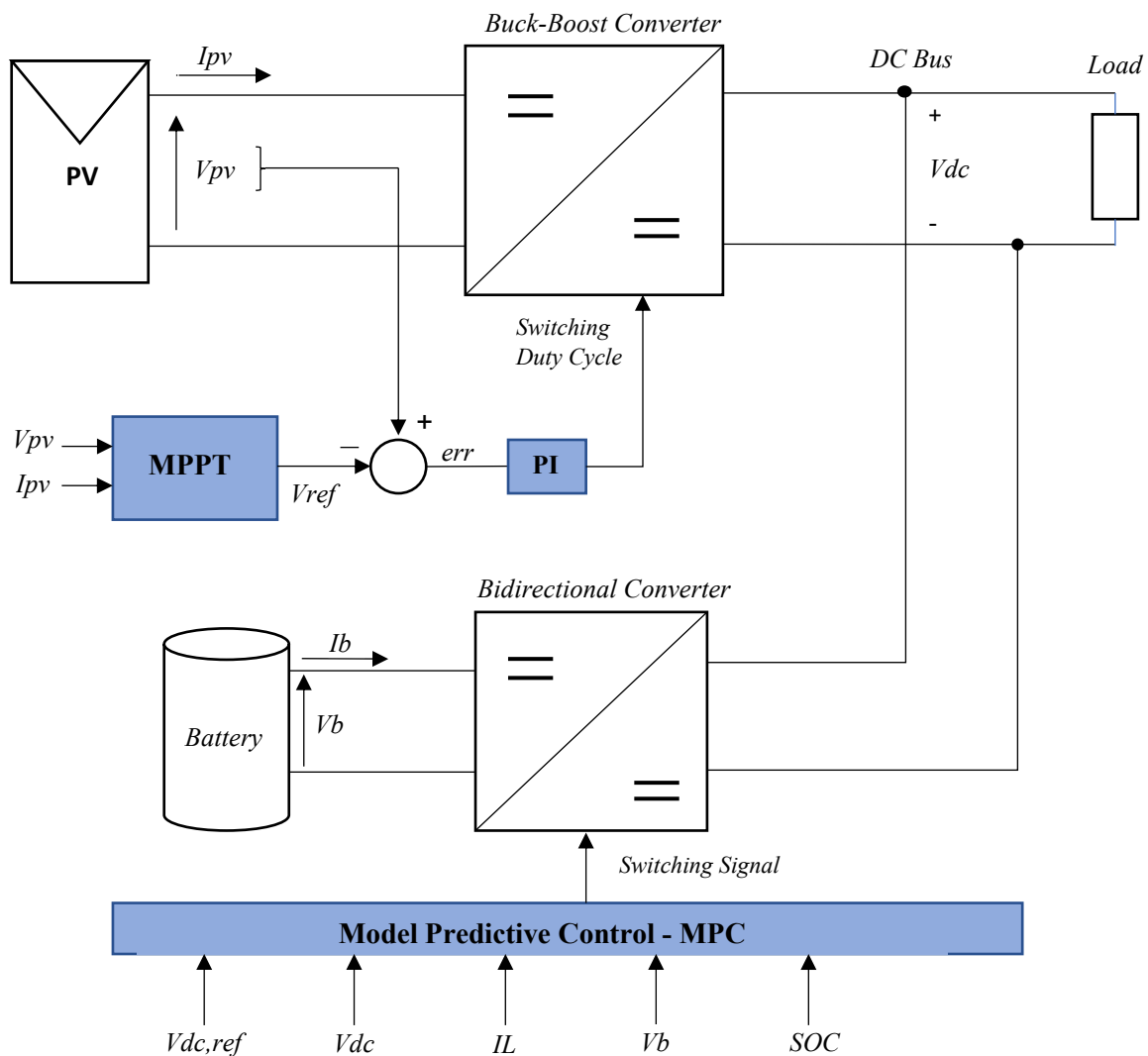


Fig. 3. Block diagram of the control units.

### 3.1 Maximum Power Point Tracking

As seen in section 2.1, the PV array characteristics ( $P$ - $V$  and  $I$ - $V$ ) present a maximum power point (MPP) for a certain operating voltage ( $V_{mp}$ ) and current ( $I_{mp}$ ). This is the point the panel should operate in order to deliver the maximum available power [9]. This MPP varies at every instance due to weather conditions, therefore, to achieve an efficient PV power generation system an MPPT technique is necessary. MPPT algorithms are usually employed on interfacing DC-DC power converters, to hold the operation point at the MPP by regulating either the current or voltage of the MPPT converter [8]. The voltage control is preferred because the voltage at the MPP is almost constant. On the other hand, the PV current, changes greatly with variations in solar irradiation [12]. Hence, regulating the PV voltage should improve the performance of the MPPT.

Different MPPT algorithms can be used, and many theoretical improvements have been proposed in the literature to enhance the performance of the methods. Among all the algorithms, Fractional Open Circuit Voltage (FOCV), Fractional Short Circuit Current (FSCC), Perturb and Observe (P&O) and Incremental Conductance (Inc) are few of them that can be easily implemented and are state-of-the-art techniques [12]. In the thesis the well-known P&O algorithm has been used to track the MPP of the solar module.

#### 3.1.1 P&O Algorithm

Perturb and Observer (P&O) is the most commonly used algorithm because is simple and easy to implement while maintaining relatively good performance.

As the name says, the P&O algorithm tracks the MPP by iteratively perturbing the PV voltage  $V_{pv}$ , observing and comparing the power generated by the panel  $P_{pv}(k)$  at any instant with the previous power  $P_{pv}(k-1)$  [20].

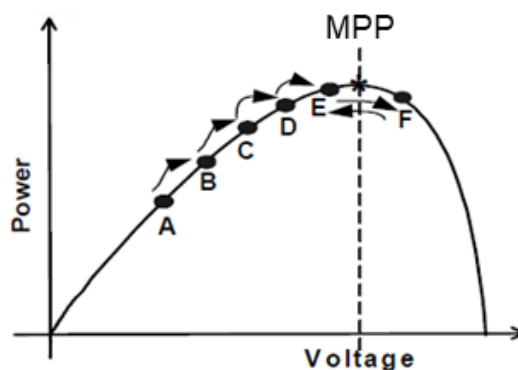


Fig. 3.1.  $P$ - $V$  curve of a PV module and P&O illustration concept.

A general  $P$ - $V$  curve that helps to understand the concept is plotted in Fig. 3.1 [76]. From the figure in can be seen that decreasing voltage on the right side of the MPP increases power and increasing voltage on the left side of the MPP also increases power. For example, after an increment in the PV operating voltage, the algorithm compares the actual measured power with the previous one. If the power has increased, it keeps the same direction (increasing voltage), otherwise it changes direction (decreasing voltage). The process is repeated at every MPPT step until the MPP is reached [77].

However, P&O method cannot converge to the correct MPP, indeed it oscillates around the MPP in steady state [78]. The deviation depends on the size of the step used to perturb the voltage. With a small size of the step, the oscillations are reduced, but the tracking will be slower, while with bigger step size the tracking is faster, but the oscillations will be bigger. Therefore, in order to improve both

tracking speed and algorithm accuracy a compromise must be done in the selection of the perturbation step size [7].

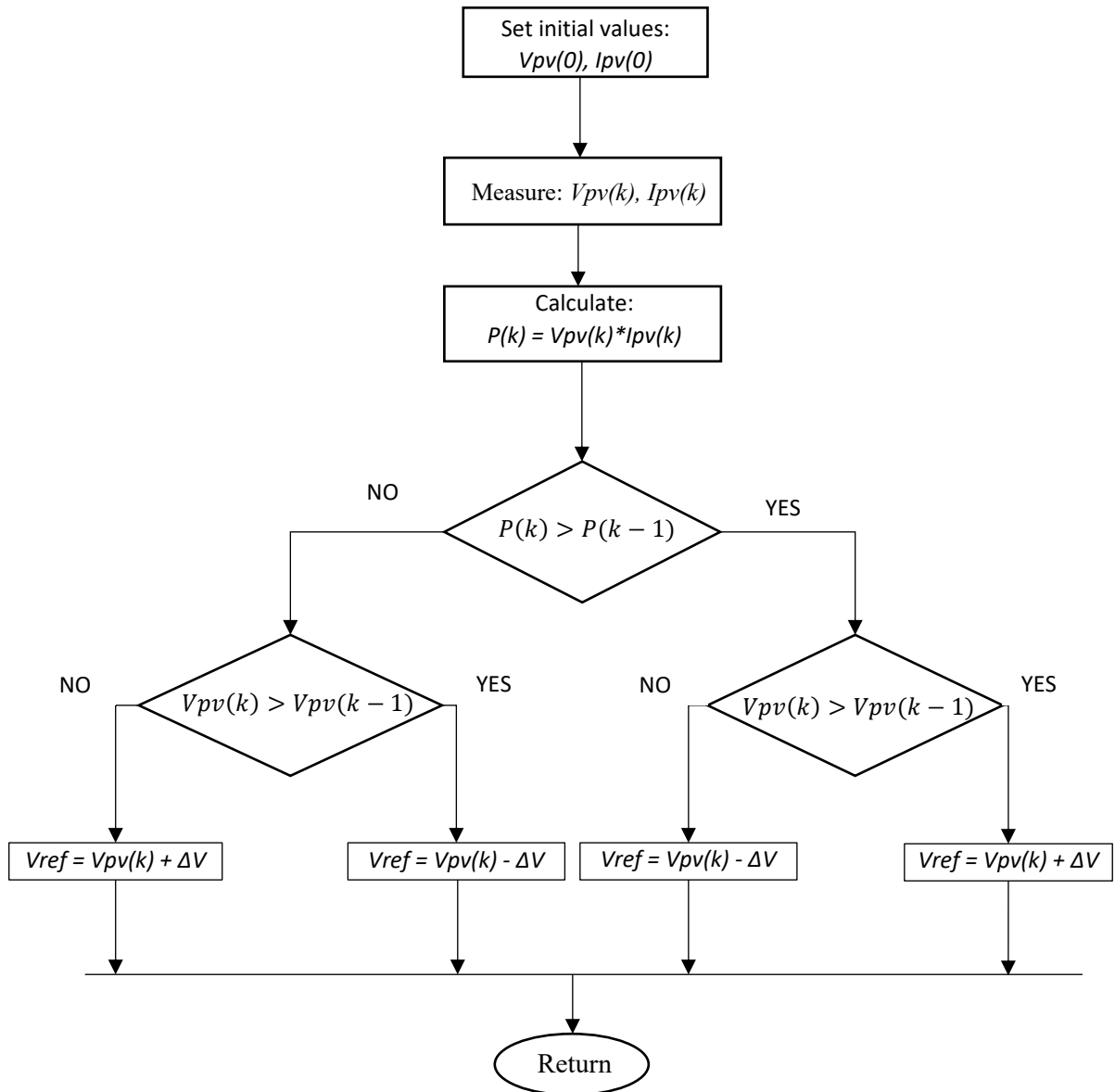


Fig. 3.2. Flowchart of the P&O algorithm with voltage perturbation.

The flowchart of the P&O algorithm with voltage perturbation is shown in Fig. 3.2. The P&O algorithm is implemented in MATLAB (file script in **Appendix B.1**) together with the PV array model, to validate the chosen MPPT technique. The results of the P&O tracking method with a constant step size compromised at a value of  $\Delta V = 0.25$  are plotted in Fig. 3.3.

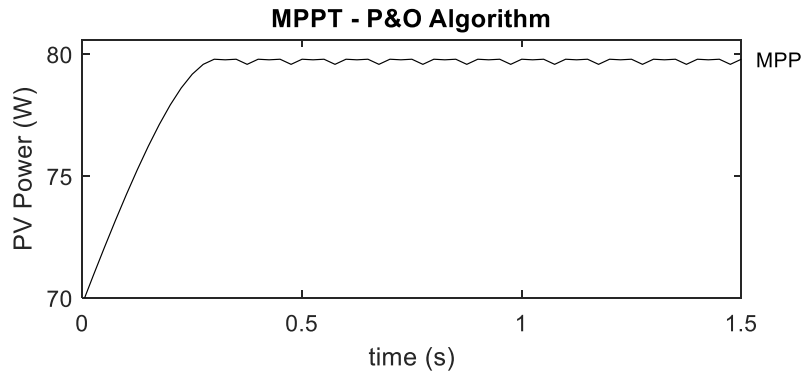


Fig. 3.3. Performance of P&O algorithm with voltage step size  $\Delta V = 0.25$ .

Based on the graph, the expected maximum power is 79.8 W, which corresponds at the parameter  $P_{mp}$ , given in the PV array datasheet (see Table 2). Thus, the MPPT MATLAB code is validated.

### 3.2 MPPT Converter Control

Converters with the MPPT algorithm are used to continuously detect the maximum instantaneous power of the PV array. However, the achievement of MPPT strongly depends on the performance of the converter and its ability to regulate the operating point of the PV panel [12].

Depending on the topology of the system, current, voltage or duty cycle can be controlled. The direct duty cycle control is not recommended because the converter is subject to increased switching stress and losses, and a feedback control for the converter voltage or current is preferred [15]. In [8] is observed that input voltage is recommended to be used since the input current control is prone to saturation of the controller. Therefore, to achieve a reliable operation of the MPPT, a feedback control loop is needed and Proportional-Integral (PI) control is commonly applied to regulate converter's stability problems. As shown in the control scheme of Fig. 3.4, the MPPT algorithm provides the reference voltage  $V_{ref}$ , for the converter and the PI controller uses this reference to impose the duty cycle to the converter to regulate the voltage to the desired value [79]. In short, the inner control loop makes the interfacing voltage  $V_{pv}$ , to track its reference value  $V_{ref}$ .

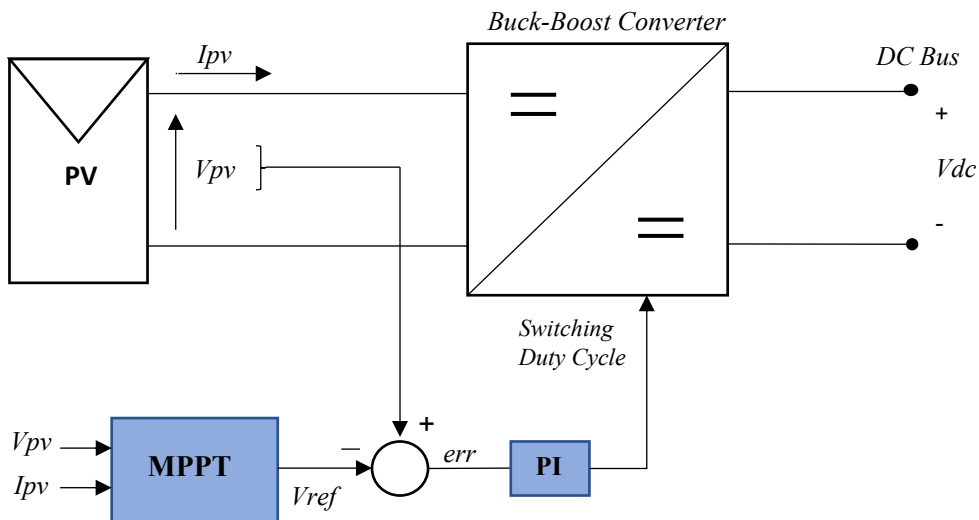


Fig. 3.4. MPPT converter control scheme.

The dynamic behavior of the converter is essential for the design of an effective PI controller. Small-signal analysis and Bode Plot representation were used to design the proposed control strategy.

### 3.2.1 Open Loop Analysis

In order to develop the control loop of the non-inverting Buck-Boost converter under study, the converter model linearized at a chosen operating point is necessary. The linear model was obtained by applying the small-signal analysis with the purpose to find small-signal transfer functions that describe the dynamic behavior of the converter input voltage near the operating point and can be used in the design of the closed loop control system [13].

The control to input voltage transfer functions of the non-inverting Buck-Boost converter working in Buck and Boost modes respectively, as previously calculated in paragraph 2.2.4 (equations 2.46 and 2.68) are re-proposed.

$$Gv_{buck}(s) = \frac{\widehat{vpv}}{\widehat{d}'} = \frac{\frac{V_{C_2}}{RC_1} \left[ s^2 + \left( \frac{R}{L} + \frac{1}{RC_2} \right) s + \frac{2}{LC_2} \right]}{s^3 + \frac{1}{RC_2} s^2 + \left( \frac{1}{LC_2} + \frac{D^2}{LC_1} \right) s + \frac{D^2}{RLC_1C_2}} \quad (3.1)$$

$$Gv_{boost}(s) = \frac{\widehat{vpv}}{\widehat{d}'} = \frac{\frac{V_{C_2}}{LC_1} \left( s + \frac{2}{RC_2} \right)}{s^3 + \frac{1}{RC_2} s^2 + \left( \frac{1-D}{LC_2} + \frac{1}{LC_1} \right) s + \frac{1}{RLC_1C_2}} \quad (3.2)$$

Where the complement of the small signal duty cycle  $\widehat{d}'$  is chosen as the control variable, since positive variations of duty cycle  $d$  produce negative variations of input voltage  $vpv$ , as already said.

The two transfer functions  $Gv_{buck}$  and  $Gv_{boost}$ , describe the converter response of the input voltage to small variations  $\widehat{d}'$  around the operating point  $V_{pv} = \frac{R \cdot I_{pv}}{D}$ , in Buck mode and  $V_{pv} = (1 - D)^2 R \cdot I_{pv}$ , in Boost mode operation [79].

Before design the controller, the dynamic characteristic of the open loop system is analyzed. The frequency domain responses of the Buck and Boost modes converter are plotted in Figs. 3.5 – 3.6.

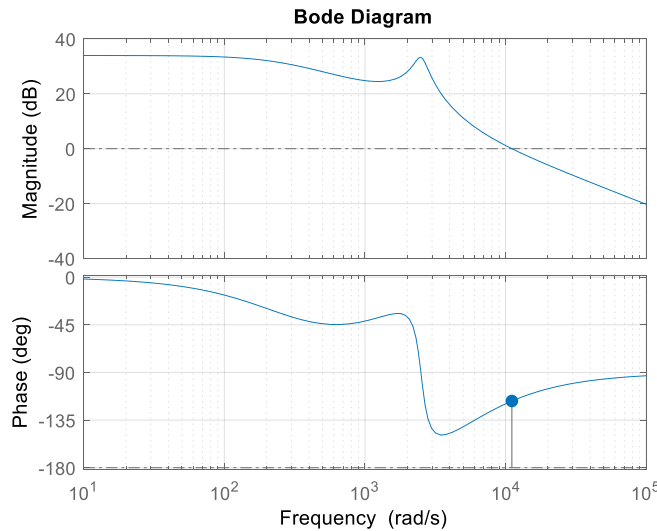


Fig. 3.5. Frequency response of small-signal Buck transfer function  $Gv_{buck}$ .

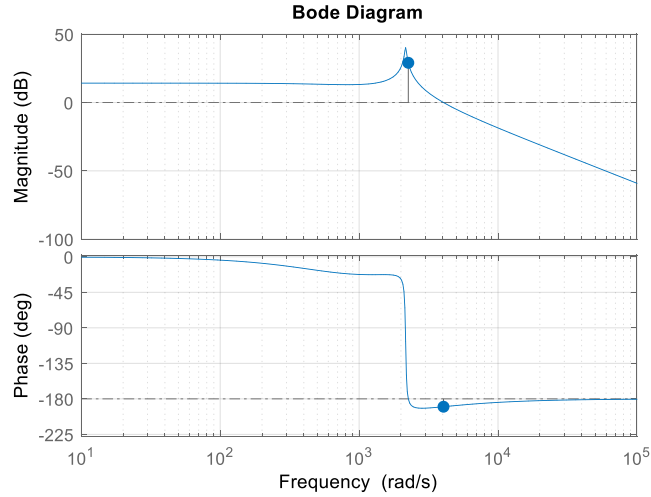


Fig. 3.6. Frequency response of small-signal Boost transfer function  $Gv_{boost}$ .

The magnitude and phase plots are obtained based on MPP operating condition. Parameters in Table 11.

**Table 11.** Parameters at MPP operating condition.

Parameters	Values
$I_{pv}$	4.75 A
$L$	0.33 mH
$C1$	700 $\mu$ F
$C2$	700 $\mu$ F
$R$	1.8 $\Omega$
$D$	0.7

According to Bode diagrams, in Buck mode the open loop system is stable and has a good phase margin, however in Boost mode the system indicates negative gain and phase margin which make the converter completely unstable [28]. Therefore, a proper controller needs to be designed for stabilizing the system.

The controller is designed for the optimal performance of Boost mode and it will automatically fit for Buck operation mode, thus it is used to control both Buck and Boost modes. However, this approach will reduce performance in Buck mode because it limits the selection of high crossover frequency.

Provide a smooth transition from the two operation modes is a big issue in controlling a non-inverting Buck-Boost converter. Accordingly to [28], using different controllers to each operation mode will increase the input voltage performance but it will lead to instability during the transition from one mode to the other.

### 3.2.2 PI Controller Design

To solve stability issues and improve system response a PI controller is designed. A classic PI controller can be represented by the following equation.

$$\hat{d}'(t) = Kp * e(t) + Ki * \int_0^T e(t)d(t) \quad (3.3)$$

Where  $\hat{d}'$ , is the controller output,  $e(t)$  is the error signal generated from the difference between the reference and the converter input voltage,  $Kp$  and  $Ki$  are the proportional and integral gains, respectively. The proportional compensator is used to increase the bandwidth of the system, allowing faster transient response and the integral compensator is used to remove the steady state error [79].

Many conventional control design methods can be used to get the parameters of the controller, such as the Ziegler-Nichols (Z-N) method, Root Locus (RL) method, etc. In this study Bode Plot design was applied using MATLAB Control System Designer Toolbox, a popular method for control engineers. Bode Plot design using Control System Designer is an interactive graphical method of tuning a controller to achieve a specific closed loop response.

In the Bode Editor, it's possible to adjust the open loop bandwidth and design the gain and phase margin to reach the desired specifications and to modify characteristics such as settling time and overshoot.

A small glance to the operation of the Control System Designer Toolbox is shown in Fig. 3.7.

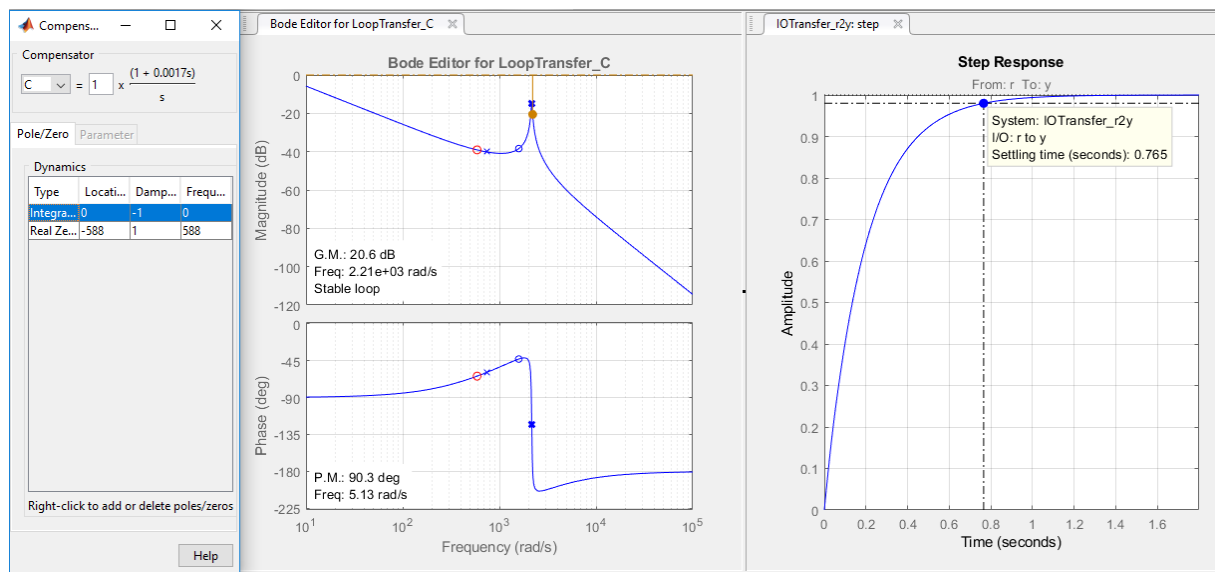


Fig. 3.7. Control System Designer: (left) controller parameters; (center) Bode plot of the open loop transfer function; (right) step response of the overall closed loop system (controller and plant).

The parameters of the controller can be directly derived from the Compensator Editor (in the left of Fig. 3.7) and the controller transfer function in  $s$ -domain can be written,

$$C_i(s) = Kp + \frac{Ki}{s} = \frac{(1 + 0.0017s)}{s} \quad (3.4)$$

whit  $Kp = 0.0017$  and  $Ki = 1$ .

The frequency responses of the open loop converter uncompensated and compensated are shown in Fig. 3.8.

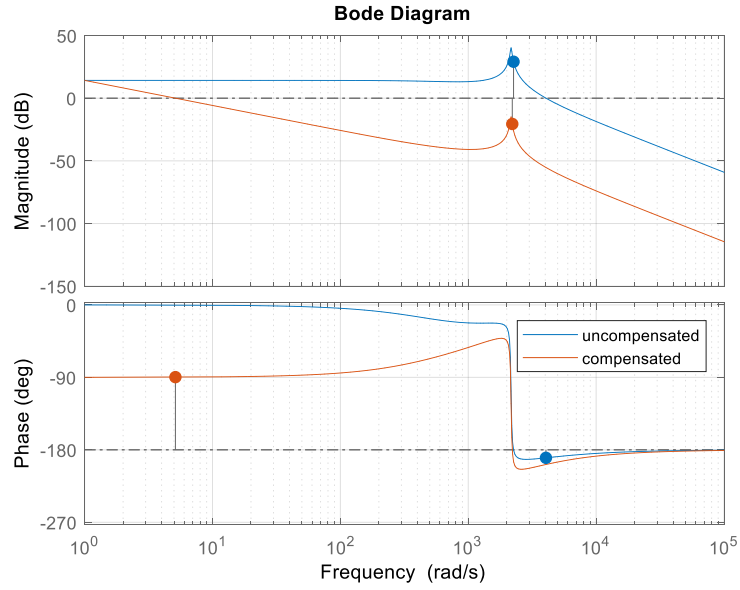


Fig. 3.8. Frequency responses of uncompensated and compensated open loop system.

As shown, with these settings the requirement of system stability is fulfilled. However, the small bandwidth results in fragile overall stability and can produce oscillations in the resulting output variables of the system.

### 3.2.3 Closed Loop Analysis

The block diagram of the closed loop control system used to control the input voltage of the converter is built in Fig. 3.9.

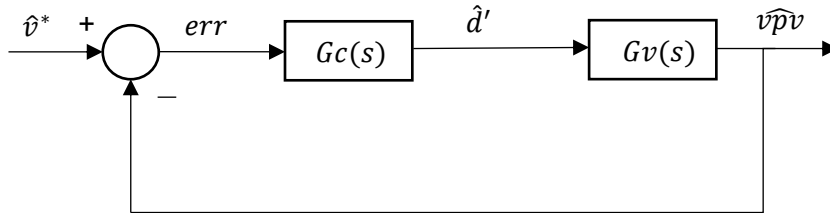


Fig. 3.9. Closed loop block diagram of the linearized model.

Where  $G_c(s)$  is the PI controller transfer function,  $G_v(s)$  is the converter linearized transfer function and  $\hat{v}^*$  represent the small-signal reference value.

Worth to notice is that, as the input of the system is the control variable  $\hat{d}'$  (ac variations of the complement of the duty cycle), there is no need to use positive feedback and reverse the sign of the reference signal as stated in paragraph 2.2.4, because the application of positive feedback control equals dynamically to the inversion of the switch control signal [20]. An easy demonstration of this statement using control properties is solved in **Appendix B.2**.

The closed loop transfer function of the block diagram in the negative feedback loop is calculated as:

$$G(s) = \frac{G_c * G_v}{1 + G_c * G_v} \quad (3.5)$$

The step response of the closed loop system  $G(s)$  is shown in Fig. 3.10.

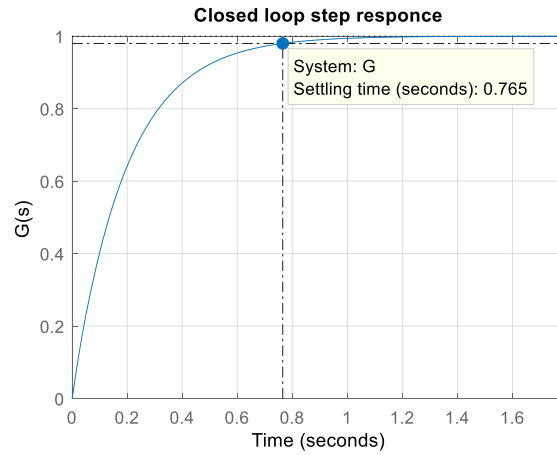


Fig. 3.10. Step response of the closed loop system.

As can be seen, with the PI controller designed in the previous section, the closed loop system of the converter connected to the PV array reach zero steady state error, has a small settling time and good stability (assured by the big phase margin value of the compensated open loop system) [79].

The MATLAB script file used to obtain the Bode Plots of the converter, the step response of the closed loop system and the design of the PI controller is reported in **Appendix B.3**.

### 3.2.4. Implementation and Simulation Results

Because both PV array and switching mode converter have nonlinear and time variant characteristics, a control strategy was needed, as discussed in the previous sections, and the small-signal analysis was performed to design the PI controller.

Now the implementation of the control unit in the PV-MPPT-Converter system, represented in Fig. 3.11, is analyzed.

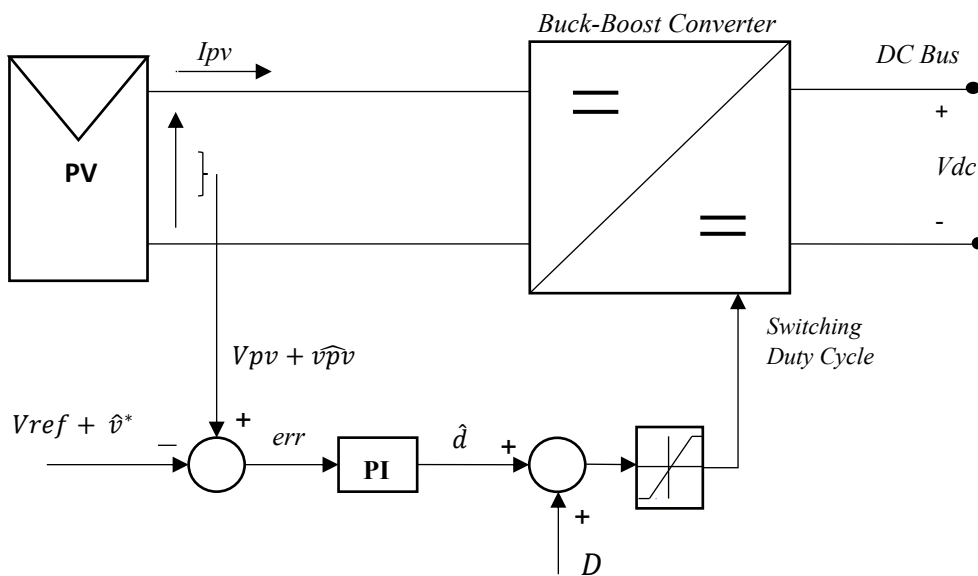


Fig. 3.11. Configuration of the overall system, which emphasizes the large-signal and small-signal values.

The figure above shows the PV module, the DC-DC converter and the control loop, with an emphasis in the large-signal and small-signal structure of the parameters. The output voltage of the MPPT algorithm represent the reference of the control loop and can be written as sum of the large-signal and small-signal values,  $V_{ref} + \hat{v}^*$ , but because this voltage reference meant to be tracked is constant, we want the small-signal value to be zero so it is negligible. The reference value is then compared to the input voltage of the converter and the error is sent to the PI controller.

To notice is that positive feedback is used, since the small signal duty cycle  $\hat{d}$  (and not  $\hat{d}'$ ) is implemented. The ac variation of the complement of the duty cycle  $\hat{d}' = -\hat{d}$ , was more convenient to use for obtaining the small-signal transfer function.

Therefore, the PI controller performs the adjustment to the error signal to obtain the small-signal control variable  $\hat{d}$ , which is summed up to the large-signal duty ratio  $D$  and so, after passing through a limiter block, the switching duty cycle signal controlling the converter is obtained. For a digital control, logic unit is used to decide the switching modes.

The control unit was implemented in MATLAB command line. The control algorithm, reported in **Appendix B.4**, includes the PV model, the non-inverting Buck-Boost converter, the MPP tracking algorithm and the input voltage control loop.

The simulation time step of the implemented system is  $1\mu\text{s}$  and the switching frequency of the converter is 20kHz (switching period  $50\mu\text{s}$ ). The control frequency, that need to be lower than the switching frequency, is 1kHz (control loop sampling period 1ms). The control loop frequency should be significantly faster than the MPPT update rate. This is important because after MPPT updates the value, the control loop must have enough steps to be able to steer the input voltage to the new value. In the implementation, the MPPT algorithm runs at 40Hz (25ms) which is 25 times slower than the control frequency (1kHz) [77]. The simulation parameters are reported in Table 12.

**Table 12.** Simulation Parameters.

<b>Parameters</b>	<b>Values</b>
<i>Simulation time step</i>	$1\mu\text{s}$
<i>Switching frequency</i>	20kHz (50 $\mu\text{s}$ )
<i>Control update rate</i>	1kHz (1ms)
<i>MPPT update rate</i>	40Hz (25ms)

Another important parameter to consider is the value of the input capacitor. It contributes to the accuracy of the MPPT. Input capacitance can limit current ripple, but it also slows down input voltage variations. Too small value can cause high voltage ripple, but a too big capacitance will cause the control loop to be unable to reach the MPPT set point.

The continuous-time controller designed in previous sections is implemented as discrete-time digital controller and an integrator anti-windup block was also added in the control unit with an important function. This algorithm stops the integrator when the control output exceeds the limits, because sometimes the controller output may exceed the maximum effective control effort, causing integrator saturation and deteriorating the control performance [12].

Finally, the MATLAB code of the system is tasted. The simulation results are plotted in Fig. 3.12.

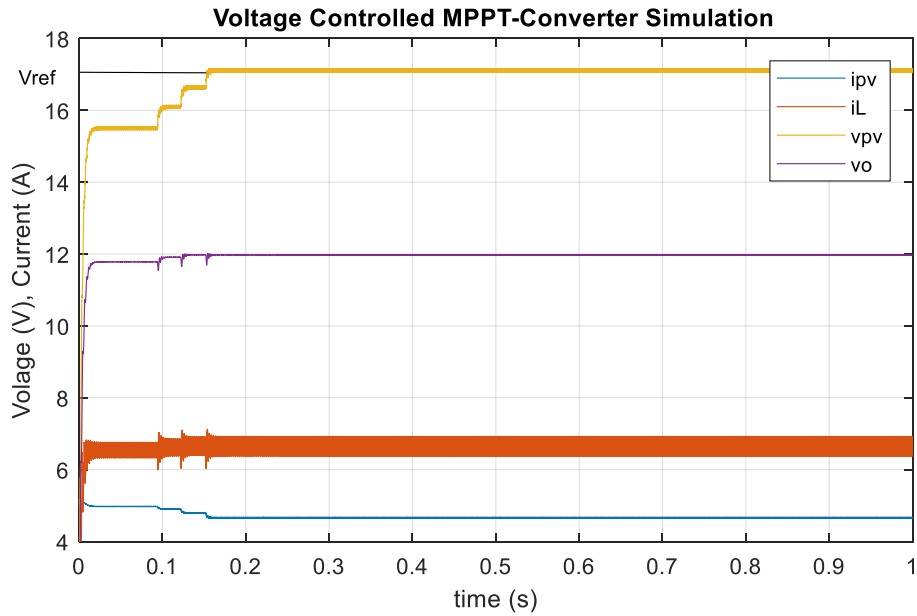


Fig. 3.12. PV system with the MPPT&PI control unit simulation results.

The state and the input variables of the converter, inductance current  $i_L$ , input voltage  $v_{pv}$ , output voltage  $v_o$ , and input current  $i_{pv}$ , are displayed.

From these results, it can be seen that the input voltage  $v_{pv}$ , tracks the reference voltage  $v_{ref}$ , calculated by the MPPT.

The input voltage reached is around 17V, that corresponds at the voltage at the MPP that is 16.8V (at STC). The maximum power at this point should be around 79.8 W, and this is confirmed in Fig. 3.13 where the power extracted from the PV during the MPP tracking control is plotted.

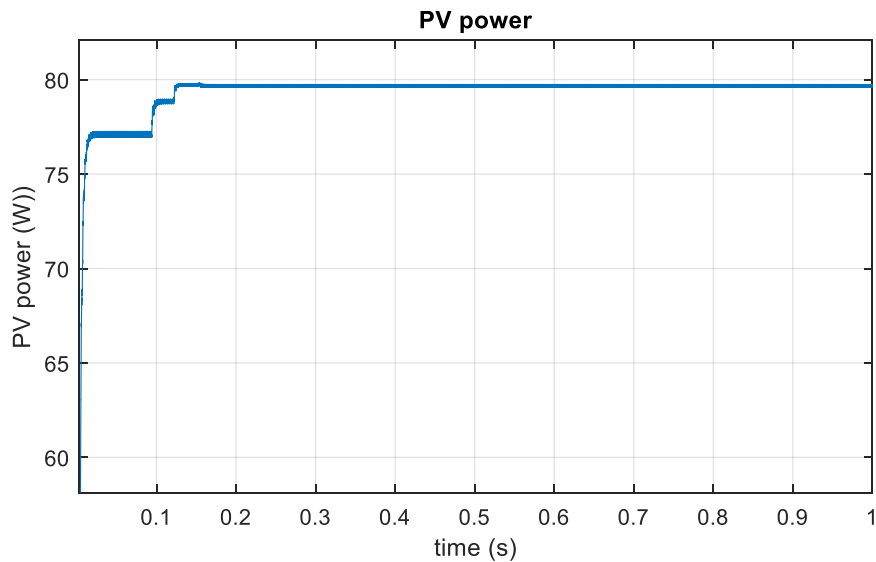


Fig. 3.13. PV power tracking.

Unfortunately, from Fig. 3.12 it can also be seen that some perturbations appear, mostly at the beginning of the trajectory. To try to have an accurate understanding of the reasons why these perturbations occur, other parameters are extracted from the simulations and plotted in Fig. 3.14.

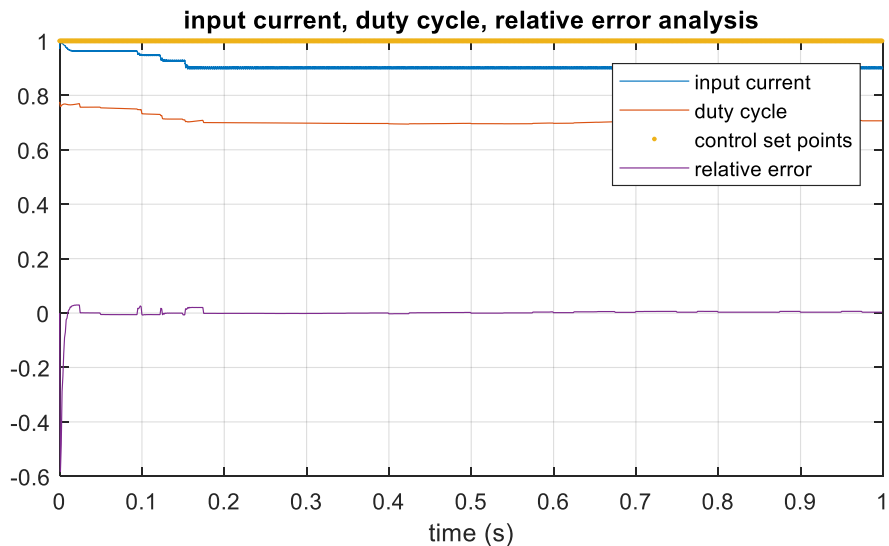


Fig. 3.14. Input current, duty cycle and relative error analysis diagram.

In the figure, yellow points represent the points at which the control is executed. The figure also shows the change in input current, duty cycle and relative error. This last parameter underlines that a zero steady state error is achieved.

Because the model of the converter including switching ripple is considered, in the time domain simulation oscillations can occur if the control strategy is not well adapted to the dynamic behavior of the system. Obviously, averaged model tracks better than switching model but it does not represent the 'real life' of the system, thus it is meaningless.

In the model studied, these perturbations are mostly due to the fact that the frequency response of the system has limitations in bandwidth, resulting in a cross-over frequency that is much smaller than the switching frequency.

### 3.2.5. Improvements

Improvements to the system can be done considering a more accurate model of the converter, for example adding the equivalent resistor of the inductor  $R_L$ , and the equivalent resistance of the output capacitor  $R_c$ , as in Fig. 3.15. In this section, is shown that considering the parasitic elements into the model increases the cross-over frequency, thus stability margins.

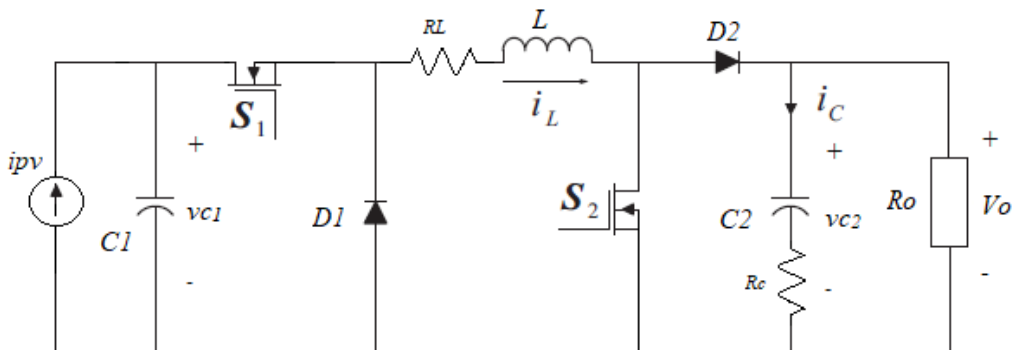


Fig. 3.15. Non-inverting Buck-Boost converter with parasitic elements.

Because of the importance of the Boost mode operations for the stability analysis and the design of the controller, only this mode is discussed. Therefore, in the Boost mode, the state space equations can be expressed as:

$$\begin{bmatrix} \dot{i}_L \\ \dot{v}_{C_1} \\ \dot{v}_{C_2} \end{bmatrix} = \begin{bmatrix} -\frac{R_L}{L} & \frac{1}{L} & 0 \\ -\frac{1}{C_1} & 0 & 0 \\ 0 & 0 & -\frac{1}{(R+R_c)C_2} \end{bmatrix} \begin{bmatrix} i_L \\ v_{C_1} \\ v_{C_2} \end{bmatrix} + \begin{bmatrix} 0 \\ 1 \\ 0 \end{bmatrix} ipv \quad (3.6)$$

when the switch S2 is on. And:

$$\begin{bmatrix} \dot{i}_L \\ \dot{v}_{C_1} \\ \dot{v}_{C_2} \end{bmatrix} = \begin{bmatrix} -\left(\frac{R_L}{L} + \frac{RcR}{(R+Rc)L}\right) & \frac{1}{L} & -\frac{1}{L}\left(\frac{R}{R+Rc}\right) \\ -\frac{1}{C_1} & 0 & 0 \\ \frac{R}{(R+Rc)C_2} & 0 & -\frac{1}{(R+Rc)C_2} \end{bmatrix} \begin{bmatrix} i_L \\ v_{C_1} \\ v_{C_2} \end{bmatrix} + \begin{bmatrix} 0 \\ 1 \\ 0 \end{bmatrix} ipv \quad (3.7)$$

when the switch S2 is off.

Again, to derive the linear transfer function of the system, the small-signal analysis is performed, and the frequency responses of the basic and the more accurate model are compared in Fig. 3.16.

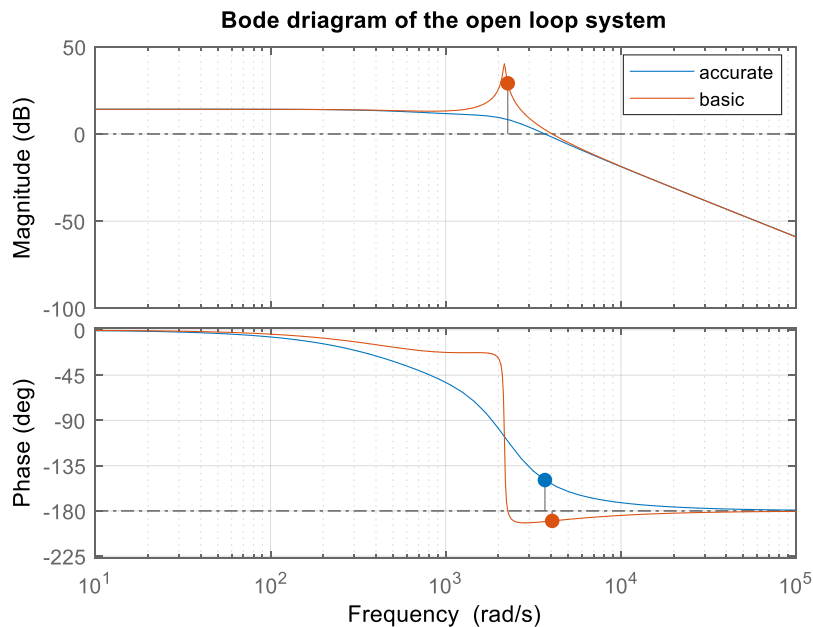


Fig. 3.16. Bode diagram of the basic and accurate model.

From the figure, it is clear that the dynamic and stability of the system when the parasitic components are considered are significantly improved [33]. This will result, during the design of the controller, to reach a compensated system with wider bandwidth, and hopefully better response of the overall system.

### 3.3 Model Predictive Control

Because of PV power fluctuations due to environmental conditions, energy storages are usually integrated in PV systems. In this study a battery energy storage (BES) is connected to the DC bus through a Bidirectional DC-DC converter, in order to balance the power between PV generation and load demand.

An effective control system, which can realize the bidirectional power flow of energy is needed, and in this research, an MPC strategy is proposed. The conventional cascade linear control method results in a complicated structure with multiple feedback loops and PWM modulation, which leads to slow dynamic response and hard tuning of the PI parameters, thus making the controller not easy to implement [71].

MPC approach is an attractive alternative to the classical control methods, it is fast, simple and easy to implement, it has the ability to include nonlinearities and constraints and can operate with multivariable. The main purpose of MPC method is to compensate the power difference between load and PV generation, while maintaining the DC bus voltage constant. Furthermore, battery life can be improved by implementing constraints on the SOC of the battery to avoid overcharge and over discharge. Fig 3.17 depicts the schematic diagram of the MPC control system used for the Bidirectional converter.

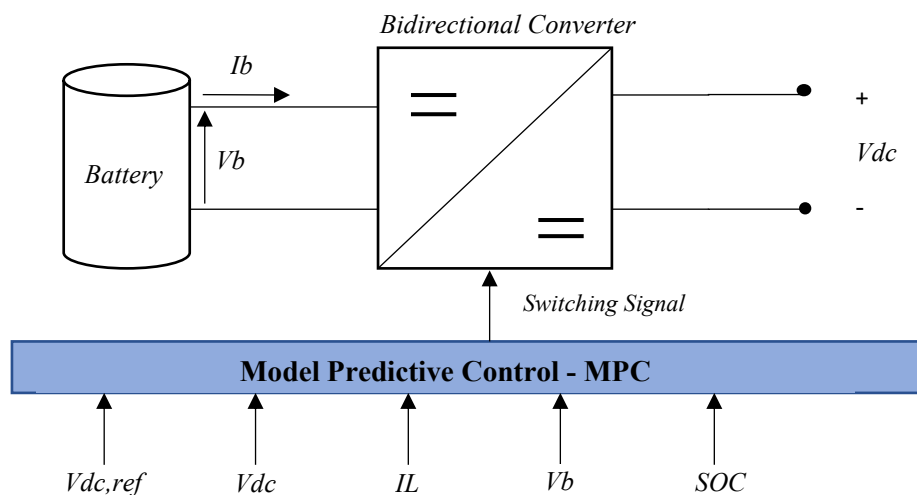


Fig. 3.17. MPC control scheme.

An MPC strategy is presented for the Bidirectional converter, in which the main idea is to use a model of the system to predict the future behavior of the controlled variables, so that the optimal control action can be determined by minimizing a predefined cost function.

The performance and feasibility of the proposed control strategy are evaluated through MATLAB simulations.

#### 3.3.1 MPC Principle of Operation

Model Predictive Control is an advanced control technique that has been used in process industries, mostly in chemical plants and oil refineries, since the 1970s. In these high-power systems with low switching frequency it currently represents the state of the art.

In recent years, its use has been expanding in the automotive and power electronics industry. The use of high switching frequencies wasn't possible at that time due to the large calculation time needed

---

for the control algorithm. Nowadays, with the improvement of modern microcontrollers and digital signal processors (DSPs), interest in the application of MPC in power electronics with high switching frequency is increasing significantly [80].

The principal advantages that are making MPC popular are:

- Concepts are very simple and intuitive;
- Controller implementation can also be simple, especially with horizon  $N = 1$ ;
- Can be applied to every system with known mathematical models;
- Has the ability to deal with nonlinearities;
- Can operate with multivariable;
- Has the ability to include constraints;

However, the larger number of calculations, increase the computational complexity compared to classical controllers. Moreover, because a discrete model is needed for the prediction of the variables, the quality of the model influences the quality of the resulting controller, and if the parameters of the system change in time, some adaptation or estimation algorithm must be considered [6].

The main characteristics of the strategy, as already said, is predicting the future behavior of the desired control variables for a specific time in the horizon, using a discrete model of the system. These predictions are then used for the selection of the optimal control action by minimizing a predefined cost function [6].

The discrete-time model used for prediction can be expressed in state-space as:

$$\begin{aligned} \mathbf{x}(k + 1) &= \mathbf{A}\mathbf{x}(k) + \mathbf{B}\mathbf{u}(k) \\ \mathbf{y}(k) &= \mathbf{C}\mathbf{x}(k) \end{aligned} \tag{3.8}$$

Then a cost function  $J$ , that represents the desired operation of the system is defined. This function takes in consideration the references, the states and the future actions.

$$J = J(\mathbf{x}(k), \mathbf{U}(k)) \tag{3.9}$$

Where  $\mathbf{U}(k) = [\mathbf{u}(k), \mathbf{u}(k + 1), \dots, \mathbf{u}(k + N - 1)]^T$ , is the control vector containing all the future control actions over a finite horizon in time  $N$ .

An optimization problem that consist of minimizing the cost function  $J$ , subject to the model of the system and the system constrains can be formulated:

$$\begin{aligned} &\text{minimize } J(k) \\ &\text{subject to } \mathbf{x}(k + 1) = f(\mathbf{x}(k), \mathbf{u}(k)) \end{aligned} \tag{3.10}$$

The aim of the optimization problem is to find the control sequence at step  $k$ ,  $\mathbf{U}(k)$ , that results in the optimal performance of the system, where the controller will apply only the first element of the sequence  $\mathbf{U}(1)$ . The optimization problem, is solved at each sampling time, using the new measured data to obtain the new sequence of optimal control actions.

The MPC principle of operation is represented in Fig. 3.18 [6], where it clearly shows that the future behavior of the system is predicted for  $k + N$  time steps in horizon, using the known data at time step  $k$ .

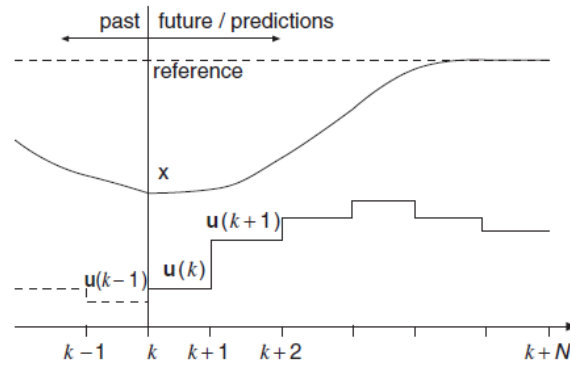


Fig. 3.18. MPC working principle.

### 3.3.2 Proposed Single-step Control Strategy

In this section, a simple but effective MPC strategy for the Bidirectional converter is proposed, in order to improve its dynamic performance. The advantage of the presented strategy is that the problem is formulated in a way that only one-step prediction horizon is needed to control the converter. Therefore, a proper cost function elaborated in terms of the inductor current is proposed.

The MPC working principle applied to the Bidirectional converter under study is illustrated in Fig. 3.19.

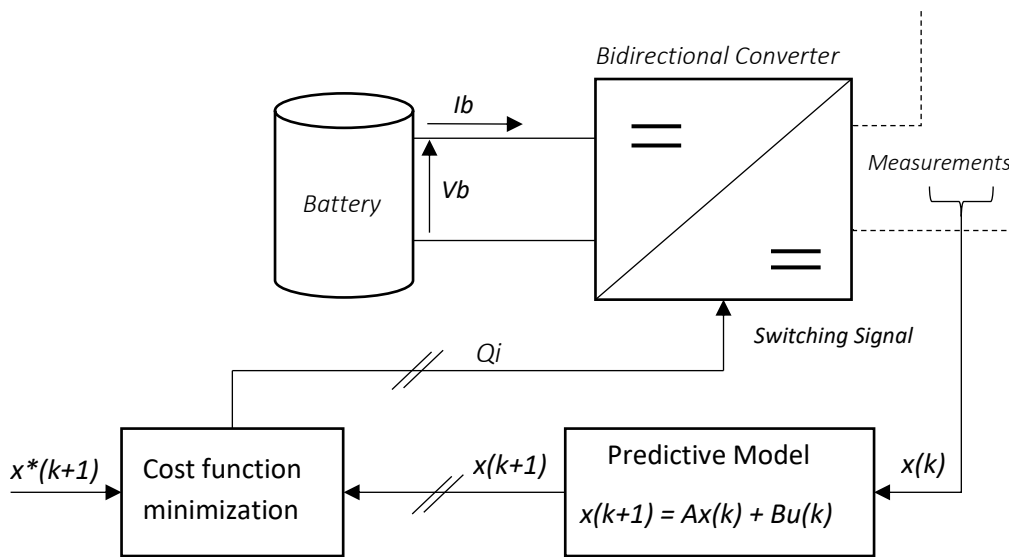


Fig. 3.19. Proposed MPC scheme for Bidirectional converter.

The scheme includes three parts, the prediction of the model, the calculation of the reference and the performance optimization. These three steps are required to be performed at each control interval.

Considering the Bidirectional converter analyzed in section 2.4, the equations representing the model of the system, for charging and discharging modes, were derived. The continuous-time inductance current equation of the converter, considering the state of the switches, is reported:

$$\frac{di_L(t)}{dt} = \frac{vb(t)}{L_b} - (1 - s(t)) \frac{v_{dc}(t)}{L_b} \quad (3.11)$$

where  $s$  represents the state of the switches,

$$s(t) = \begin{cases} 1, & \text{discharging mode} \\ 0, & \text{charging mode} \end{cases} \quad (3.12)$$

To obtain an accurate equation for the prediction block, the developed continuous-time model is discretized using Euler's approximation,

$$\frac{dx}{dt} = \frac{x(k+1) - x(k)}{T_s} \quad (3.13)$$

where  $T_s$ , is the sampling time. Therefore, the predicted inductor current is as follows:

$$i_L(k+1) = i_L(k) - (1 - s) \frac{T_s}{C_2} v_{dc}(k) - \frac{T_s}{L} vb(k) \quad (3.14)$$

A cost function, that ensure the power balance while maintaining the bus voltage constant, in terms of inductor current regulation, and considers SOC constrains, is formulated.

$$J_{s|_0^1} = |i_L^* - i_L(k+1)| \quad (3.15)$$

$$SOC_{min} \leq SOC \leq SOC_{max}$$

$J$  is defined as error between variable values and their reference value and is calculated for all possible switching states (1 and 0). The reference value is based on a simple power balance mathematical equality, between the input and output power of the converter, considering a unity efficiency and supposing that the battery current doesn't differ much from the inductance current.

$$i_L^* = \frac{(v_{dc}^*)^2}{R * vb(k)} \quad (3.16)$$

where  $v_{dc}^*$ , is the constant bus reference voltage (12 V).

The aim of the proposed cost function is to minimize the error between the inductor current reference  $i_L^*$ , and the predicted inductor current  $i_L(k+1)$ , to control the charging/discharging of the ESS while maintaining the bus voltage constant. Thus, at each sampling interval, the switching state  $Q_i$  that minimizes the cost function is selected and applied to the converter for the following sampling period. The flowchart, that illustrate the optimization process of the proposed MPC strategy is depicted in Fig. 3.20.

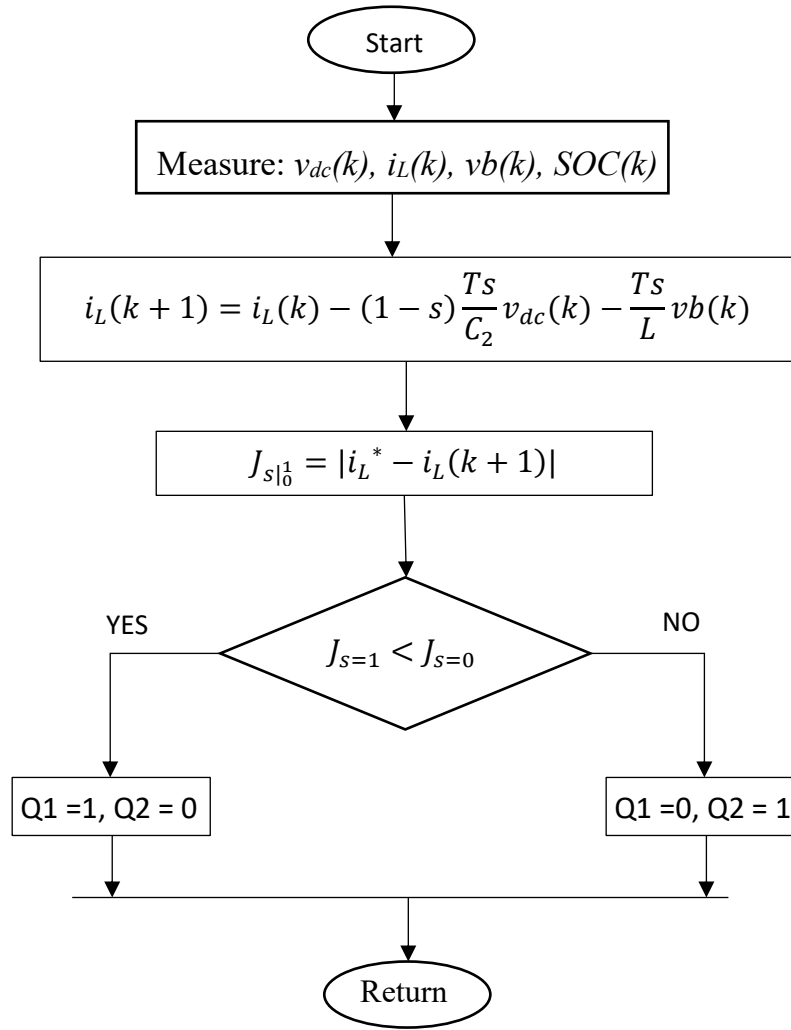


Fig. 3.20. Flowchart of the proposed MPC algorithm.

### 3.3.3 Implementation and Simulation

Finally, the proposed MPC strategy was implemented in MATLAB programming interface, together with the battery and the Bidirectional models, to simulate the performance of the control unit (see file script in **Appendix B.5**). The simulation results for a startup are shown in Fig. 3.21, using parameters given in table 13.

**Table 13.** Simulation Parameters.

Parameters	Values
$L_b$	33mH
$R$	5Ω
$C_2$	2mF
$C_b$	700μF
Initial State of Charge, $SOC_0$	60%
Switching frequency	20kHz

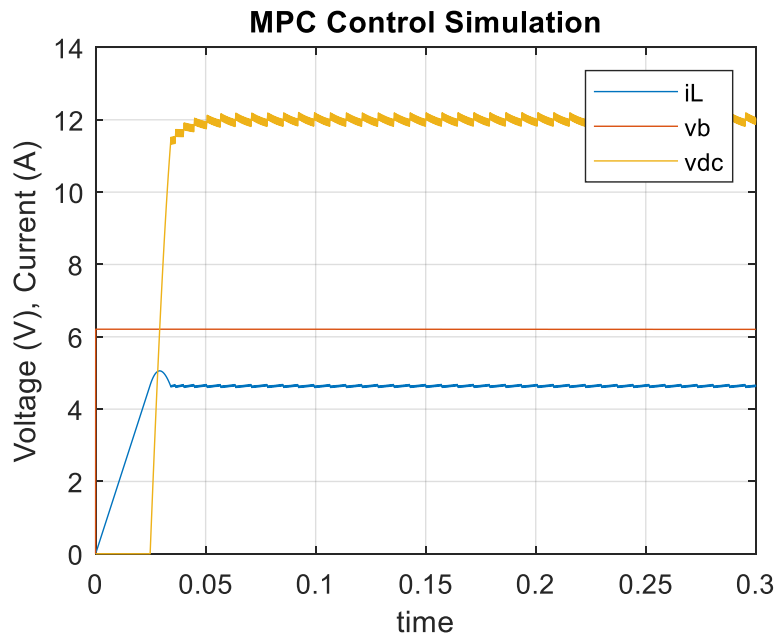


Fig. 3.21. Simulation results of the proposed control strategy.

In Fig. 3.21, the inductance current  $i_L$ , the input voltage  $v_b$ , and the output voltage  $v_{dc}$ , of the converter are depicted during the startup. As shown, the output voltage reaches its reference value in about 50ms, without any noticeable overshoot, and the inductance current rises to reach his nominal value. While the input voltage of the converter that is also the battery voltage slightly decreases. These results validate the performance of the proposed strategy.

In the considered scenario the load is powered only by the battery, thus the battery is expected to work in discharging mode, with a slowly decrement of the battery voltage. This can be proved considering the SOC of the Battery, as plotted in Fig. 3.22.

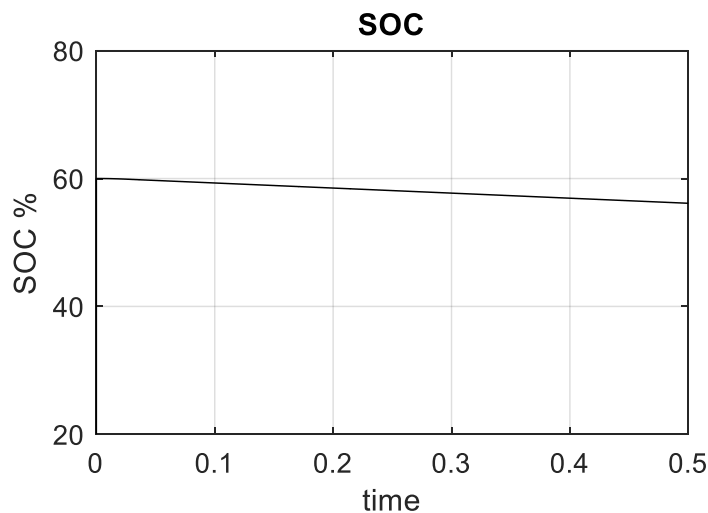


Fig. 3.22. State of charge of the battery during the simulation.

The initial SOC was set to 60% and it is easy to see that during the simulation time the SOC decreases, meaning that the battery is discharging.

### 3.4 Power Management Strategy

A power management strategy which coordinates the elements of the system must be designed to make the power flow more efficient and reliable.

The off-grid PV system with battery storage under study has five different operating modes according to the amount of power supplied by the PV panel, the power required by the load and the state of the battery. The energy constraints of the battery are determined by the SOC limits, implemented to improve battery life avoiding overcharge and over discharge. Considering the properties of a Lead Acid battery, the minimum and maximum SOC where chosen to be 40% and 80%, respectively.

The flowchart of the power management strategy developed to ensure stable operation under different operation modes is shown in Fig. 3.23.

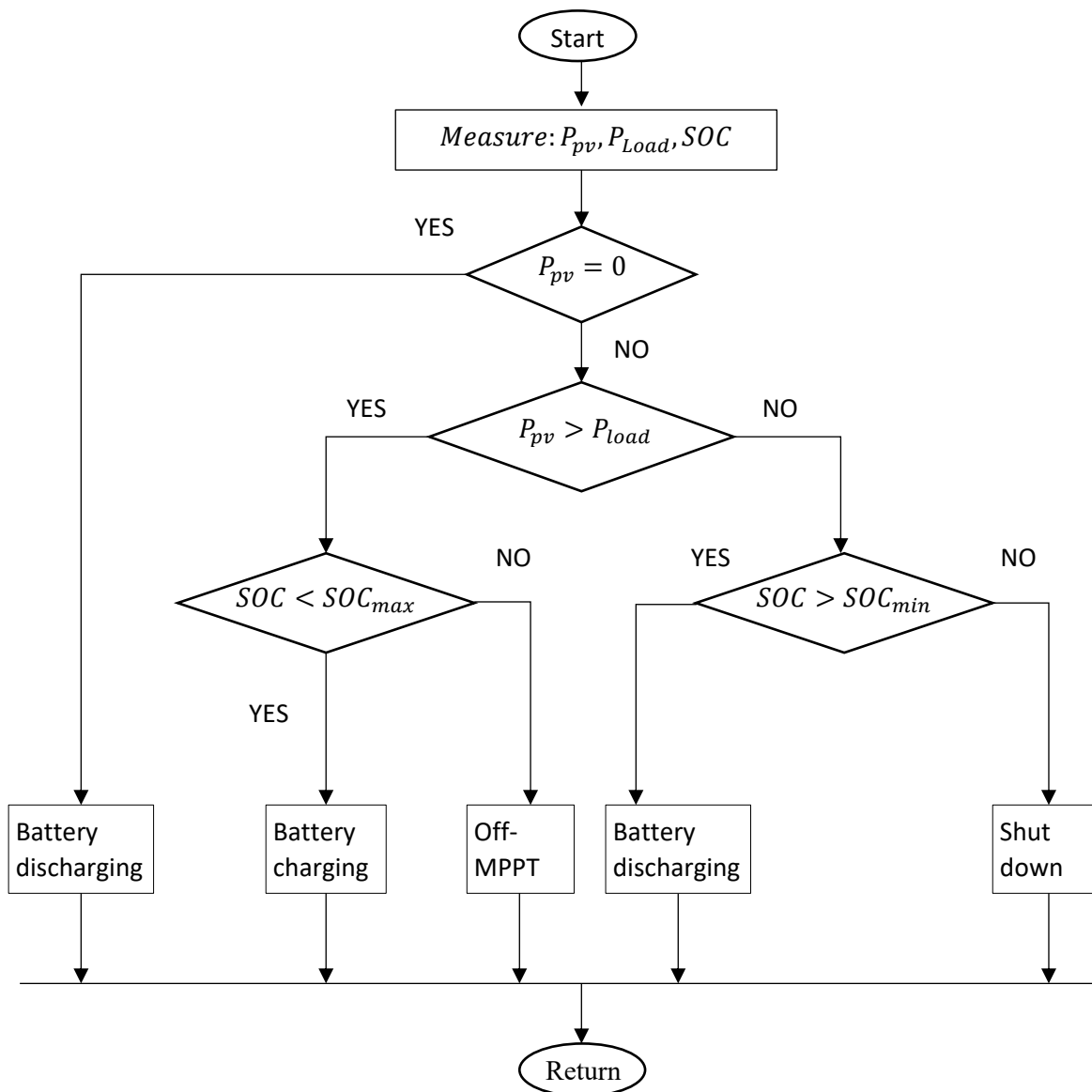


Fig. 3.23. Proposed power management algorithm.

Mode 1 :  $P_{pv} < P_{load}$  &  $SOC > SOC_{min}$ .

In this scenario, the PV panel cannot provide enough energy to power the load, thus the storage is used as a backup source. The PV panel works in MPPT to extract the maximum power and the Battery is discharged to meet the load demand and to stabilize the DC bus voltage.

*Mode 2 :  $P_{pv} < P_{load} & SOC < SOC_{min}$ .*

When the power generated by the PV is less than the power demand and the battery reaches its minimum value, the whole system is shut down.

*Mode 3 :  $P_{pv} > P_{load} & SOC < SOC_{max}$ .*

In this mode the PV generation is bigger than the load demand and the battery is not fully charged. As a result, the PV panel realizes the MPPT to power the load and the excess energy produced is used to charge the battery.

*Mode 4 :  $P_{pv} > P_{load} & SOC > SOC_{max}$ .*

When the PV generation is bigger than the load demand, but the battery is fully charged, the MPPT is quit from the PV panel to protect the battery from overcharging. As a result, the PV power feeds the load with off-MPPT operation and regulates the output voltage, while the Bidirectional converter remains disabled.

*Mode 5 : no  $P_{pv}$  &  $SOC_{min} < SOC < SOC_{max}$ .*

In this scenario there is no solar power the battery is charged. For example, this mode occurs during night. As a result, the PV panel is off, and all the load is supplied by the battery.

To further verify the performance of the proposed power management and the MPC control strategy, simulations for various scenarios are carried out.

The system was implemented in MATLAB programming interface. Simulation results plotted in the following figures, illustrate the charging and discharging of the battery for different modes of operation.

Worth to say, is that the non-inverting Buck-Boost converter, used to extract the maximum power from the PV array and that works as a current source converter, for these simulations was considered injecting constant current to the system. These results in fact are just a preliminary demonstration of the functionality of the proposed off-grid system. More accurate simulations and maybe experiments could be considered as a future work.

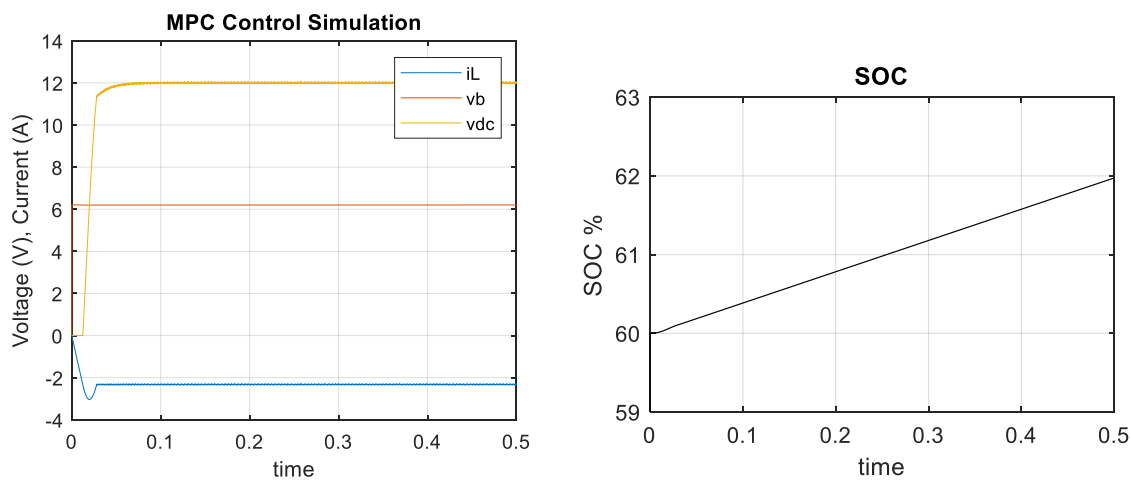


Fig. 3.24. Simulation results for charging mode.

In Fig. 3.24, the scenario where the  $P_{pv} > P_{load}$  &  $SOC < SOC_{max}$  (mode 3), is considered. Since the power generated from the PV panel is bigger the load demand, and the battery is not fully charged, the surplus solar power produced is used to charge the battery. In this mode the battery current is negative, and the SOC is increasing, meaning that the battery is charging.

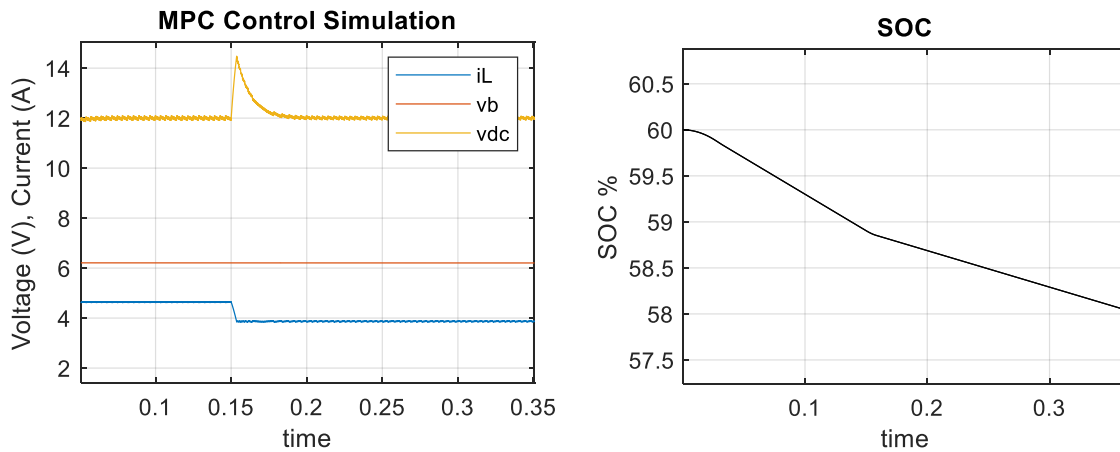


Fig. 3.25. Simulation results for a step-up change in the load.

In Fig. 3.25, the scenario where the battery is discharging and a step-up change in load occur is plotted. At time 0.15s, the load resistance is increased, from  $R = 5\Omega$  to  $R = 8\Omega$ . As shown, after a small overshoot the voltage returns to track its reference value, while the current suddenly decreases. Whereas the slope of the SOC also decreases, meaning that the battery discharging is slower.

---

## Chapter 4. Direct Voltage MPC

In the previous chapter the basic principles of model predictive control were exposed, and a simple but effective strategy that considers only one-step in the horizon was proposed. This is a common implementation of MPC in the field of power electronics, since the reduced prediction horizon is easy to obtain, requires less computational calculations and gives satisfactory results [81]. Moreover, in the proposed strategy the cost function was formulated in terms of current control rather than voltage control.

However, since the main control objective is the regulation of the output voltage of the Bidirectional converter, a different control strategy is presented. A direct voltage MPC cost function, which consider a larger prediction horizon, is formulated, and even though the implementation results in a more complex problem, the direct voltage MPC control with receding horizon can improve the steady state performance of the system.

In the following the strategy is explained and simulation results validating the proposal are carried out.

### 4.1 Cost Function Formulation

In this section the basic mathematical formulation of the proposed direct voltage MPC with receding horizon is explained [82].

Given a set plant dynamic and assuming that the system is linear, the discrete-time state space model can be expressed as:

$$\begin{aligned} \mathbf{x}(k+1) &= A\mathbf{x}(k) + B\mathbf{u}(k) + N\mathbf{w}(k) \\ \mathbf{y}(k) &= C\mathbf{x}(k) \end{aligned} \quad (4.1)$$

Where  $\mathbf{x}$  is the state vector of the system,  $\mathbf{u}$  is the input vector of the manipulated variables or input variables,  $\mathbf{w}$  is the vector of the disturbance variables and  $\mathbf{y}$  is the output vector.  $A, B, N, C$  are the system matrices.

The current state  $\mathbf{x}(k)$ , can be used to calculate the prediction of the future state and output variables over a finite number  $N$  of steps, where  $N$  is the prediction horizon. Starting from the step  $k+1$ , and assuming  $N=4$  (it can be easily generalized for  $N$  steps), the future state variables are calculated:

$$\begin{aligned} \mathbf{x}(k+1) &= A\mathbf{x}(k) + B\mathbf{u}(k) + N\mathbf{w}(k) \\ \mathbf{x}(k+2) &= A\mathbf{x}(k+1) + B\mathbf{u}(k+1) + N\mathbf{w}(k+1) \\ &= A^2\mathbf{x}(k) + AB\mathbf{u}(k) + B\mathbf{u}(k+1) + N\mathbf{w}(k+1) \\ \mathbf{x}(k+3) &= A\mathbf{x}(k+2) + B\mathbf{u}(k+2) + N\mathbf{w}(k+2) \\ &= A^3\mathbf{x}(k) + A^2B\mathbf{u}(k) + A^2N\mathbf{w}(k) + AB\mathbf{u}(k+1) + AN\mathbf{w}(k+1) \\ &\quad + B\mathbf{u}(k+2) + N\mathbf{w}(k+2) \\ \mathbf{x}(k+4) &= A\mathbf{x}(k+3) + B\mathbf{u}(k+3) + N\mathbf{w}(k+3) \\ &= A^4\mathbf{x}(k) + A^3B\mathbf{u}(k) + A^3N\mathbf{w}(k) + A^2B\mathbf{u}(k+1) + A^2N\mathbf{w}(k+1) \\ &\quad + AB\mathbf{u}(k+2) + AN\mathbf{w}(k+2) + B\mathbf{u}(k+3) + N\mathbf{w}(k+3) \end{aligned} \quad (4.2)$$

which in matrix form, become:

$$\begin{bmatrix} \mathbf{x}(k+1) \\ \mathbf{x}(k+2) \\ \mathbf{x}(k+3) \\ \mathbf{x}(k+4) \end{bmatrix} = \begin{bmatrix} A \\ A^2 \\ A^3 \\ A^4 \end{bmatrix} \mathbf{x}(k) + \begin{bmatrix} B & 0 & 0 & 0 \\ AB & B & 0 & 0 \\ A^2B & AB & B & 0 \\ A^3B & A^2B & AB & B \end{bmatrix} \begin{bmatrix} \mathbf{u}(k) \\ \mathbf{u}(k+1) \\ \mathbf{u}(k+2) \\ \mathbf{u}(k+3) \end{bmatrix} + \begin{bmatrix} N & 0 & 0 & 0 \\ AN & N & 0 & 0 \\ A^2N & AN & N & 0 \\ A^3N & A^2N & AN & N \end{bmatrix} \begin{bmatrix} \mathbf{w}(k) \\ \mathbf{w}(k+1) \\ \mathbf{w}(k+2) \\ \mathbf{w}(k+3) \end{bmatrix} \quad (4.3)$$

Finally, the predicted output variables are obtained,

$$\begin{bmatrix} \mathbf{y}(k+1) \\ \mathbf{y}(k+2) \\ \mathbf{y}(k+3) \\ \mathbf{y}(k+4) \end{bmatrix} = \begin{bmatrix} C & 0 & 0 & 0 \\ 0 & C & 0 & 0 \\ 0 & 0 & C & 0 \\ 0 & 0 & 0 & C \end{bmatrix} \begin{bmatrix} \mathbf{x}(k+1) \\ \mathbf{x}(k+2) \\ \mathbf{x}(k+3) \\ \mathbf{x}(k+4) \end{bmatrix} = \begin{bmatrix} CA \\ CA^2 \\ CA^3 \\ CA^4 \end{bmatrix} \mathbf{x}(k) + \begin{bmatrix} CB & 0 & 0 & 0 \\ CAB & CB & 0 & 0 \\ CA^2B & CAB & CB & 0 \\ CA^3B & CA^2B & CAB & CB \end{bmatrix} \begin{bmatrix} \mathbf{u}(k) \\ \mathbf{u}(k+1) \\ \mathbf{u}(k+2) \\ \mathbf{u}(k+3) \end{bmatrix} + \begin{bmatrix} CN & 0 & 0 & 0 \\ CAN & CN & 0 & 0 \\ CA^2N & CAN & CN & 0 \\ CA^3N & CA^2N & CAN & CN \end{bmatrix} \begin{bmatrix} \mathbf{w}(k) \\ \mathbf{w}(k+1) \\ \mathbf{w}(k+2) \\ \mathbf{w}(k+3) \end{bmatrix} \quad (4.4)$$

which can be written in a more compact form, as:

$$\mathbf{Y} = \mathbf{F}\mathbf{x}(k) + \boldsymbol{\phi}\mathbf{U}(k) + \mathbf{Z}\mathbf{W}(k) \quad (4.5)$$

where

$$\mathbf{Y} = \begin{bmatrix} \mathbf{y}(k+1) \\ \mathbf{y}(k+2) \\ \mathbf{y}(k+3) \\ \mathbf{y}(k+4) \end{bmatrix}; \mathbf{U}(k) = \begin{bmatrix} \mathbf{u}(k) \\ \mathbf{u}(k+1) \\ \mathbf{u}(k+2) \\ \mathbf{u}(k+3) \end{bmatrix}; \mathbf{W}(k) = \begin{bmatrix} \mathbf{w}(k) \\ \mathbf{w}(k+1) \\ \mathbf{w}(k+2) \\ \mathbf{w}(k+3) \end{bmatrix} \quad (4.6)$$

$$\mathbf{F} = \begin{bmatrix} CA \\ CA^2 \\ CA^3 \\ CA^4 \end{bmatrix}; \boldsymbol{\phi} = \begin{bmatrix} CB & 0 & 0 & 0 \\ CAB & CB & 0 & 0 \\ CA^2B & CAB & CB & 0 \\ CA^3B & CA^2B & CAB & CB \end{bmatrix}; \mathbf{Z} = \begin{bmatrix} CN & 0 & 0 & 0 \\ CAN & CN & 0 & 0 \\ CA^2N & CAN & CN & 0 \\ CA^3N & CA^2N & CAN & CN \end{bmatrix} \quad (4.7)$$

Important to notice, is that all predicted variables are formulated in terms of the state variables at time  $k$  and on the future control actions  $[\mathbf{u}(k); \mathbf{u}(k+1); \mathbf{u}(k+2); \mathbf{u}(k+3)]^T$  [82].

Since the main control objective is to make the output voltage of the converter to track the reference voltage, a cost function is formulated as follows:

$$J(k, \mathbf{U}(k)) = \|\mathbf{V}_r - \mathbf{Y}\|_2^2 \quad (4.8)$$

where  $\mathbf{V}_r$ , is the reference voltage vector.

The cost function of equation (4.8) is formulated based on the norm two, which produce a quadratic function and thus results in a convex optimization problem to be solved [83]. Explicating the norm and substituting the equation (4.5) to (4.8), the objective function can be expressed as:

$$\begin{aligned}
J(k) &= (\mathbf{V}_r - \mathbf{Y})^T (\mathbf{V}_r - \mathbf{Y}) \\
&= (\mathbf{V}_r - \mathbf{F}\mathbf{x}(k) - \mathbf{Z}\mathbf{W}(k))^T (\mathbf{V}_r - \mathbf{F}\mathbf{x}(k) - \mathbf{Z}\mathbf{W}(k)) \\
&\quad - \mathbf{U}(k)^T \boldsymbol{\phi}^T (\mathbf{V}_r - \mathbf{F}\mathbf{x}(k) - \mathbf{Z}\mathbf{W}(k)) \\
&\quad - (\mathbf{V}_r - \mathbf{F}\mathbf{x}(k) - \mathbf{Z}\mathbf{W}(k))^T \boldsymbol{\phi} \mathbf{U}(k) + \mathbf{U}(k)^T \boldsymbol{\phi}^T \boldsymbol{\phi} \mathbf{U}(k)
\end{aligned} \tag{4.9}$$

In order to get the optimal control vector at time  $k$ ,  $\mathbf{U}(k)$ , the cost function need to be minimized, and because, as already said, the optimization problem results in a convex problem, the optimum control is obtained by first calculating the gradient of the cost function and then imposing it equal to zero [82].

The first order partial derivative of the cost function, pay attention to the properties of matrices, results to be:

$$\nabla J(k, \mathbf{U}(k)) = -2\boldsymbol{\phi}^T (\mathbf{V}_r - \mathbf{F}\mathbf{x}(k) - \mathbf{Z}\mathbf{W}(k)) + 2\boldsymbol{\phi}^T \boldsymbol{\phi} \mathbf{U}(k) \tag{4.10}$$

and imposing the (4.10) equal to zero  $\nabla J(k) = 0$ , the optimal control action is extracted:

$$\mathbf{U}(k) = \boldsymbol{\phi}^{-1} (\mathbf{V}_r - \mathbf{F}\mathbf{x}(k) - \mathbf{Z}\mathbf{W}(k)) \tag{4.11}$$

Thus, the first element of the optimal sequence,  $\mathbf{U}(1)$ , which represent the optimal switching state, is selected and applied to the converter for the following sampling period. Finally, the described process to determine the control input is repeated with the new measured variables [83].

## 4.2 Problem Statement and Small-signal Model

In this section the previous proposed process is applied to the Bidirectional converter, with the aim to charge and discharge the battery while regulating the output voltage of the converter.

The continuous-time equations of the Bidirectional converter, for charging and discharging modes, derived in section 2.4, are reported:

$$\begin{aligned}
\frac{di_L}{dt} &= \frac{vb}{L_b} - (1-s) \frac{v_{dc}}{L_b} \\
\frac{dv_{dc}}{dt} &= (1-s) \frac{i_L}{C_2} - \frac{v_{dc}}{RC_2}
\end{aligned} \tag{4.12}$$

where, as already known,  $s$  represents the state of the switches,

$$s = \begin{cases} 1, & \text{discharging mode} \\ 0, & \text{charging mode} \end{cases} \tag{4.13}$$

The continuous-time model expressed in state space, is:

$$\begin{cases} \dot{\mathbf{x}} = \mathbf{A}\mathbf{x} + \mathbf{B}\mathbf{u} + \mathbf{N}\mathbf{w} \\ \mathbf{y} = \mathbf{C}\mathbf{x} \end{cases} \quad (4.14)$$

$$\begin{bmatrix} \dot{i}_L \\ \dot{v}_{dc} \end{bmatrix} = \begin{bmatrix} 0 & -\frac{1}{L} \\ \frac{1}{C_2} & -\frac{1}{RC_2} \end{bmatrix} \begin{bmatrix} i_L \\ v_{dc} \end{bmatrix} + \begin{bmatrix} \frac{v_{dc}}{L} \\ -\frac{i_L}{C_2} \end{bmatrix} s + \begin{bmatrix} 1 \\ 0 \end{bmatrix} vb \quad (4.15)$$

$$[v_{dc}] = [0 \quad 1] \begin{bmatrix} i_L \\ v_{dc} \end{bmatrix} \quad (4.16)$$

The required base model to calculate the predictions is the discrete-time model, thus from the continuous-time equations the discrete-time model in state space is obtained [84]:

$$\begin{cases} \mathbf{x}(k+1) = \mathbf{A}\mathbf{x}(k) + \mathbf{B}\mathbf{u}(k) + \mathbf{N}\mathbf{w}(k) \\ \mathbf{y}(k) = \mathbf{C}\mathbf{x}(k) \end{cases} \quad (4.17)$$

$$\begin{bmatrix} i_L(k+1) \\ v_{dc}(k+1) \end{bmatrix} = \begin{bmatrix} 1 & -\frac{T_s}{L} \\ \frac{T_s}{C_2} & \left(1 - \frac{1}{RC_2}\right) \end{bmatrix} \begin{bmatrix} i_L(k) \\ v_{dc}(k) \end{bmatrix} + \begin{bmatrix} \frac{T_s}{L} v_{dc}(k) \\ -\frac{T_s}{C_2} i_L(k) \end{bmatrix} s(k) + \begin{bmatrix} T_s \\ 0 \end{bmatrix} vb(k) \quad (4.18)$$

$$[v_{dc}(k)] = [0 \quad 1] \begin{bmatrix} i_L(k) \\ v_{dc}(k) \end{bmatrix} \quad (4.19)$$

with,

$$\mathbf{x}(k) = \begin{bmatrix} i_L(k) \\ v_{dc}(k) \end{bmatrix}; \quad \mathbf{y}(k) = [v_{dc}(k)]; \quad \mathbf{u}(k) = s(k); \quad \mathbf{w}(k) = vb(k); \quad (4.20)$$

$$\mathbf{A} = \begin{bmatrix} 1 & -\frac{T_s}{L} \\ \frac{T_s}{C_2} & \left(1 - \frac{1}{RC_2}\right) \end{bmatrix}; \quad \mathbf{B} = \begin{bmatrix} \frac{T_s}{L} v_{dc}(k) \\ -\frac{T_s}{C_2} i_L(k) \end{bmatrix}; \quad \mathbf{N} = \begin{bmatrix} T_s \\ 0 \end{bmatrix}; \quad \mathbf{C} = [0 \quad 1] \quad (4.21)$$

where  $T_s$ , is the sample time, and the matrices  $\mathbf{A}, \mathbf{B}, \mathbf{N}, \mathbf{C}$  for simplicity have the same names of that of the continuous-time model.

However, because the model of the system is nonlinear and moreover the matrix  $\mathbf{B}$ , of the input variable is a time-varying matrix, the direct optimal solution to the control problem using the equations presented in the previous section is not possible. Therefore, the system is linearized using the well-known small-signal analysis so that the small-signal discrete-time model can be utilized to calculate the optimal control actions, that in this case corresponds to the small-signal variations of the duty cycle, since with this approach the state of the switch also corresponds to the duty cycle, as can be easily notice from (4.12).

Therefore, the averaging method is used to obtain first the steady-state model of the converter and then the needed small-signal model. The method is omitted as it was already presented in chapter 2. From equation (4.12), which is equivalent to the averaged model of the converter, the steady-state model is obtained.

$$\begin{cases} \mathbf{0} = \mathbf{A}\mathbf{X} + \mathbf{B}\mathbf{U} + \mathbf{N}\mathbf{W} \\ \mathbf{Y} = \mathbf{C}\mathbf{X} \end{cases} \rightarrow \begin{cases} \mathbf{X} = -\mathbf{A}^{-1}(\mathbf{B}\mathbf{U} + \mathbf{N}\mathbf{W}) \\ \mathbf{Y} = -\mathbf{C}\mathbf{A}^{-1}(\mathbf{B}\mathbf{U} + \mathbf{N}\mathbf{W}) \end{cases} \quad (4.22)$$

$$\begin{bmatrix} 0 \\ 0 \end{bmatrix} = \begin{bmatrix} 0 & -\frac{1}{L} \\ \frac{1}{C_2} & \frac{1}{RC_2} \end{bmatrix} \begin{bmatrix} I_L \\ V_{dc} \end{bmatrix} + \begin{bmatrix} \frac{V_{dc}}{L} \\ -\frac{I_L}{C_2} \end{bmatrix} S + \begin{bmatrix} 1 \\ 0 \end{bmatrix} Vb \quad (4.23)$$

$$[V_{dc}] = [0 \quad 1] \begin{bmatrix} I_L \\ V_{dc} \end{bmatrix} \quad (4.24)$$

Where the uppercase variables indicate the steady-state values. From (4.23) and (4.24) the steady-state values or DC values of the states and output variable can be calculated:

$$\begin{cases} I_L = \frac{V_{dc}}{(1-S)R} \\ V_{dc} = \frac{Vb}{(1-S)} \end{cases} \quad (4.25)$$

Finally, to investigate the performance of the convert the small-signal model is obtained. The small-signal analysis is the study of deviations from an operating point for a system subjected to small disturbances. The assumption made by this method is that the disturbances are so small that the deviation of the system can be described linearly [38]. Therefore, the linearized ac model is obtained:

$$\begin{cases} \hat{\mathbf{x}} = \mathbf{A}\hat{\mathbf{x}} + \mathbf{B}\hat{\mathbf{u}} + \mathbf{N}\hat{\mathbf{w}} \\ \hat{\mathbf{y}} = \mathbf{C}\hat{\mathbf{x}} \end{cases} \quad (4.26)$$

$$\begin{bmatrix} \hat{i}_L \\ \hat{v}_{dc} \end{bmatrix} = \begin{bmatrix} 0 & -\frac{(1-S)}{L} \\ \frac{(1-S)}{C_2} & -\frac{1}{RC_2} \end{bmatrix} \begin{bmatrix} \hat{i}_L \\ \hat{v}_{dc} \end{bmatrix} + \begin{bmatrix} \frac{V_{dc}}{L} \\ -\frac{I_L}{C_2} \end{bmatrix} \hat{s} + \begin{bmatrix} 1 \\ 0 \end{bmatrix} \hat{v}b \quad (4.27)$$

$$[\hat{v}_{dc}] = [0 \quad 1] \begin{bmatrix} \hat{i}_L \\ \hat{v}_{dc} \end{bmatrix} \quad (4.28)$$

where the variables indicated by “^”, represent the small-signal perturbations around an operating point, and the name of the matrices for simplicity is left the same.

The discrete-time model of the just calculated small-signal model, which will be used in the proposed MPC strategy to obtain the optimal actions for the controlled variable, is:

$$\begin{cases} \hat{\mathbf{x}}(k+1) = \mathbf{A}\hat{\mathbf{x}}(k) + \mathbf{B}\hat{\mathbf{u}}(k) + \mathbf{N}\hat{\mathbf{w}}(k) \\ \hat{\mathbf{y}}(k) = \mathbf{C}\hat{\mathbf{x}}(k) \end{cases} \quad (4.29)$$

$$\begin{bmatrix} \hat{i}_L(k+1) \\ \hat{v}_{dc}(k+1) \end{bmatrix} = \begin{bmatrix} 1 & -\frac{(1-S)Ts}{L} \\ \frac{(1-S)Ts}{C_2} & \left(1 - \frac{Ts}{RC_2}\right) \end{bmatrix} \begin{bmatrix} \hat{i}_L(k) \\ \hat{v}_{dc}(k) \end{bmatrix} + \begin{bmatrix} \frac{V_{dc}Ts}{L} \\ -\frac{I_L Ts}{C_2} \end{bmatrix} \hat{s} + \begin{bmatrix} Ts \\ 0 \end{bmatrix} \hat{v}b \quad (4.30)$$

$$[\widehat{v}_{dc}(k+1)] = [0 \quad 1] \begin{bmatrix} \widehat{i}_L(k+1) \\ \widehat{v}_{dc}(k+1) \end{bmatrix} \quad (4.31)$$

with,

$$\begin{aligned} \widehat{\mathbf{x}}(k) &= \begin{bmatrix} \widehat{i}_L(k) \\ \widehat{v}_{dc}(k) \end{bmatrix}; \text{ state variables (SV);} \\ \widehat{\mathbf{u}}(k) &= \widehat{s}(k); \text{ manipulated input (MV);} \\ \widehat{\mathbf{w}}(k) &= \widehat{vb}(k); \text{ disturbance input (DV);} \\ \widehat{\mathbf{y}}(k) &= [\widehat{v}_{dc}(k)]; \text{ output variable (OV);} \end{aligned} \quad (4.32)$$

### 4.3 Implementation and Simulation Results

In this section, the implementation and the simulation results are presented to validate the performance of the proposed MPC strategy.

First of all, the small-signal model of the Bidirectional converter was calculated at the steady state operating point ( $v_{dc} = v_{dc,ref} = 12V$ ) using equation (4.27) and parameters in Table 14.

**Table 14.** Simulation parameters at nominal operating point.

Parameters	Values
$Lb$	33mH
$R$	5Ω
$C2$	800μF
$Vb$	6V
Steady state duty cycle, $S$	0.5

The calculated linearized model in state space form was then implemented in MATLAB using the MPC Toolbox, to obtain the simulation results. The MPC Toolbox, is a collection of MATLAB functions used for interactively design and simulate MPC controllers [85].

Knowing the small-signal system, the state space model is implemented by define the MPC input and output signals of the plant, such as: the manipulated variable (MV) that corresponds to the small-signal duty cycle  $\widehat{s}$ ; the disturbance input (DV) represented by the variations of the battery voltage  $\widehat{vb}$ ; and the manipulated output (MO), that corresponds to the controlled output voltage  $\widehat{v}_{dc}$ .

Therefore, a command line '*mpc*', is used to create a model predictive controller object based on the state space model, and the predictive model is developed setting the sample time,  $T_s$ .

The properties of the MPC controller, such as prediction horizon, control horizon and system constraints can be easily specified.

The implemented algorithm which make use of the MPC Toolbox is presented in **Appendix C.1**. The MPC objective properties can be seen by just running the script. Simulation results are shown in Figs. 4.1 – 4.2.

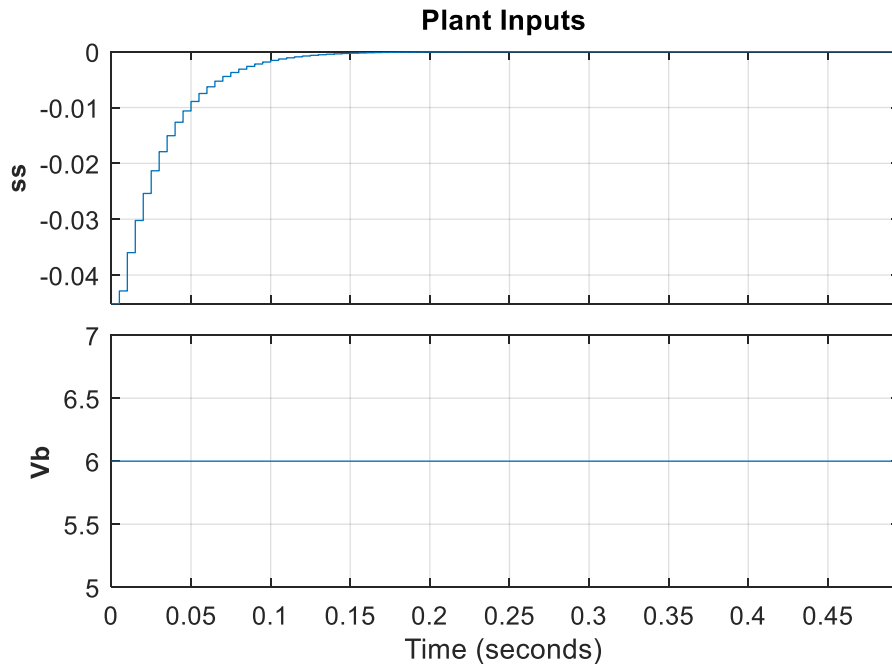


Fig. 4.1. Top: manipulated variable; bottom: disturbance input.

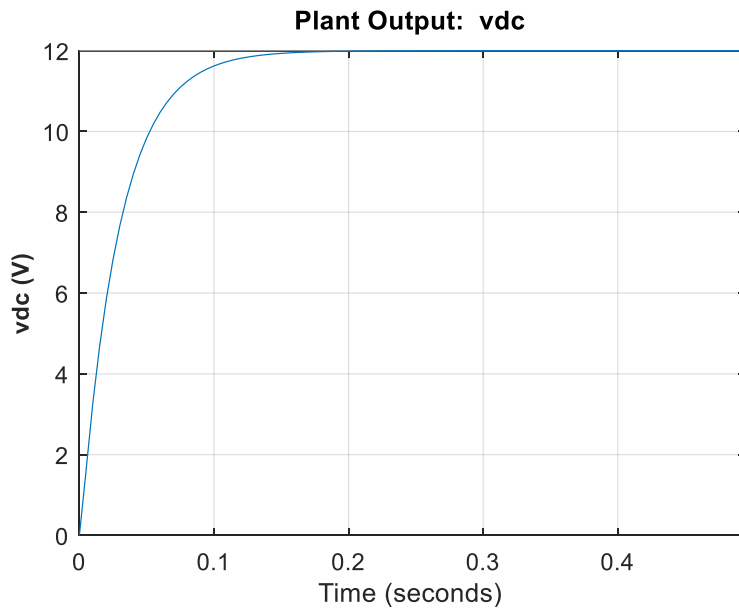


Fig. 4.2. Controlled output voltage.

In figure 4.1, the MV and the DV are plotted. The MV, here represented as  $ss$ , is the small-signal variation of the state of the switch  $s$  that is equivalent to the small-signal duty cycle. Therefore, to get the optimal control action, which allows the output voltage of the converter to track the reference, the obtained control sequence of the MV need to be added to the steady state duty cycle  $S$ . In practice, the optimal solution is calculated as:

$$s = S + ss \tag{4.33}$$

In the same figure the DV, represented by the battery voltage  $v_b$ , is plotted, and because of its slow dynamics it was considered as a constant value.

The output voltage of the converter during the start-up is shown in Fig. 4.2. As can be seen, the output voltage tracks his reference value with a good dynamic. This validate the performance of the proposed strategy. However, is important to mention that an higher sample time, compared to the one used in the current control presented in the section 3.3, was used. The sample time chosen to reach this result was  $T_s = 0.005s$ , and the prediction horizon  $N = 10$ .

This negative aspect could be due to sensitivity problems connected to the proposed MPC strategy. An in-depth analysis to better understand the challenges of this control and try to use new control strategies can be done as a future work.

Moreover, because the MPC designer Toolbox returns a continuous sequence of the optimal control actions, for a successful implementation on a microcontroller, the controller output needs to be discretized. Hence, a PWM is necessary to be implemented to convert the continuous optimal control to a discrete control actuation (Fig. 4.3), that can directly drive the switches.

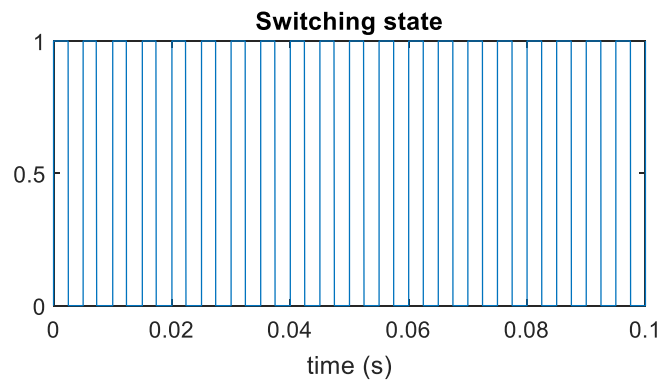
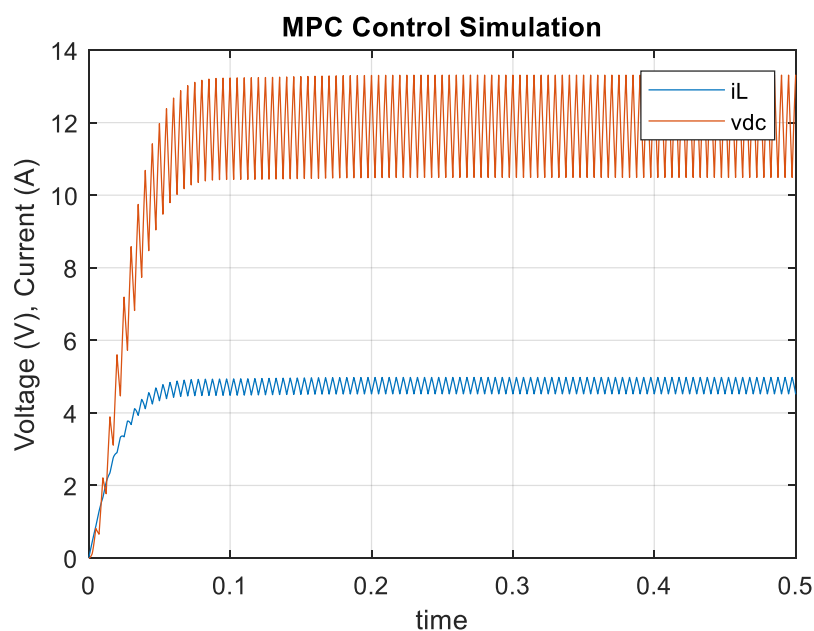


Fig. 4.3. Zoom of the switching signal generated from the continuous controller output.

Finally, by implementing the PWM into the system, to have a discrete switching signal, the output voltage of the converter and the inductance current are obtained, as in Fig. 4.28.



4.28. Controlled output voltage and inductance current with PWM.

As shown in figure, although the output voltage reaches its reference value with a good dynamic, in steady state the voltage presents a pronounced ripple. This problem is mostly due to the high sample time used.

#### 4.4 Sensitivity Analysis

To have a specific knowledge of the dynamic that characterize the MPC and to understand the limits of the approach, a sensitivity analysis is performed in this section.

The small-signal model of the Bidirectional converter obtained in section 4.3, is implemented in MATLAB using the approach explained in section 4.1.

The sensitivity analysis, that briefly is the study of how the uncertainty in the output of a system can be allocated to different sources of uncertainty in its inputs [86], is applied in the specific model adjusting a weight factor  $w_1$ , introduced in the cost function, as:

$$J(k, \mathbf{U}(k)) = w_1 \|\mathbf{V}_r - \mathbf{Y}\|_2^2 \quad (4.34)$$

to improve the MPC performance.

The first analysis, with parameters of table 14, is executed. In this step, the model is simulated for a decreasing sample time  $T_s$ , (sample rate 0.001), and the results are reported in table 15. As can be seen, the voltage reference and the weight factor are left constant during the simulation, while the sample time has been reduced. From the table, it can be noticed that the tracking is well achieved, except for the last simulation, and that with decreasing in  $T_s$ , the voltage ripple is also reduced. While step by step  $T_s$  diminishes, the settling time augments, and unfortunately at a certain point for a certain  $T_s$ , the system explodes and thus the control became pointless. Obviously, all the measures reported are calculated at the same time (0.5s), and the underlined cells indicate the changed variable.

**Table 15.** Simulation parameter results with decrements in  $T_s$ , at nominal operating point.

<i>n.</i>	<i>Vref</i>	<i>Ts (s)</i>	<i>w1</i>	<i>s</i>	<i>Vdc (V)</i>	<i>Vdc ripple (V)</i>	<i>IL (A)</i>
1	12	0,005	0,05	0,499	≈12	4,76	4,7
2	12	0,004	0,05	0,5006	≈12	3,94	4,75
3	12	0,003	0,05	0,5022	≈12	3	4,8
4	12	0,002	0,05	0,504	≈12	2,1	4,86
5	12	0,001	0,05	0,5062	≈12	1	4,9
6	12	0,0009	0,05	0,498	≈12	0,9	4,78
7	12	0,0008	0,05	0,494	≈12	0,8	4,7
8	12	0,0007	0,05	0,4953	≈12	0,7	4,68
9	12	0,0006	0,05	0,5023	≈12	0,6	4,8
10	12	0,0005	0,05	0,5086	≈12	0,5	4,92
11	12	0,0004	0,05	0,489	≈12	0,4	4,62
12	12	0,0003	0,05	0,46	≈12	0,2	4,1
13	12	0,0002	0,05	0	∞	/	0

The second block of simulations is executed for a constant  $T_s$  (0.002s) and increasing the weight  $w_1$ . The parameters results are reported in table 16. From the table, and considering the first simulations, it can be noticed that increasing the weight, also increases the value of the voltage

reference, the duty cycle  $s$  and the current. Then when the duty cycle has reached a maximum point it starts to decrease again, and at a certain point ( $w_1 = 0.45$ ), the voltage goes to zero and the current explode to infinite.

**Table 16.** Simulation parameter results with constant  $T_s$ , and a decreasing weight  $w_1$ .

$n.$	$V_{ref}$	$T_s$ (s)	$w_1$	$s$	$V_{dc}$ (V)	$V_{dc}$ ripple (V)	$I_L$ (A)
1	12	0,002	0,05	0,504	$\approx 12$	2,1	4,86
2	12	0,002	0,1	0,511	$\approx 12$	2,1	5
3	12	0,002	0,15	0,5196	$\approx 12$	2,1	5,2
4	12	0,002	0,2	0,6	$\approx 14$	3	6,8
5	12	0,002	0,25	0,7367	$\approx 15$	3,5	10,6
6	12	0,002	0,3	0,6714	$\approx 13,5$	3	8
7	12	0,002	0,35	0,4081	$\approx 10$	1,5	3,4
8	12	0,002	0,4	0,2893	$\approx 8,4$	0,8	2,4
9	12	0,002	0,45	1	0	/	54 $\uparrow$
10	12	0,002	0,5	1	0	/	77 $\uparrow$

For a better point of view on the problem, the simulation number 10 is plotted in Fig. 4.4.

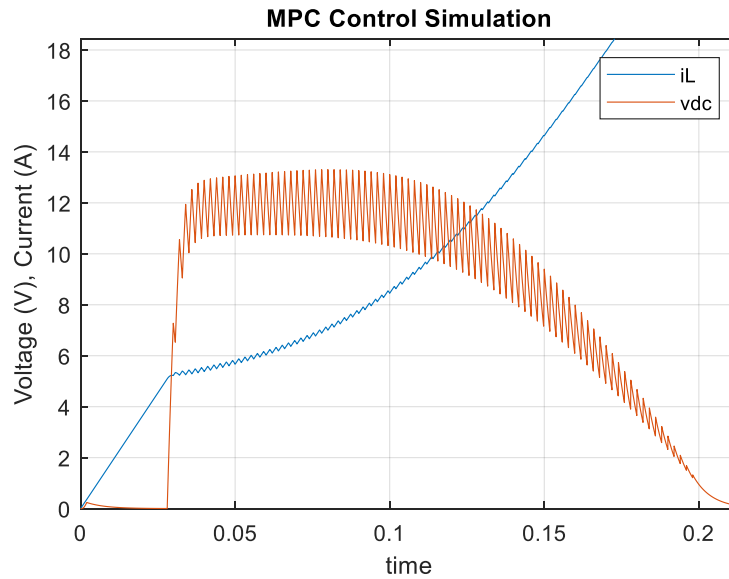


*Fig. 4.4.* Plotted results for simulation  $n. 10$  of table 16.

For the last analysis, the const function reported in (4.34) is formulated in a different way, as:

$$J(k, \mathbf{U}(k)) = w_1 \|\mathbf{V}_r - \mathbf{Y}\|_2^2 + w_2 \|\Delta \mathbf{U}\|_2^2 \quad (4.35)$$

where a second term,

$$\Delta U(k) = u(k) - u(k - 1) \quad (4.36)$$

with a weight factor  $w_2$ , is added to penalize the difference between two different control values. A detailed formulation of the const function presented in (4.35) can be found in [83].

In the last block of simulations, the sample time and both the weight factors are adjusted with the aim to see the changes in the voltage current and duty cycle. Results are reported in table 17.

**Table 17.** Simulation parameter results changing  $T_s$ ,  $w_1$  and  $w_2$ .

$n.$	$V_{ref}$	$T_s$ (s)	$w_1$	$w_2$	$s$	$V_{dc}$ (V)	$V_{dc}$ ripple (V)	$i_L$ (A)
1	12	0,005	0,05	0	0,499	$\approx 12$	4,8	4,7
2	12	0,005	0,05	1	0,5	$\approx 12$	4,8	4,7
3	12	0,005	0,05	5	0,506	$\approx 12$	4,8	4,7
4	12	0,005	0,05	10	0,513	$\approx 12$	4,8	4,9
5	12	0,005	0,2	10	0,516	$\approx 12$	4,9	5
6	12	0,005	0,25	10	0,518	$\approx 12$	5	5
7	12	0,005	0,3	10	0,521	$\approx 12$	5,2	5,1
8	12	0,005	0,3	1	0,489	$\approx 12$	4,6	4,5
9	12	0,004	0,3	1	0,528	$\approx 12$	4,3	5,3
10	12	0,001	0,05	0,2	0,497	$\approx 12$	1	4,75

From the table it can be seen that  $w_2$ , plays an important role in the achievement of the performance. As shown, in the first simulations only the  $w_2$  is changed, then also  $w_1$  is adjusted, and in the last simulation all three parameters are modified. The result for the last performed simulation is plotted in Fig. 4.5.

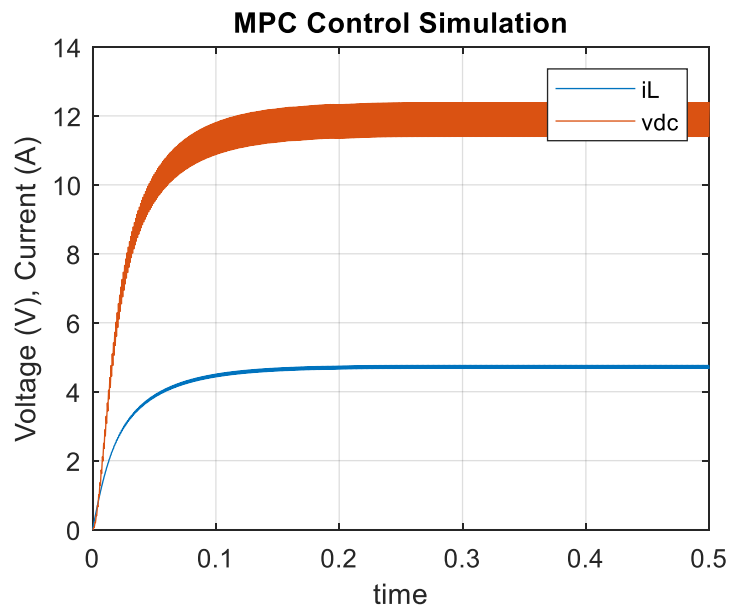


*Fig. 4.5. Plotted results for simulation n. 10 of table 17.*

Finally, can be stated that adjusting the weight factors the performance of the control can be improved.

---

## Conclusions

In summary, in this research essentially two control strategies were analyzed.

The first control unit, mainly used to extract the maximum power from the PV panel, includes the MPPT and the PI controller. This is a well-known strategy and the literature is plenty of different approaches, even advanced techniques of artificial intelligence were proposed to obtain efficiency improvements [12]. In the proposed study, although the tracking was well performed, limitations in the system were found. These limitations regard the use of the non-inverting Buck-Boost converter, which must be implemented as current-fed converter rather than a voltage-fed converter when interfaces a PV module. Moreover, this converter has two different mode of operations, Buck and Boost, but only one mode was considered for the design of the controller, thus limiting the dynamic.

Therefore, some improvements to the system can still be done, for example considering a more accurate model of the converter, which takes into account parasitic elements. This will increase the cross-over frequency, thus stability margins which hopefully will result in a better response of the overall system. Or also different control approaches, that assume both the operation modes can be considered, or even give the possibility to adopt a different converter for the same purpose.

For the second control unit, the MPC, two strategy were introduced.

The advantage of the single-step current control strategy, which is the most popular in the literature, is that the short prediction horizon requires much less computational calculations, and moreover a high frequency can be utilized, thus reducing the switching ripple and improving the dynamic of the tracking. Simulations proved the effectiveness of this strategy, however, since the control objective is the regulation of the voltage rather than the current, the method requires an outer loop to properly control the output voltage of the converter.

For the direct voltage MPC approach, it surely can be stated that is a powerful method with a high potential. Simulations of the small-signal model in the MPC Toolbox environment, gave satisfactory results, suggesting that even if the mathematical complexity is pronounced, the method presents great prospective. However, the implementation in MATLAB command line found out limitations regarding the relatively high sample time needed, and although the encountered problems were attenuated inserting weight factors in the cost function, the robustness of the dynamic response of the system remain still an open question. Unfortunately, so far not relevant papers were published implementing the voltage control on converters like Boost or Bidirectional types, that don't make use of any laborious tuning to control the voltage. On the contrary, the same direct voltage algorithm applied to Buck type converter demonstrates good response and a great potential, as presented in [83].

From this prospective can be intuited that the converter type plays an important role in the implementation of the MPC, and as stated in [87], a primary difficulty associated with Boost converter appears when controlling the output voltage without an intermediate current control loop, since the output voltage presents a non-minimum phase behavior with respect to the switching control action. Therefore, the direct voltage control become real challenging for this type of converters.

To conclude, an accurate analysis of the problem is necessary to overcome the encountered limitations, and probably different control approaches should also be considered. Personally, I think that since the potential of the proposed MPC strategy is great, the obstacles to overcome will not be less complicated.

---

## References

- [1] S. Mandelli, J. Barbieri, R. Mereu, and E. Colombo, 'Off-grid systems for rural electrification in developing countries: Definitions, classification and a comprehensive literature review', *Renewable and Sustainable Energy Reviews*, vol. 58, pp. 1621–1646, May 2016.
- [2] 'Mini-grids', *Wikipedia*. 23-May-2019.
- [3] E. Lorenzo, 'Photovoltaic Rural Electrification', *Progress in Photovoltaics: Research and Applications*, vol. 5, no. 1, pp. 3–27, Jan. 1997.
- [4] S. G. Malla and C. N. Bhende, 'Voltage control of stand-alone wind and solar energy system', *International Journal of Electrical Power & Energy Systems*, vol. 56, pp. 361–373, Mar. 2014.
- [5] H. A. Mostafa, R. E. Shatshat, and M. M. A. Salama, 'A review on energy management systems', in *2014 IEEE PES T&D Conference and Exposition*, Chicago, IL, USA, 2014, pp. 1–5.
- [6] J. Rodriguez and P. Cortes, *Predictive Control of Power Converters and Electrical Drives: Rodriguez/Predictive Control of Power Converters and Electrical Drives*. Chichester, UK: John Wiley & Sons, Ltd, 2012.
- [7] Fei Ding, Peng Li, Bibin Huang, Fei Gao, Chengdi Ding, and Chengshan Wang, 'Modeling and Simulation of Grid-connected Hybrid Photovoltaic/Battery Distributed Generation System'. IEEE, 2010.
- [8] Leppäaho, Jari, 'MPP-Tracking DC-DC Converters in Photovoltaic Applications - Implementation, Modeling and Analysis.' 2011.
- [9] M. M. Iqbal and K. Islam, 'Design And Simulation Of A PV System With Battery Storage Using Bidirectional DC-DC Converter Using Matlab Simulink', vol. 6, no. 07, p. 9, 2017.
- [10] S. Nanou, S. Papathanassiou, and G. Vokas, 'SMALL SIGNAL ANALYSIS AND GAIN SCHEDULING CONTROL OF A PHOTOVOLTAIC DC/DC CONVERTER', p. 5.
- [11] X. Zhao, H. Zhao, and M. Sugisaka, 'Study on the Technology of MPPT of the Solar Photovoltaic Based on the Model Predictive Control', *Journal of Robotics, Networking and Artificial Life*, vol. 3, no. 2, p. 111, 2016.
- [12] M. G. Villalva, T. G. de Siqueira, and E. Ruppert, 'Voltage regulation of photovoltaic arrays: small-signal analysis and control design', *IET Power Electronics*, vol. 3, no. 6, p. 869, 2010.
- [13] M. G. Villalva and E. F. Ruppert, 'Input-controlled buck converter for photovoltaic applications: modeling and design', in *4th IET International Conference on Power Electronics, Machines and Drives (PEMD 2008)*, York, UK, 2008, pp. 505–509.
- [14] M. Elbuluk and N. R. N. Idris, 'The role power electronics in future energy systems and green industrialization', in *2008 IEEE 2nd International Power and Energy Conference*, Johor Bahru, Malaysia, 2008, pp. 1–6.
- [15] M. G. Villalva and E. R. F., 'Analysis and simulation of the P&O MPPT algorithm using a linearized PV array model', in *2009 35th Annual Conference of IEEE Industrial Electronics*, Porto, Portugal, 2009, pp. 231–236.
- [16] M. G. Villalva, J. R. Gazoli, and E. R. Filho, 'Comprehensive Approach to Modeling and Simulation of Photovoltaic Arrays', *IEEE Transactions on Power Electronics*, vol. 24, no. 5, pp. 1198–1208, May 2009.
- [17] J.-K. Shiau, M.-Y. Lee, Y.-C. Wei, and B.-C. Chen, 'Circuit Simulation for Solar Power Maximum Power Point Tracking with Different Buck-Boost Converter Topologies', p. 20, 2014.
- [18] G. Walker, 'EVALUATING MPPT CONVERTER TOPOLOGIES USING A MATLAB PV MODEL', p. 6.
- [19] Ramdani Youcef, Moulay Fatima, Habbati Bellia, 'A detailed modeling of photovoltaic module using MATLAB', *NRIAG Journal of Astronomy and Geophysics*, vol. 3, no. 1, pp. 53–61, Jun. 2014.
- [20] E. K. Anto, J. A. Asumadu, and P. Y. Okyere, 'PID-based P&O MPPT Controller for Offgrid Solar PV Systems Using Ziegler-Nichols Tuning Method to Step, Ramp and Impulse Inputs', vol. 2, no. 7, p. 12, 2016.

- 
- [21] S. Sumathi, L. Ashok Kumar, and P. Surekha, *Solar PV and Wind Energy Conversion Systems*. Cham: Springer International Publishing, 2015.
- [22] S. Sx, 'The Natural Source for Electricity™', p. 38.
- [23] T. Suntio, J. Leppäaho, J. Huusari, and L. Nousiainen, 'Issues on Solar-Generator Interfacing With Current-Fed MPP-Tracking Converters', *IEEE Transactions on Power Electronics*, vol. 25, no. 9, pp. 2409–2419, Sep. 2010.
- [24] K. Kuwabara and T. Suzuki, 'A Pulse-Width Controlled DC-DC Converter Powered by a Constant-Current Source', in *INTELEC '84 - International Telecommunications Energy Conference*, New Orleans, LA, USA, 1984, pp. 468–472.
- [25] W. Xiao, N. Ozog, and W. G. Dunford, 'Topology Study of Photovoltaic Interface for Maximum Power Point Tracking', *IEEE Transactions on Industrial Electronics*, vol. 54, no. 3, pp. 1696–1704, Jun. 2007.
- [26] R. S. Weissbach and K. M. Torres, 'A noninverting buck-boost converter with reduced components using a microcontroller', in *Proceedings. IEEE SoutheastCon 2001 (Cat. No.01CH37208)*, Clemson, SC, USA, 2001, pp. 79–84.
- [27] H. Qiao, Y. Zhang, Y. Yao, and L. Wei, 'Analysis of Buck-Boost Converters for Fuel Cell Electric Vehicles', in *2006 IEEE International Conference on Vehicular Electronics and Safety*, Shanghai, China, 2006, pp. 109–113.
- [28] O. N. Almasi, V. Fereshtehpoor, M. H. Khooban, and F. Blaabjerg, 'Analysis, control and design of a non-inverting buck-boost converter: A bump-less two-level T-S fuzzy PI control', *ISA Transactions*, vol. 67, pp. 515–527, Mar. 2017.
- [29] K. Tawfique Ahmed, M. Datta, and N. Mohammad, 'A Novel Two Switch Non-inverting Buck-Boost Converter based Maximum Power Point Tracking System', *International Journal of Electrical and Computer Engineering (IJECE)*, vol. 3, no. 4, May 2013.
- [30] J. Leppäaho, L. Nousiainen, J. Puukko, J. Huusari, and T. Suntio, 'Implementing current-fed converters by adding an input capacitor at the input of voltage-fed converter for interfacing solar generator', in *Proceedings of 14th International Power Electronics and Motion Control Conference EPE-PEMC 2010*, Ohrid, Macedonia, 2010.
- [31] J. F. Silva and S. F. Pinto, 'Control Methods for Switching Power Converters', in *Power Electronics Handbook*, Elsevier, 2007, pp. 935–998.
- [32] A. Capel, J. C. Marpinard, J. Jalade, and M. Valentin, 'Current Fed and Voltage Fed Switching DC/DC Converters - Steady State and Dynamic Models their Applications in Space Technology', p. 10.
- [33] Y. Li, K. Liu, H. Wang, and M. Gu, 'Performance Evaluation of Controller Design Based on Accurate Model of Non-Inverting Buck Boost Converter Fed by Photovoltaic Module', vol. 30, no. 1, p. 16, 2017.
- [34] S.-Y. Tseng and H.-Y. Wang, 'A Photovoltaic Power System Using a High Step-up Converter for DC Load Applications', *Energies*, vol. 6, no. 2, pp. 1068–1100, Feb. 2013.
- [35] Jamri, 'Modeling and Control of a Photovoltaic Energy System Using the State-Space Averaging Technique', *American Journal of Applied Sciences*, vol. 7, no. 5, pp. 682–691, May 2010.
- [36] R. W. Erickson and D. Maksimović, *Fundamentals of power electronics*, 2nd ed. Norwell, Mass: Kluwer Academic, 2001.
- [37] L. Qin, S. Xie, C. Yang, and J. Xu, 'The interfacing stability of photovoltaic cells and current-fed MPPT converter', in *2013 IEEE ECCE Asia Downunder*, Melbourne, Australia, 2013, pp. 877–881.
- [38] P. Sahu, D. Verma, and S. Nema, 'Physical design and modelling of boost converter for maximum power point tracking in solar PV systems', in *2016 International Conference on Electrical Power and Energy Systems (ICEPES)*, Bhopal, India, 2016, pp. 10–15.
- [39] W. Xiao, W. Dunford, P. Palmer, and A. Capel, 'Regulation of Photovoltaic Voltage', *IEEE Transactions on Industrial Electronics*, vol. 54, no. 3, pp. 1365–1374, Jun. 2007.
- [40] K.-H. Chao, M.-C. Tseng, C.-H. Huang, Y.-G. Liu, and L.-C. Huang, 'Design and Implementation of a Bidirectional DC-DC Converter for Stand-Alone Photovoltaic Systems', vol. 2, p. 12, 2013.

- 
- [41] Hagedorn, Julian, 'Basic Calculations of a 4 Switch Buck-Boost Power Stage'. exas Instruments, 2018.
- [42] V. Yousefzadeh, 'Continuous and discontinuous time-domain modeling and simulation for DC-DC switching converters', in *2010 IEEE 12th Workshop on Control and Modeling for Power Electronics (COMPEL)*, Boulder, CO, USA, 2010, pp. 1–8.
- [43] 'Numerical methods for ordinary differential equations', *Wikipedia*. 07-Mar-2019.
- [44] 'Trapezoidal rule (differential equations)', *Wikipedia*. 05-May-2019.
- [45] F. Alvarado, 'Parallel Solution of Transient Problems by Trapezoidal Integration', *IEEE Transactions on Power Apparatus and Systems*, vol. PAS-98, no. 3, pp. 1080–1090, May 1979.
- [46] Milovan Kovačević, 'A Comparison of Discrete Models of DC-DC Converters', p. 4.
- [47] M. Sarrafzadeh, 'Department of electrical engineering and computer science', *ACM SIGDA Newsletter*, vol. 20, no. 1, p. 91, Jun. 1990.
- [48] M. S. Mamis, 'Discrete-Time State-Space Modeling of Distributed Parameter Transmission Line', in *EUROCON 2007 - The International Conference on 'Computer as a Tool'*, Warsaw, Poland, 2007, pp. 2078–2081.
- [49] G. Gurralla, A. Batageri, and D. L. Dinesha, 'Real-time simulation of power converters using Adomian decomposition method on mini-FSS', in *2016 IEEE International Conference on Power Electronics, Drives and Energy Systems (PEDES)*, Trivandrum, India, 2016, pp. 1–6.
- [50] A. M. Ameen, J. Pasupuleti, and T. Khatib, 'Simplified performance models of photovoltaic/diesel generator/battery system considering typical control strategies', *Energy Conversion and Management*, vol. 99, pp. 313–325, Jul. 2015.
- [51] A. Alsaleem, 'A Bidirectional Converter for Battery Based Energy System for Residential Applications', p. 61.
- [52] S. Li and B. Ke, 'Study of battery modeling using mathematical and circuit oriented approaches', in *2011 IEEE Power and Energy Society General Meeting*, San Diego, CA, 2011, pp. 1–8.
- [53] O. Tremblay, L.-A. Dessaint, and A.-I. Dekkiche, 'A Generic Battery Model for the Dynamic Simulation of Hybrid Electric Vehicles', in *2007 IEEE Vehicle Power and Propulsion Conference*, Arlington, TX, USA, 2007, pp. 284–289.
- [54] Munadir Ahmed, 'Modeling Lithium-ion Battery Chargers in PLECS'. Plexim Inc.
- [55] E. Raszmann, K. Baker, Y. Shi, and D. Christensen, 'Modeling stationary lithium-ion batteries for optimization and predictive control', in *2017 IEEE Power and Energy Conference at Illinois (PECI)*, Champaign, IL, USA, 2017, pp. 1–7.
- [56] H. B. Vika, 'Modelling of Photovoltaic Modules with Battery Energy Storage in Simulink/Matlab', p. 136.
- [57] O. Tremblay and L.-A. Dessaint, 'Experimental Validation of a Battery Dynamic Model for EV Applications', *World Electric Vehicle Journal*, vol. 3, no. 2, pp. 289–298, Jun. 2009.
- [58] S. R. P. Mantravadi, 'MODELING, SIMULATION & IMPLEMENTATION OF LI-ION BATTERY POWERED ELECTRIC AND PLUG-IN HYBRID VEHICLES', p. 153.
- [59] N. Kularatna, 'Rechargeable batteries and their management', *IEEE Instrumentation & Measurement Magazine*, vol. 14, no. 2, pp. 20–33, Apr. 2011.
- [60] P. Manimekalai, R. Harikumar, and S. Raghavan, 'An Overview of Batteries for Photovoltaic (PV) Systems', *International Journal of Computer Applications*, vol. 82, no. 12, pp. 28–32, Nov. 2013.
- [61] Greg Albright, Jake Edie, and Said Al-Hallaj, 'A Comparison of Lead Acid to Lithium-ion in Stationary Storage Applications'. AllCell Technologies LLC, Mar-2012.
- [62] M. Dürr, A. Cruden, S. Gair, and J. R. McDonald, 'Dynamic model of a lead acid battery for use in a domestic fuel cell system', *Journal of Power Sources*, vol. 161, no. 2, pp. 1400–1411, Oct. 2006.
- [63] L. Castañer and S. Silvestre, *Modelling photovoltaic systems using PSpice*. Chichester, England ; Hoboken, NJ: J. Wiley, 2002.
- [64] 'Panasonic LC-R067R2P Datasheet'. [Online]. Available: [https://www.mouser.it/datasheet/2/315/panasonic\\_vrla\\_lc-r067r2p-947486.pdf](https://www.mouser.it/datasheet/2/315/panasonic_vrla_lc-r067r2p-947486.pdf).

- 
- [65] M. Ebad and Byeong-Mun Song, 'Accurate model predictive control of bidirectional DC-DC converters for DC distributed power systems', in *2012 IEEE Power and Energy Society General Meeting*, San Diego, CA, 2012, pp. 1–8.
- [66] X. Dominguez, O. Camacho, P. Leica, and A. Rosales, 'A fixed-frequency Sliding-mode control in a cascade scheme for the Half-bridge Bidirectional DC-DC converter', in *2016 IEEE Ecuador Technical Chapters Meeting (ETCM)*, Guayaquil, 2016, pp. 1–6.
- [67] G. Rajapakse, S. Jayasinghe, A. Fleming, and M. Negnevitsky, 'Grid Integration and Power Smoothing of an Oscillating Water Column Wave Energy Converter', *Energies*, vol. 11, no. 7, p. 1871, Jul. 2018.
- [68] A. Pirooz and R. Noroozian, 'Model predictive control of classic bidirectional DC-DC converter for battery applications', in *2016 7th Power Electronics and Drive Systems Technologies Conference (PEDSTC)*, Tehran, Iran, 2016, pp. 517–522.
- [69] P. Pany, R. K. Singh, and R. K. Tripathi, 'Bidirectional DC-DC converter fed drive for electric vehicle system', p. 10.
- [70] J. Zhang, 'Bidirectional DC-DC Power Converter Design Optimization, Modeling and Control', p. 149.
- [71] Y. Shan, J. Hu, Z. Li, and J. M. Guerrero, 'A Model Predictive Control for Renewable Energy Based AC Microgrids Without Any PID Regulators', *IEEE Transactions on Power Electronics*, vol. 33, no. 11, pp. 9122–9126, Nov. 2018.
- [72] M. Bhardwaj, 'Modeling Bi-Directional Buck/Boost Converter for Digital Control Using C2000 Microcontrollers', p. 12, 2015.
- [73] S. Serna-Garcés, D. González Montoya, and C. Ramos-Paja, 'Control of a Charger/Discharger DC/DC Converter with Improved Disturbance Rejection for Bus Regulation', *Energies*, vol. 11, no. 3, p. 594, Mar. 2018.
- [74] A. A. T. Alkhalidi and N. H. A. Dulaimi, 'Design of an Off-Grid Solar PV System for a Rural Shelter', *Unpublished*, 2018.
- [75] A. T. Ghareeb, T. A. Youssef, A. Mohamed, and O. A. Mohammed, 'Design and Control of Standalone P-V System for Rural Residential Applications', p. 8, 2013.
- [76] A. Pandey, N. Dasgupta, and A. K. Mukerjee, 'Design Issues in Implementing MPPT for Improved Tracking and Dynamic Performance', in *IECON 2006 - 32nd Annual Conference on IEEE Industrial Electronics*, Paris, France, 2006, pp. 4387–4391.
- [77] M. Rosu-Hamzescu and S. Oprea, 'Practical Guide to Implementing Solar Panel MPPT Algorithms', p. 16, 2013.
- [78] M. Metry, S. Bayhan, R. S. Balog, and H. A. Rub, 'Model predictive control for PV maximum power point tracking of single-phase submultilevel inverter', in *2016 IEEE Power and Energy Conference at Illinois (PECI)*, Urbana, IL, USA, 2016, pp. 1–8.
- [79] M. G. Villalva and E. R. Filho, 'BUCK CONVERTER WITH VARIABLE INPUT VOLTAGE FOR PHOTOVOLTAIC APPLICATIONS', p. 7.
- [80] M. B. Shadmand, X. Li, R. S. Balog, and H. A. Rub, 'Model predictive control of grid-tied photovoltaic systems: Maximum power point tracking and decoupled power control', in *2015 First Workshop on Smart Grid and Renewable Energy (SGRE)*, Doha, Qatar, 2015, pp. 1–6.
- [81] D. E. Quevedo, R. P. Aguilera, and T. Geyer, 'Predictive Control in Power Electronics and Drives: Basic Concepts, Theory, and Methods', in *Advanced and Intelligent Control in Power Electronics and Drives*, vol. 531, T. Orłowska-Kowalska, F. Blaabjerg, and J. Rodríguez, Eds. Cham: Springer International Publishing, 2014, pp. 181–226.
- [82] L. Wang, *Model predictive control system design and implementation using MATLAB*. London: Springer, 2009.
- [83] Petros Karamanakos, 'Model Predictive Control Strategies for Power Electronics Converters and AC Drives', *PhD thesis, National Technical University of Athens*, 2013.
- [84] S. Bououden, O. Hazil, S. Filali, and M. Chadli, 'Modelling and model predictive control of a DC-DC Boost converter', in *2014 15th International Conference on Sciences and Techniques of Automatic Control and Computer Engineering (STA)*, Hammamet, Tunisia, 2014, pp. 643–648.

- 
- [85] A. Bemporad, N. L. Ricker, and M. Morari, 'Model Predictive Control Toolbox™', p. 172.
- [86] 'Sensitivity analysis', *Wikipedia*. 02-Jul-2019.
- [87] P. Karamanakos, T. Geyer, and S. Manias, 'Direct Voltage Control of DC–DC Boost Converters Using Enumeration-Based Model Predictive Control', *IEEE Transactions on Power Electronics*, vol. 29, no. 2, pp. 968–978, Feb. 2014.

---

## Appendix A – MATLAB Scripts of Chapter 2

### A.1. Iterative process to calculate Rs and Rp

MATLAB script file used to calculate the values of Rs and Rp iteratively.

```
%%PV model. Iterative process to calculate Rs and Rp. Graphs Validation at
%STC. Newton Raphson for current extraction.
```

```
%PV parameters SOLAREX SX80
Vmpp = 16.8; %Voltage at MPP in STC
Impp = 4.75; %Current at MPP in STC
Pmpp = Vmpp*Impp; %Power at MPP in STC
Iscn = 5.17; %Short circuit current at STC
Vocn = 21.0; %Open circuit voltage at STC
Ns = 36; %Number of series connected cells
Ki = 0.0033605; %Short circuit coeff.[A/K]
Kv = -0.08; %Open circuit coeff.[V/K]
%Constants
k = 1.38065e-23; %Boltzman constant
q = 1.60218e-19; %Charge of electron
a = 1.3; %Diode ideality factor
Eg = 1.12; %Band gap of silicon at 25°C
%Nominal values at STC
To = 273.15+25; %Nominal temperature
Go = 1000; %Nominal irradiance
%Working values
T = 25; %Operating temperature in °C
Tc = 273.15+T; %Operating temperature in °K
G = 1000; %Actual irradiance
%Equations
Vt = Ns*k*Tc/q; %Junction thermal voltage of array
Ion = Iscn/(exp(q*Vocn/(Ns*a*k*To))-1); %Nominal diode saturation current
b = q*Eg/(a*k);
%Io = Ion*(Tc/To)^(3)*exp(b*(1/To -1/Tc)); %Diode saturation current
Io = (Iscn + Ki*(Tc - To))/(exp((Vocn+Kv*(Tc-To))/(a*Vt))-1); %Diode
saturation current

%Reference values for Rs and Rp
Rs_max = (Vocn - Vmpp)/Impp;
Rp_min = Vmpp/(Iscn-Impp) - Rs_max;
%Initial values
Rs = 0;
Rp = Rp_min;
tol = 0.001; %Power mismatch tolerance
Rsinc = 0.001; %Increment of Rs
P = [0];
error = Inf;

%Iterative process to get Rs and Rp, until Pmpp_model = Pmpp;
count = 1;
while (error > tol)
    %Irradiation effect on current
    Iphn = (Rp+Rs)/Rp*Iscn; %Nominal photocurrent
    Iph = (G/Go)*(Iphn + Ki*(Tc - To)); %Photocurrent
    %Increment Rs
    Rs = Rs + Rsinc;
    %Parallel resistance Rp
```

---

```

Rp = (Vmpp+Impp*Rs) / (Iph-Io*(exp((Vmpp+Impp*Rs)/(a*Vt))-1)-Impp);

%Solving I-V equation with Newton-Raphson
V = [0:0.1:Vocn];
I = zeros(1,size(V,2));

for i = 1:size(V,2)
    %Solve I2 = I1 -f(I1)/f'(I1);
    f(:,i) = Iph -I(:,i) -Io*(exp((V(i)+I(:,i)*Rs)/(a*Vt))-1) -
(V(i)+I(:,i)*Rs)./Rp;

    while (sum(abs(f(:,i)) > 0.001) > 0)
        f(:,i) = Iph -I(:,i) -Io*(exp((V(i)+I(:,i)*Rs)/(a*Vt))-1) -
(V(i)+I(:,i)*Rs)./Rp;
        %f'(:,i) = -1-Io*(Rs./(a*Vt))*exp((V(i)+I(:,i)*Rs)/(a*Vt))-
(Rs/Rp);
        I(:,i) = I(:,i)-(Iph -I(:,i) -Io*(exp((V(i)+I(:,i)*Rs)/(a*Vt))-1)
-(V(i)+I(:,i)*Rs)./Rp)/(-1-Io*(Rs./(a*Vt))*exp((V(i)+I(:,i)*Rs)/(a*Vt))-
(Rs/Rp));
    end
end

%Calculate power using I-V equation
P = I.*V;
Pmax_m = max(P);
error = Pmax_m - Pmpp;
count = count +1;
end
Rs = Rs; %Internal series resistance
Rp = Rp; %Internal parallel resistance

```

## A.2. PV model validation

MATLAB script file used to generate the simulation results shown in chapter 2.1.

```

%%Graphs Validation of the PV model. To compare with the graphs of the Data
Sheet. Valid for different working values Tc(temperature) and G(irradiation).

%PV parameters SX-80
[...]
%Equations
Vt = Ns*k*Tc/q; %Junction thermal voltage of array
Iphn = (Rp+Rs)/Rp*Iscn; %Nominal photocurrent
Iph = (G/Go)*(Iphn + Ki*(Tc - To)); %Photocurrent
Ion = Iscn/(exp(q*Vocn/(Ns*a*k*To))-1); %Nominal diode saturation current
b = q*Eg/(a*k);
Io = (Iscn + Ki*(Tc - To))/(exp((Vocn+Kv*(Tc-To))/(a*Vt))-1); %Diode
saturation current

%Extracting the V-I (working) values
V = [0:0.1:Vocn];
I = zeros(1,size(V,2));
P = (0);
%Extract the Ipv
for i = 1:size(V,2)
    %Newton raphson I2 = I1 -f(I1)/f'(I1);
    f(:,i) = Iph -I(:,i) -Io*(exp((V(i)+I(:,i)*Rs)/(a*Vt))-1) -
(V(i)+I(:,i)*Rs)./Rp;
    while (sum(abs(f(:,i)) > 0.001) > 0)

```

```

        f(:,i) = Iph -I(:,i) -Io*(exp((V(i)+I(:,i)*Rs)./(a*Vt))-1) -
(V(i)+I(:,i)*Rs)./Rp;
        %f'(:,i) = -1-Io*(Rs./(a*Vt))*exp((V(i)+I(:,i)*Rs)./(a*Vt))-
(Rs/Rp);
        I(:,i) = I(:,i)-(Iph -I(:,i) -Io*(exp((V(i)+I(:,i)*Rs)./(a*Vt))-1)
-(V(i)+I(:,i)*Rs)./Rp)/(-1-Io*(Rs./(a*Vt))*exp((V(i)+I(:,i)*Rs)./(a*Vt))-
(Rs/Rp));
        end
        if I(:,i) <0
            I(:,i) = 0;
        end
    end
end
P = I.*V;

%Graphs
figure(1)
plot(V,I,'k')
xlabel('Voltage (V)');
ylabel('Current (A)');
title('I-V Characteristic')
axis([0,max(Vocn)*1.1, 0,max(I)*1.1])
figure(2)
plot(V,V.*I,'k')
xlabel('Voltage (V)');
ylabel('Power (W)');
title('P-V Characteristic')
axis([0,max(Vocn)*1.1,0,max(V*max(I))*0.8])

```

### A.3. Simulation of the non-inverting Buck-Boost model with trapezoidal integration

MATLAB script file used to generate the simulation results shown in chapter 2.2.6

```

%%%Time-domain modeling and simulation of the non-inverting Buck-Boost
%converter, using trapezoidal integration. The trapezoidal rule of
%integration is chosen for its efficiency, accuracy and good numerical
%stability characteristics.
%Switching modes: 1) Buck Vo<Vpv; 2) Boost Vo>Vpv.

%Buck-Boost Parameters
Vo = 12; %reference output voltage
Vpv = 16.8; %input voltage = output voltage of the PV
Ipv = 4.75; %input current
L = 0.33e-3; %inductance
C1 = 700e-6; %input capacitor
C2 = 700e-6; %output capacitor
R = 1.8; %3.6 %resistive load
Ts = 5e-5; %switching period
fs = 1/Ts; %switching frequency 20kHz
tend = 5000*Ts; %simulation time
dt = 1e-6; %simulation time step
tol = dt/2; %tolerance needed for switching
t = 0:dt:tend;
tsize = size(t,2);

%Matrices
A1 = [0, 1/L, 0; -1/C1, 0, 0; 0, 0, -1/(R*C2)]; %Boost S2 ON state
A2 = [0, 1/L, -1/L; -1/C1, 0, 0; 1/C2, 0, -1/(R*C2)]; %Boost S2 OFF state =
Buck S1 ON state
A3 = [0, 0, -1/L; 0, 0, 0; 1/C2, 0, -1/(R*C2)]; %Buck S1 OFF state
B = [0; 1/C1; 0]; %B1=B2=B3

```

---

```

C = [0, 1, 0]; %C1=C2=C3
D = [0]; %D1=D2=D3

%Initial configuration for matrices:
A = A2;
M = inv(eye(3) - 1/2*dt*A) * (eye(3) + 1/2*dt*A);
N = inv(eye(3) - 1/2*dt*A) * 1/2*dt*B;
d = zeros(1,tsize); % to plot Dt in [0,1]
onoff = 0; % 1 is on, 0 is off
Dt = zeros(1,tsize);
Dt(:) = 0.7;%sqrt(R*Ipv/Vpv); %Buck Duty cycle

x = zeros(3,tsize); % x = [iL; vc1; vc3];
y = zeros(1,tsize); % y = vpv;
u = Ipv*ones(1,tsize);

for k = 2:tsize
    if (Vpv < Vo) %Boost mode
        if mod(t(k),Ts) > -tol && mod(t(k),Ts) < tol
            onoff = 1;
            A = A1;
        elseif mod(t(k),Ts) > Dt(k)*Ts-tol && mod(t(k),Ts) < Dt(k)*Ts+tol
            onoff = 0;
            A = A2;
        end
    elseif (Vpv > Vo) %Buck mode
        if mod(t(k),Ts) > -tol && mod(t(k),Ts) < tol
            onoff = 1;
            A = A2;
        elseif mod(t(k),Ts) > Dt(k)*Ts-tol && mod(t(k),Ts) < Dt(k)*Ts+tol
            onoff = 0;
            A = A3;
        end
    end
    M = inv(eye(3) - 1/2*dt*A) * (eye(3) + 1/2*dt*A);
    N = inv(eye(3) - 1/2*dt*A) * 1/2*dt*B;
    x(:,k) = M*x(:,k-1) + N*(u(k-1) + u(k));
    y(:,k) = C*x(:,k) + D*u(k);
    d(k) = onoff;
end

figure(1)
plot(t,u,t,x)
xlabel('time (s)');
ylabel('Voltage(V), current(A)');
title('Converter Simulation');
legend('ipv','iL','vpv','vo')

```

#### A.4. Battery cell model validation

MATLAB script file used to generate the simulation results shown in chapter 2.3.2

```

%%%NiNM Panasonic HHR650D3 Cell Model Validation.
%%%Discharge voltage curve function of time
Ib = 1.3; %Constant battery current [A]
Qo = 6.5; %Rated battery capacity [Ah]
Rb = 0.0046; %Constant internal resistance [Ohm]
Efull = 1.39; %Fully charged voltage [V]
Eexp = 1.25; %Voltage at the end of the exp. zone [V]
Enom = 1.20; %Voltage at the end of the nominal zone [V]

```

---

```

Qexp = Ib*1;           %Battery charge at the end of the exp. zone[Ah]
Qnom = 5.2;           %Battery charge at the end of the nom. zone[Ah]
A = Efull - Eexp;    %Exponential zone amplitude [V]
B = 3/Qexp;          %Exponential zone time constant inverse [1/Ah]
K = (Efull -Enom +A*(exp(-B*Qnom)-1))*(Qo -Qnom)/Qnom;%Polarization voltage
Eo = Efull + K + Rb*Ib - A; %Battery constant voltage [V]

tend = 5;           %Simulation time [h]
dt = 1/60;         %Simulation time step 1min
t = 0:dt:tend;
for i= 1:size(t,2)
    Q(i) = Ib*t(i);
    E(i) = Eo - K*Qo/(Qo-Q(i)) + A*exp(-B*Q(i)); %Voltage at no load [V]
    Vb(i) = E(i) -Rb*Ib; %Battery terminal voltage[V]
    DOD(i) = Q(i)/Qo; %Depth of Discharge DOD
    SOC(i) = 1 -DOD(i); %State of Charge
end
figure(1)
plot(t,Vb,'k')
xlabel('time [h]');
ylabel('Battery Cell voltage Vb [V]')
title('Discharge Characteristics')
axis([0,tend,0.8,max(Vb)])
legend('Ib = 1.3A')

```

## A.5. Lead-acid battery pack simulation

MATLAB script file used to generate the simulation results shown in chapter 2.3.3

```

%%%Lead-Acid Panasonic LC-R067R2P Battery pack simulation.
%%%Charging and discharging voltage curve function of SOC.
Ns = 1;           %Number of series cells
Np = 10;          %Number of parallel cells
Ib = Np*0.72;    %Constant battery current [A]
Qo = Np*7.2;     %Rated battery capacity [Ah]
Rb = 0.02*Ns/Np; %Constant internal resistance [Ohm]
Efull = Ns*6.4;  %Fully charged voltage [V]
Eexp = Ns*6.1;   %Voltage at the end of the exponential zone [V]
Enom = Ns*6;     %Voltage at the end of the nominal zone [V]
Qexp = Ib/60;    %Battery charge at the end of the exp. zone[Ah]
Qnom = Np*2.88;  %Battery charge at the end of the nom. zone[Ah]
A = Efull - Eexp; %Exponential zone amplitude [V]
B = 3/Qexp;      %Exponential zone time constant inverse [1/Ah]
K = (Efull -Enom +A*(exp(-B*Qnom)-1))*(Qo -Qnom)/Qnom;%Polarization voltage
Eo = Efull + K + Rb*Ib - A;%Battery constant voltage [V]

Q =[0:0.01:Qo];   %Actual battery charge [Ah]
for i= 1:size(Q,2)
    E(i) = Eo - K*Qo/(Qo-Q(i)) + A*exp(-B*Q(i)); %Voltage at no load [V]
    Vb(i) = E(i) -Rb*Ib; %Battery terminal voltage [V]
    DOD(i) = Q(i)/Qo; %Depth of Discharge DOD =Eb/En;
    SOC(i) = 1 -DOD(i); %State of Charge
end
figure(1)
plot(SOC,Vb,'k')
xlabel('SOC');
ylabel('Battery Pack Voltage Vb (V)')
title('Charging and discharging voltage curve')
axis([0,1,0.6,max(Vb)])
legend('Ib = Np*0.72A')

```

---

## Appendix B – MATLAB Scripts of Chapter 3

### B.1. P&O algorithm

MATLAB script file used to simulate the performance of the basic P&O algorithm outlined in the flowchart in Fig. 3.2.

```
%%%P&O Algorithm Validation%%%
%PV parameters SX-80
[...]
%Extracting the V-I (working) values
[...]

%MPPT - P&O
%Initialize the internal values for the voltage and power on the first pass
Vprev = 21;
Pprev = 0;
Iprev = 0;
%Initialize increment/ decrement parameter
deltaV = 0.25;

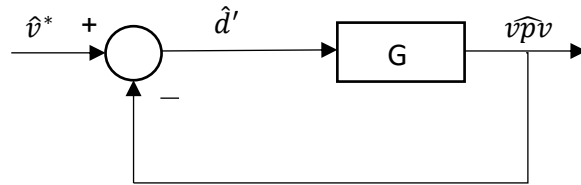
tend = 1.5; %Simulation time
dt = 0.025; %Simulation time step 1/40Hz
t = 0:dt:tend;
for j= 1:size(t,2)
    %Calculated the power
    Ppv = Vpv*Ipv;
    %Increase or decrease voltage based on conditions
    if (Ppv-Pprev) ~= 0
        if (Ppv-Pprev) > 0
            if (Vpv-Vprev) > 0
                Vref = Vpv + deltaV;
            else
                Vref = Vpv - deltaV;
            end
        elseif(Ppv-Pprev) < 0
            if (Vpv-Vprev) > 0
                Vref = Vpv - deltaV;
            else
                Vref = Vpv + deltaV;
            end
        end
    else
        Vref = Vpv;
    end

    %Update internal values
    Pprev = Ppv;
    Vprev = Vpv;
    Iprev = Ipv;
end
figure(1)
plot(t,Ppv,'k')
xlabel('time (s)');
ylabel('PV Power (W)')
title('MPPT - P&O Algorithm')
```

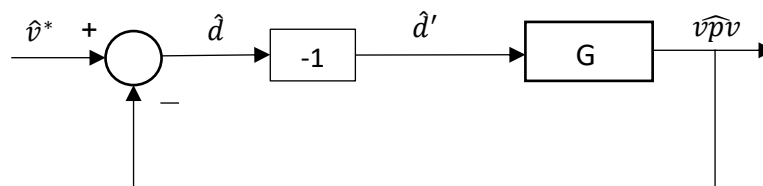
## B.2. Positive feedback control demonstration

In the following, using control properties, we will demonstrate that the application of positive feedback control equals dynamically to the inversion of the switch control signal.

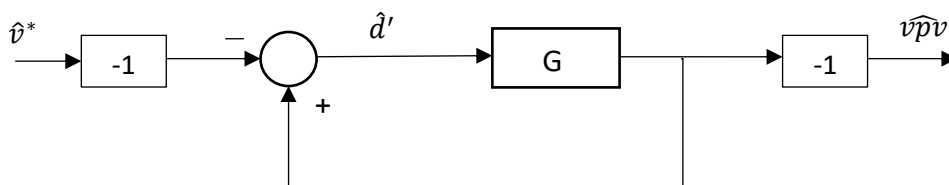
Considering that this statement is true, a negative feedback using the inverse of the control signal  $\hat{d}'$  can be built.



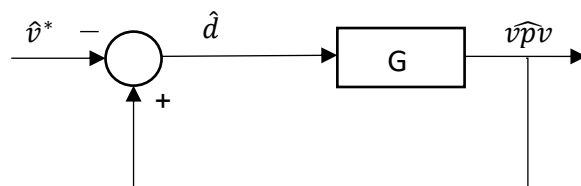
Since  $\hat{d}' = -\hat{d}$ , the block diagram can be represented as



And using control block properties, the diagram can be represented as



Simplifying the two negative unity blocks, the positive feedback of the control variable  $\hat{d}$  is obtained.



This means that the control variable  $\hat{d}$  can be used in the implementation of the closed loop control system, with positive feedback control meaning that the polarities of the feedback and reference voltage signals must be interchanged.

## B.3. PI controller design

MATLAB script file used to obtain the frequency responses of the converter, the step response of the closed loop system and the design of the PI controller.

```

%% Bode Plots - PI controller design - Closed loop response
% Parameters at MPP operating point
Ipv = 4.75; % Input current

```

---

```

D = 0.7; %Steady state duty cycle
L = 0.33e-3; %Inductance
C1 = 700e-6; %Input capacitor
C2 = 700e-6; %Output capacitor
R = 1.8; %Load resistance

%Steady state model - DC Values
%X = [IL; Vc1; Vc2]; U = [Ipv]; Y = [Vpv];
A = [0, 1/L, -(1-D)/L; -1/C1, 0, 0; (1-D)/C2, 0, -1/(R*C2)];
B = [0; 1/C1; 0];
C = [0 1 0];
A_1 = inv(A);
IL = -A_1(1,:) * B * Ipv; %Inductance current
Vc1 = -A_1(2,:) * B * Ipv; %Input voltage =Vpv
Vc2 = -A_1(3,:) * B * Ipv; %output voltage =Vdc
Vpv = -C * inv(A) * B * Ipv; %Output variable =Vpv(1-D)^2 * R * Ipv

%Small Signal Model - x' = [iL'; vc1'; vc2']; u' = [d']; y' = [vpv'];
a = [0, 1/L, -(1-D)/L; -1/C1, 0, 0; (1-D)/C2, 0, -1/(R*C2)];
m = [-Vc2/L; 0; IL/C2];
c = [0, 1, 0];
G = ss(a,m,c,[0]); %State space small-signal model

%%Open-loop analysis
G_tf = tf(G); %Small-signal TRF
disp(['Control to input voltage transfer function']);
disp(['vpv/d+ (s)']);
G_tf
figure(1)
bode(G_tf)
title('Bode driagram of the open loop system')

%%PI controller design using Control System Designer Toolbox
%step(G_tf); %Step response of the open-loop uncompensated
%rlocus(G_tf) %Root locus of the open-loop uncompensated
%controlSystemDesigner(G_tf);

%PI controllers parameters
Kp = 0.0017; %Proportional gain parameter
Ki = 1; %Integral gain parameter
Ci = pid(Kp,Ki); %PI controller
Ci = tf(Ci); %Controller TRF
Go = Ci * G_tf; %Open loop compensated TRF
figure(2)
bode(G_tf,Go);
legend('uncompensated','compensated')
title('Bode driagram of the open loop system')

%%Closed-loop analysis
G = feedback(Go,1); %Closed loop TRF
figure(3)
step(G)
ylabel('G(s)')
title('Closed loop step responce')

```

#### B.4. Voltage controlled MPPT-converter simulation

MATLAB script file used to obtain the simulation results of section 3.2.4. The control algorithm includes the PV model, the non-inverting Buck-Boost converter model, the MPP tracking algorithm and the input voltage control loop.

---

```

%%Voltage controlled MPPT-Converter Simulation
%%PV parameters SX-80
[...]
%Extracting the V-I (working) values
[...]
Ppv = Vpv*Ipv;      %Initial working point

%%MPPT
%Initialize the internal values for the voltage and power on the first pass
Vprev = 21;
Pprev = 0;
%Initialize increment/ decrement parameter
deltaV = 0.05;

%%Non-inverting Buck-Boost Parameters
[...]

%%Simulation Parameters
tend = 20000*Ts;    %simulation time
dt = 1e-6;         %simulation time step (1us)
tol = dt/2;        %tolerance needed for switching
t = 0:dt:tend;
tsize = size(t,2);

%%%%%%%%%%%%%%%%%%%%%%%%%%%%%%%%%%%%%%%%%%%%%%%%%%%%%%%%%%%%%%%%%%%%%%%%
%Initial configuration for matrices:
[...]

%PI Controller parameters (valid for both modes of operation, Boost&Buck)
kp = 0.0017;
ki = 1;

%Parameters initial configuration
dmax = 0.99;       %Duty cycle max saturation
dmin = 0.01;       %Duty cycle min saturation
dtc = 1e-3;        %Control loop sampling period(1ms) (fc = 1kHz)
integral = 0;
error = 0;
z = 1;
told = 0;
toldpv = 0;
dmaxwu= 0.007;
Vref = Vpv;
%%%%%%%%%%%%%%%%%%%%%%%%%%%%%%%%%%%%%%%%%%%%%%%%%%%%%%%%%%%%%%%%%%%%%%%%
for k = 2:tsize
    %%PV model
    %Extract the Ipv
    for m=1:5
        Ipv = Ipv - (Iph-Ipv-Io*(exp((Vpv+Ipv*Rs)/(a*Vt))-1) -
(Vpv+Ipv*Rs)/Rp)/(-1-Io*(Rs/(a*Vt))*exp((Vpv+Ipv*Rs)/(a*Vt)) - (Rs/Rp));
    end
    u(k) = Ipv;

    %%MPPT loop (40Hz)
    if (t(k) -toldpv) > 0.025 %every 1/40Hz -> run mppt
        Ppv = Vpv*u(k);
        %P&O Algorithm - Increase or decrease voltage based on conditions
        if (Ppv-Pprev) ~= 0
            if (Ppv-Pprev) > 0
                if (Vpv-Vprev) > 0

```

---

```

        Vref = Vpv + deltaV;
    else
        Vref = Vpv - deltaV;
    end
elseif(Ppv-Pprev) < 0
    if (Vpv-Vprev) > 0
        Vref = Vpv - deltaV;
    else
        Vref = Vpv + deltaV;
    end
end
else
    Vref = Vpv;
end
%Update internal values
Pprev = Ppv;
Vprev = Vpv;
toldpv = t(k);
end

%%%PI Control loop (1kHz)
if (t(k) - told > dtc) %every 1ms -> run control loop
    z = z+1;
    error(z) = -Vref + Vpv; %error signal
    integral(z) = ki*error(z)*dtc + integral(z-1);
    %integral anti-windup
    if (integral(z) > dmaxwu)
        integral(z) = dmaxwu;
    elseif (integral(z) < -dmin)
        integral(z) = -dmin;
    end
    ds(z) = kp*error(z) + integral(z); %small signal duty cycle

    %Steady state duty cycle D
    if (Vpvin <= Vo) %Boost mode
        Ds = 1- sqrt(Vref/(R*u(k)));
    else (Vpvin > Vo); %Buck mode
        Ds = sqrt(R*u(k)/Vref);
    end
    %Control Duty Cycle
    Dt(z) = Ds + ds(z);
    %Saturation
    if (Dt(z) > dmax)
        Dt(z) = dmax;
    elseif (Dt < dmin)
        Dt(z) = dmin;
    end
    told = t(k);
end

%%%Buck or Boost operation
if (Vpvin < Vo) %Boost mode
    if mod(t(k),Ts) > -tol && mod(t(k),Ts) < tol
        onoff = 1;
        A = A1;
    elseif mod(t(k),Ts) > Dt(z)*Ts-tol && mod(t(k),Ts) < Dt(z)*Ts+tol
        onoff = 0;
        A = A2;
    end
elseif (Vpvin > Vo) %Buck mode
    if mod(t(k),Ts) > -tol && mod(t(k),Ts) < tol

```

---

```

        onoff = 1;
        A = A2;
    elseif mod(t(k),Ts) > Dt(z)*Ts-tol && mod(t(k),Ts) < Dt(z)*Ts+tol
        onoff = 0;
        A = A3;
    end
end
%%Non-inverting Buck-Boost model (Trapezoidal method integration)
zi(k) = t(k)/Ts;
M = inv(eye(3) - 1/2*dt*A) * (eye(3) + 1/2*dt*A);
N = inv(eye(3) - 1/2*dt*A) * 1/2*dt*B;
x(:,k) = M*x(:,k-1) + N*(u(k-1) + u(k));
y(:,k) = C*x(:,k) + D*u(k);
d(k) = onoff;
Vpv = y(k);
end

tz = 0:(tend/z):(tend-tend/z);
points = tz./tz; points(1) = 1;%control step points

figure(1)
plot(t,u,t,x)          %u = [ipv]  x = [vpv iL vo]
xlabel('time (s)');
ylabel('Volage (V), Current (A)')
title('Voltage Controlled MPPT-Converter Simulation')
legend('ipv', 'iL', 'vpv', 'vo')
grid on
figure(2)
%show change in input current and duty cycle
%plot at which points control is executed and relative error
plot(t,u/max(u),tz,Dt,tz,points, '.',tz,error/Vref)
title('input current, duty cycle, relative error analysis')
legend('input current', 'duty cycle', 'control set points', 'relative error')
xlabel('time (s)');

```

## B.5. MPC Algorithm – Single-step prediction horizon current control

MATLAB script file used to simulate the performance of the basic MPC strategy proposed in section 3.3, together with the Battery and the Bidirectional models.

```

%%MPC current control with one step in the horizon, together with Battery
and Bidirectional models%%
%%Battery Pack model Parameters
%Input SOC0, ib(t)          Output SOC(t), Vb(t)
[...]
SOC0 = 0.6;                  %Initial battery SOC
%%Bidirectional Parameters and initial conditions
[...]
tend = 0.5;                  %Simulation time [s]
dt = 1e-6;                   %Simulation time step [s]
t = 0:dt:tend;

%%MPC model
%s=1 Q1 on, Q2 off
%s=0 Q1 off, Q2 on
Ts = 5e-5;
vdcref = 12;                 %DC-link referance voltage
told = 0;
z = 0;

```

---

```

for i= 2:size(t,2)
    %Battery
    Qdt(i) = -ib(i-1)*dt + Qdt(i-1);%Charge sottracted/added during dt [Ah]
    Qin = Qo*SOC0; %Initial charge [Ah]
    Q(i) = Qin + Qdt(i); %Actual battery charge [Ah]
    SOC(i) = SOC0 + Qdt(i)/Qo; %Actual state of charge
    Eo = Efull + K + Rb*ib(i-1) - A;%Battery constant voltage [V]
    u(i) = Eo - K*Qo/Q(i) + A*exp(-B*(Qo-Q(i)));%No-load voltage [V]
    Vb(i) = u(i) -Rb*ib(i-1); %Battery terminal voltage [V]

    %MPC
    if (t(i)-told > 5*Ts)
        z = z+1;
        iLk1_1(z) = iL(i-1) + Ts*vb(i-1)/Lb;
        iLk1_0(z) = iL(i-1) -Ts*vdc(i-1)/Lb + Ts*vb(i-1)/Lb;
        iLref = (vdcref^2)/R/vb(i-1);%Pbattery=Pload
        J_1(z) = abs(iLref - iLk1_1(z));
        J_0(z) = abs(iLref - iLk1_0(z));
        if (J_1(z) < J_0(z))
            s = 1;
        elseif (J_1(z) > J_0(z))
            s = 0;
        end
        S(z) = s;
        told = t(i);
        a = [0, 1/Lb, -(1-S(z))/Lb; -1/Cb, -1/(Rb*Cb), 0; (1-S(z))/C2, 0, -
1/(R*C2)];%Update matrix
    end

    %Bidirectional Model - trapezoidal method
    M = inv(eye(3) - 1/2*dt*a) * (eye(3) + 1/2*dt*a);
    N = inv(eye(3) - 1/2*dt*a) * 1/2*dt*b;
    x(:,i) = M*x(:,i-1) + N*(u(i-1) + u(i));
    iL(i) = x(1,i);
    vb(i) = x(2,i);
    vdc(i) = x(3,i);
    %ib(i) = iL(i) +Cb*(vb(i)-vb(i-1))/dt;%Battery current
    ib(i) = iL(i);
end

figure(1)
plot(t,SOC*100)
xlabel('time');
ylabel('SOC %')
title('SOC')
figure(2)
plot(t,x)
xlabel('time');
ylabel('Voltage (V), Current (A)')
title('MPC Control Simulation')
legend('iL','vb','vdc')

```

---

## Appendix C – MATLAB Scripts of Chapter 4

### C.1. Direct voltage MPC Algorithm using MATLAB MPC Toolbox

MATLAB script file used to simulate the performance of the direct voltage MPC strategy proposed in section 4.3, using the MATLAB MPC Toolbox at command line.

```
%%MPC control strategy of the Bidirectional converter using MPC Toolbox.
%Bidirectional converter linearized at steady state point, to get the small-
%signal model representing the variations around steady state duty cycle.

%Bidirectional Parameters
L = 33e-3; %inductance
R = 5; %load resistance
C2 = 800e-6; %output capacitance
Vb = 6; %measured disturbance signal
S = 0.5; %steady state duty cycle
Vdc = Vb/(1-S); %steady state dc bus voltage
IL = Vdc/((1-S)*R); %steady state inductor current

%Small-signal matrices that define the system
%x = [iL; vdc]; u = [Vb; s]; y = [vdc];
a = [0, -(1-S)/L; (1-S)/C2, -1/(R*C2)];
b = [Vdc/L, 1/L; -IL/C2, 0];
c = [0 1];
d = [0 0];

%Small-signal model identification
Gmpc = ss(a,b,c,d); %create the state space model
Gmpc.InputName = {'ss','Vb'}; %define input names of the model
Gmpc.OutputName = {'vdc'}; %define output names of the model
Gmpc.StateName = {'iL','vdc'}; %define state names of the model

%Set signal types in MPC plant model
Gmpc.InputGroup.MV = 1; %set manipulated variable (input channel)
Gmpc.InputGroup.MD = 2; %set measured disturbance (input channel)
Gmpc.OutputGroup.MO = 1; %set manipulated output (output channels)
%Gmpc = setmpcsignals(Gmpc,'MV',1,'MD',2,'MO',1);%alternative

%Create MPC controller object with sample time
Ts = 0.005; %Sample time
MPCobj = mpc(Gmpc, Ts);
MPCobj.PredictionHorizon = 10; %specify prediction horizon
MPCobj.ControlHorizon = 2; %specify control horizon
MPCobj.MV = struct('Min',-1,'Max',1);%specify constraints for MV
MPCobj.Model.Plant.OutputUnit = {'V'};%specify the output unit

%Display the controller properties in the Command Window
display(MPCobj)

%Run simulation
Tend = 0.5; %simulation time
T = round(Tend/Ts); %number of simulation steps
Vref = 12; %reference signal
sim(MPCobj,T,Vref,Vb)
```

---

```
%Extract simulation results
[y,t,u] = sim(MPCobj,T,Vref,Vb);

%Calculate continuous-time duty cycle (s) as a summation of the steady
%state value (S) and the small-signal value (ss)
ss = u;           %small signal duty cycle
s = S +ss;       %duty cycle
```